A NOVEL SOLID STATE GENERAL ILLUMINATION SOURCE

A Thesis
Presented to
The Academic Faculty

by

David B. Nicol

In Partial Fulfillment
of the Requirements for the Degree
Doctor of Philosophy in the
School of Electrical and Computer Engineering

Georgia Institute of Technology
December 2006

A NOVEL SOLID STATE GENERAL ILLUMINATION SOURCE

Approved by:

Ian Ferguson, Committee Chair
School of Electrical and Computer Engineering
Georgia Institute of Technology

John Cressler
School of Electrical and Computer Engineering
Georgia Institute of Technology

William Doolittle
School of Electrical and Computer Engineering
Georgia Institute of Technology

Christopher Summers
School of Materials Science and Engineering
Georgia Institute of Technology

Gianluca Tosini
Department of Anatomy and Neurobiology
Morehouse School of Medicine

Date Approved: 12 September 2006

To my wife, Michelle,

parents, Jean-Paul and Lizabeth,

Beverly, Roy and Steve

siblings, Marie, Daniel and Tiffany

and dogs, Guinness, Ginger and Kylie

ACKNOWLEDGEMENTS

Thank you to the United States Department of Energy for funding my work. Thank you to my advisor, Dr. Ian Ferguson for his continued time and support over the years. Your leadership and mentoring mean a lot. Thank you to Dr. Cressler, Dr. Doolittle, Dr. Summers and Dr. Tosini for taking time out of their busy schedules to aid me in this endeavor. I would like to also acknowledge the support of my research group including Ali Asghar, Eun-Hyun Park, Martin Strassburg, Will Fenwick, Shalini Gupta, Matthew Kane, Hun Kang, Nola Li, June O Song, Vincent Woods, Yong Huang, Omkar Jani and Olivier Hamard. I would also like to thank my wife and family to whom this work is dedicated.

TABLE OF CONTENTS

LIST OF TABLES

LIST OF FIGURES

SUMMARY

A novel solid state illumination source has been developed. A two terminal dual LED has been created with the ability to control the relative intensities of the two emission peaks by varying drive current. Doping profiles have been used to extend the dynamic range of the dual LED over other reported devices. Operation of the dual LEDs is explained as a function of drive current. In addition, novel use of phosphor mixtures allows the creation of a broadband spectral power distribution that can be varied using a dual LED as an excitation source. Combinations of phosphors that have varied excitation spectra provide the ability to selectively excite different phosphors with the different LED emission peaks. First and second generations of the two terminal dual LED and the phosphor combination are discussed. The final source has the ability to mimic the light of a blackbody radiator over a range of 3200 K - 5300 K. The development of a three terminal dual LED as a pump source was prohibited by the need for a III-nitride tunnel junction, that proved unattainable in the scope of this work. However, several novel doping schemes were investigated toward this end. Finally, a circadian light source has also been developed that can affect physiological changes in humans, and a light box for entrainment of circadian rhythms in rats has been built.

CHAPTER I

INTRODUCTION

A novel broadband spectrally dynamic solid state illumination source (BSDLED) has been developed that uses a dual wavelength light emitting diode (LED) and combinations of phosphors to create a broadband emission that is real-time controllable. Six major focuses of this work were as follows: (1) creation of a two terminal dual wavelength LED with control of the relative intensities of the two emission peaks; (2) bandgap modeling of the two terminal dual LED to explain operation based on the doping profile; (3) novel use of phosphor combinations with dual LEDs to create a broadband spectral power distribution that can be varied to mimic a blackbody radiator over a certain range; (4) investigation of novel doping schemes to create tunnel junctions or equivalent buried current spreading layers in the III-nitrides; (5) optical modeling of a three terminal dual LED; (6) development a novel light source that interacts with the human circadian system.

The lighting industry is on the cusp of a major revolution with the development of new illumination sources based on light emitting diodes called solid state lighting (SSL) [29]. Traditionally, LEDs have been used as indicator lights, replacing small incandescent lamps and have only recently become widespread in niche applications such as signage, backlighting, mobile devices, traffic signals, and large area displays. However, no significant penetration has been achieved in general illumination because suitable sources do not yet exist. In some applications one or more of the following key attributes make solid state sources attractive alternatives to conventional illumination technologies: saturated color, small size, energy efficiency, robustness, and controllability. However, in general illumination different criteria such as broadband, high color rendering capability and appropriate correlated color temperature make the adoption of SSL more difficult. Additionally, it is important to eliminate gaps in the power spectrum of sources to achieve high quality white light, especially for color rendering purposes and possibly human factor effects [48]. An example of this is shown in

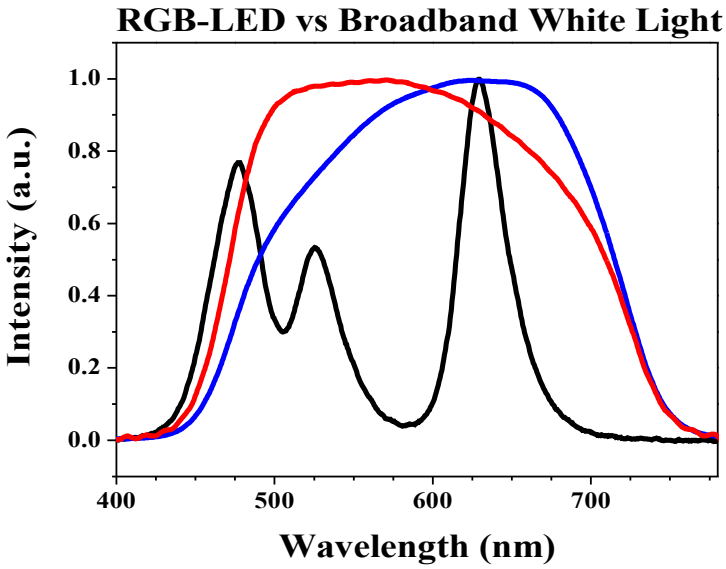

Figure 1: RGB LED SPD compared to two different broadband SPDs.

Figure 1, where broadband sources are plotted against a red-green-blue LED (RGBLED) source; the drastic differences in the power spectra can be observed. In fact, in many cases designers and architects are seeking added functionality such as dynamic spectral control, also exemplified by the two different broadband spectra shown in Figure 1. No available SSL technologies incorporates all the necessary attributes for general illumination. Thus, there is a need for novel devices that lend themselves to a SSL general illumination solution.

A dual wavelength LED has been developed with the ability to control the relative intensity of the two emission peaks through two terminal operation. A novel solid state general illumination source has been developed based on a metal organic chemical vapor deposition (MOCVD) grown, gallium nitride (GaN), multi-quantum well (MQW) light emitting diode. Two device structures were envisioned for this work, including a three terminal device structure consisting of two LEDs emitting at two distinct wavelengths monolithically grown and a two terminal device with two MQW regions that emit different wavelength of light. Both devices could be used to excite two or more phosphors with different excitation spectra, Figure 2. The combined phosphorescence spectrum can then be controlled by adjusting the relative intensities of the two LED emissions. Phosphor analysis shows such a scheme to be

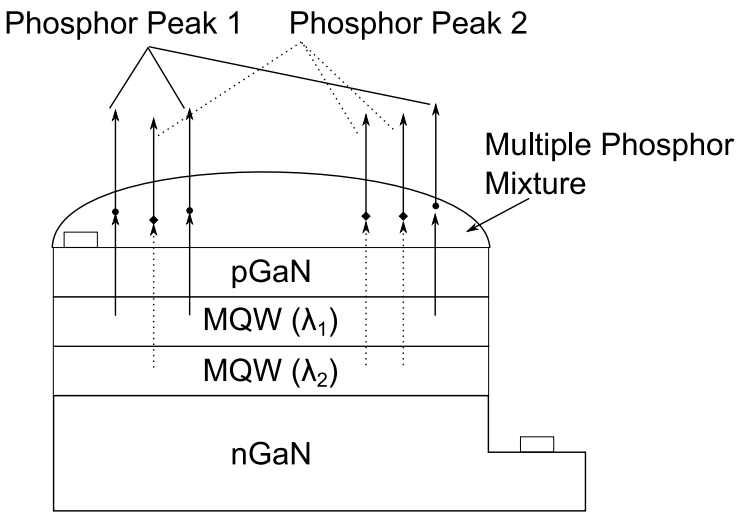

Figure 2: Schematic of Dual LED exciting multiple phosphors

viable for use in a broadband spectrally dynamic general illumination source.

The final BSDLED in this work is based on a novel two terminal dual LED. This device design is simpler than the three terminal dual LED and does not rely on the use of III-nitride tunnel junction. The development of a suitable III-nitride tunnel junction proved to be the prohibitive element of a three terminal dual LED.

One focus of this work was the development of improved buried current spreading layers for use in the three terminal dual LED structure. Previous three terminal dual LED structures [51] have not been adopted for widespread use because of inefficiencies associated with tunnel junctions (TJ) used to contact the buried p-type layers. A new hybrid p-doping technique as well as SPS doping and the effects of Mn on tunneling have been investigated to address this issue. Tunnel junctions have been reported in GaN; however, no systematic work considering standalone tunnel junctions in GaN exists, leaving a lack of understanding concerning the mechanisms of current flow in these structures.

A second focus of the work sought to maximize light output of the dual LED structures. Optical modeling was used to investigate the effects of reabsorption between the two MQW regions. If necessary, the incorporation of Bragg type reflective layers and their influence on light output was studied.

Another focus of this work has been the incorporation of multiple phosphors with the

dual LED to achieve a broadband spectrally dynamic solid state illumination source. Preliminary analysis shows that a broadband spectrally dynamic solid state illumination source using multiple phosphors is possible. This is the first known work to consider a broadband spectrally dynamic solid state illumination source.

A fourth focus was the development of light systems that interact with the mammalian circadian system. A light source that mimics the change in daylight over the period of a day has been developed. Also, a light box for investigating the effects of colored light on the circadian system of rats has been developed that uses LED as the light source.

1.1 SSL History

Solid state lighting is lighting or illumination using light emitting diodes. The recent development of high brightness LEDs (HBLED) has enabled the potential for a solid state revolution to take place in lighting/illumination similar to what has occurred in the microelectronic and display industries. Incandescent bulbs and fluorescent tubes are essentially vacuum tube technologies similar cathode ray tubes (CRT) for displays and vacuum tubes predominant in early electronics. Solid state light sources offer many advantages to conventional light sources including higher efficiency, longer life, smaller size, greater robustness, and others. However, a transition to solid state lighting technology in general illumination will be more difficult than microelectronics or displays because of the characteristics of the source and the preexisting electrical infrastructure.

The first electrical distribution system was built to provide power for incandescent light bulbs used in general illumination. Since then power distribution and lighting have been developed in coordination with each other. The existing infrastructure is primarily built for lamps operating at higher voltages (120 volts) than required for solid state lighting. Thus, some change in infrastructure may be required and is long overdue with the widespread use of consumer electronics that rely power with voltages in the range of that for SSL.

The widespread use of LEDs in lighting dates back only about a decade (mid 1990s); although, GaP and InAlGaP LEDs emitting in the red to yellow part of the spectrum date back to 1960's and 1970's. The major obstacle was creating suitable emitters in the green

to blue part of the spectrum and it was not until the development of InGaN-based blue and green LEDs that solid state lighting could be viewed as a feasible technology. In 1969 Maruska reported depositing the first GaN single crystal film using hydride vapor phase epitaxy and in 1971 Pankove reported the first electroluminescence using Zn doped GaN. Then in 1972 Maruska achieved violet (430 nm) emission using Mg doped GaN (GaN:Mg). Between 1972 and 1986 little work was published in this area until Amano et al used aluminum nitride (AlN) buffer layers to greatly increase the crystalline quality of metal organic vapor phase epitaxially (MOVPE) grown GaN. However, it was not until 1989 that Amano and Akasaki created conducting p-type GaN:Mg by post growth treatment of low energy electron beam irradiation (LEEBI) leading to the possibility of high brightness emitters. It would take another pioneer in 1995, Nakamura, with his novel growth technique and GaN buffer layers to make GaN devices a viable solid state lighting technology with efficiencies greater than ten percent. At Nichia, Nakamura used heterojunction structures to create the brightest GaN light emitting diodes at that time. Today, white broadband LEDs are capable of producing greater than 100 lumens and efficiencies greater than 100 lm/W. These metrics are rivaling, and sometimes beating, those of other general illumination sources like incandescent and fluorescent bulbs.

SSL sources have advantages over conventional light sources, including higher efficiency, longer life, smaller size, and enhanced controllability among other characteristics. The energy savings promised by SSL could be extensive[29], while the longer lifetime reduces cost of ownership and allows for greater integration of lighting into the architectural space. In addition, the smaller size and enhanced controllability of SSL over conventional illumination offers designers more freedom to create novel devices and fixtures while adding functionality.

SSL has already made a significant impact in several niche markets such as signage, displays, traffic signals, backlighting, and others where the features of LEDs are well suited for the application. However, no major penetration into general illumination has been achieved for SSL although automobile interiors are increasingly being illuminated by solid state lighting. The major differences between the proven SSL markets and illumination are direct versus indirect lighting, total light output, and the quality of white light. Lighting

designers must fully understand the characteristics of LEDs and how they differ from other lamps to fully exploit the advantages of SSL. Furthermore, innovative SSL system designs will be a major catalyst in the success of this technology in general illumination.

1.2 Motivation

Solid state lighting shows potential for energy savings and design flexibility, with the possibility for radically new illumination solutions. General illumination is the largest sector of the lighting market and the greatest potential for energy savings. However, as solid state lighting develops into a general illumination technology, it will be important for designers to exploit the attributes of LEDs to create innovative sources that provide customers with new functionality and quality as well as replacement of old lamps. If novel designs are not pursued and solid state lighting is viewed as a retrofit replacement for conventional light sources, it is likely that LEDs will be met with the same slow acceptance that has hindered the compact fluorescent lighting sector or complete failure as a general illumination technology.

The United States Department of Energy and Optoelectronics Industry Development Association (OIDA) estimated in a 2001 report that by 2025 SSL could reduce the global amount of electricity used for lighting by 50%. This would lead to a cumulative savings potential in the US alone of 16.6 Quads (760 GW) of electrical energy, thereby eliminating 258 million metric tons of carbon emission and alleviating the need of 133 new power stations (1000 MW each) [29].

The smaller size, longer life, and greater controllability, among other attributes of SSL sources, enable new fixture designs unrealizable using incandescent or fluorescent bulbs. For example, incorporation of illumination systems into building infrastructure is an option with solid state lighting sources because they have lifetimes greater than other technologies utilized in the building infrastructure. Designers may consider existing parts of the environment as potential illumination sources for example, doors or windows. These new illumination systems require new fixture designs to properly distribute the light using LEDs that closely resemble point sources. During the SSL source design process, the differences

from traditional sources should be considered to create radically different illumination systems because the cost of LEDs is higher than incandescent bulbs and it is unlikely that the price will be matched in the near future. Therefore, incentives such as added functionality, must be incorporated to entice early adopters until a critical mass is reached and economies of scale can drive down costs to better compete with traditional sources.

Dynamic lighting, that has the ability to adapt to the number of people, time of day, or occasion for a particular space is possible using one SSL source. Control is achieved easily with LEDs because they are relatively narrow band emitters compared to incandescent or fluorescent sources and have fast switching speeds. In addition, by pumping the appropriate phosphors broadband dynamic solid state light sources can be achieved. A wide color gamut including many shades of white can be realized by proper mixing, and this can be tuned as desired with a control system.

Developers must think beyond the scope of todays lighting systems. Illumination for visual acuity has long been the primary function of illumination, but as the illumination industry has matured the psychological aspects of illumination have been considered by designers; for example, choosing a particular lighting distribution or color variation in retail applications. The next step in the evolution of illumination is to consider the physiological effects of illumination that cause biological changes in a person within the environment. As described later LEDs may play a major role in such systems. It is only through innovative designs that SSL may gain a true foothold in the illumination market and potentially be a disruptive technology.

1.3 State of the Art

The state of the art for SSL is continually developing at every level of the technology including in materials and growth, packaging, and systems. Applications for LEDs have grown to include large area displays, traffic signals, mobile phone backlights, various automotive applications, as well as many others. Advanced LED chips and packages have also been developed beyond the well known 5 mm package to accommodate growing needs. Lastly, fixtures designed specifically for SSL sources are being tailored to meet the requirements of

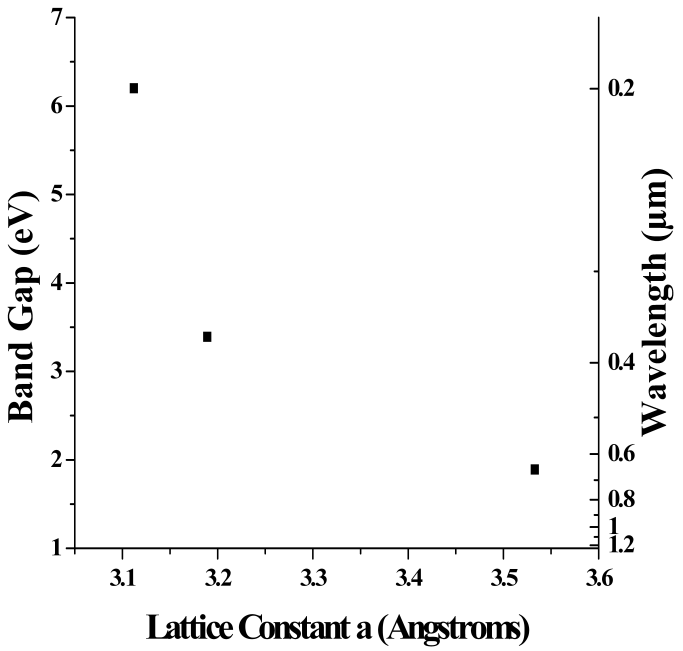

Figure 3: Band Gap vs. Lattice Constant for III-Nitrides

general illumination based on the attributes of the LEDs.

1.3.1 Materials & Growth

Commercially available LEDs are almost exclusively grown by metal organic chemical vapor deposition (MOCVD) in material systems including aluminum gallium arsenide (AlGaAs) for Red, aluminum indium gallium phosphide (AlInGaP) for red to yellowish green, and aluminum indium gallium nitride (AlInGaN) for green to UV. Figure 3 shows the material system bandgaps versus lattice constant. Most current device structures incorporate multi-quantum well (MQW) active regions to enhance light output, usually comprised of gallium nitride and indium gallium nitride (GaN/InGaN) alternating layers, and can be designed to emit a desired wavelength of light covering almost the entire visible spectrum. Magnesium (Mg) and silicon (Si) are the most common p-type and n-type dopants, respectively. A basic LED structure is shown in Figure 4 although thicknesses and exact details of the structure vary by design.

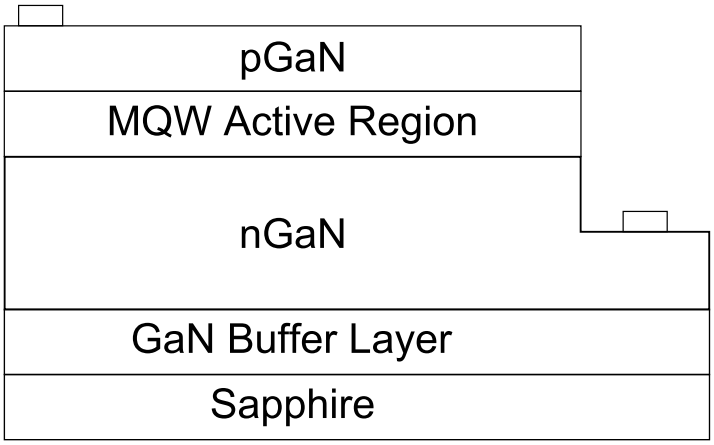

Figure 4: Schematic structure for a common III-nitride LED

1.3.2 Chip Fabrication

Die fabrication for LEDs typically employ cleanroom processing techniques such as photolithography. Once a pattern is transferred to the wafer, dry plasma etching and metal evaporation are used to define the mesa structure and deposit metal contacts, respectively. More advanced chip designs involve surface roughening techniques and die shaping to improve light extraction[32, 64]. There is also substantial work in p-type metalization schemes to improve contact resistance and increase light output such as low resistance ohmic transparent contacts. This is discussed in further detail in Section 2.2.3.

1.3.3 Packaging

Packaging is one the most important areas of SSL source development because it will define how well the light is extracted and in what pattern, how heat is to be dissipated, and how phosphor is applied. Typically, an epoxy encapsulation is formed on top of the device to act as a protectant and a lens is attached to properly distribute the light in lambertian, batwing, or other patterns. High power packages include a method for effectively removing heat generated at the junction. The luxeon package developed by Lumileds is an example of a new package developed for high power LEDs. Different lens shapes provide required distribution patterns and the back of the package serves as a face that can be attached to a heat sink for thermal management.

Phosphor development has been widespread for LED phosphor converted devices. Yttrium aluminum garnet (YAG), a scintillator (although typically referred to as a phosphor), absorbs photons with wavelengths in the blue part of the spectrum and has a relatively broadband emission peak at 550 nm (yellow/green light). White light is produced when some of the blue light is transmitted and mixed with the yellow light; however, this light is lacking in the red part of the spectrum and suffers in color rendering tasks. Red-emitting phosphors have been developed and incorporated with the YAG to provide higher quality white light to compensate for this. Another solution is to use orange, yellow, green, and blue phosphors pumped with a 400 nm device. A desired color can be achieved by properly mixing the phosphors.

1.3.4 Applications & Systems

Traffic signals and large area displays are two of the most prominent niche markets where colored LEDs have become very successful. However, one of the biggest drivers for the solid state lighting market has been the use of LEDs as backlights in mobile phones. LEDs are ideally suited for backlighting because of their small size, high efficiency, and low output requirements. They are especially useful in embedded designs where their long lifetime means they will outlive the product into which they are incorporated. Another emerging market is automotive lighting where LEDs are used as taillights, interior illumination, dash backlighting, and soon headlights. Designers have more flexibility due to the small size of the LEDs. In addition, LEDs are suited for the harsh environment of automotive lighting requirements because they do not require a fragile glass bulb.

Dynamic sources that can change their output over time are also being realized using LEDs. Applications such as wall washes and decorative lighting are markets where LEDs coupled with control circuitry are becoming widespread. Color Kinetics is a market leader and has developed many sources for these applications.

SSL is also very well suited for remote lighting applications where the power source, a battery or solar cell, can operate as low voltage direct current power sources. In many cases the quality of the light can be sacrificed for high efficiency and long lifetime. For example,

programs such as Light Up The World install such devices in remote regions of the world where an integrated power grid does not exist, yet there is need for light after the sun sets.

To date, no significant penetration has been observed in general illumination. However, many manufacturers and researchers are developing solid state lighting sources to meet the needs of general illumination. Power drivers have also been specifically developed for driving LEDs from a standard alternating current line. LEDs operate on much lower voltages ($<$ 5 Volts) than the 120 or 220 volts that are common in North America and Europe. Some of these drivers have included control circuitry to provide dimming of SSL sources. LEDs are typically dimmed by operating them with a pulse width modulation scheme instead of constant current.

Organic LEDs (OLEDs) have also been a major area of research. These devices are large area emitters instead of point sources. OLEDs have the potential to be manufactured on a reel to reel type system with either glass or plastic substrate, which could be a very economic manufacturing process. However, the development of these devices lag inorganic LEDs with lower light output (150 lumens for 6'x6' panel), shorter lifetimes (10,000 hours), and lower efficiencies (30 lm/W).

1.4 Innovative Illumination Sources

Solid state lighting has many potential advantages over conventional lighting technologies; however, this may not be enough to realize significant penetration into the general illumination market. It is unlikely that LED prices will reach the substantially lower prices of incandescent bulbs in the near future. In light of this, designers will need to create innovative devices that provide a competitive advantage over conventional illumination sources. Relative small size, long life, increased robustness, high efficiency, and added controllability are attributes that lend themselves to the creation of innovative illumination systems that can be integrated into the building infrastructure, respond dynamically to environmental changes, or cause biological effects in the illumination subjects.

Solid state lighting presents a new paradigm for illumination controllability. Certain characteristics of the illuminated environment can be manipulated using multiple LEDs

of different emission wavelengths as the illumination source. This enables a new, versatile, general illumination source achieving new effects beyond the visual that are not possible with conventional light sources. Visual acuity has long been the primary function of illumination, but as the illumination industry has matured the psychological aspects of illumination have been considered by designers; for example, choosing a particular illumination distribution or color variation in retail applications. The next step in the evolution of illumination is to consider the physiological effects of illumination that cause biological changes in a person within the environment.

Recent biological research has investigated the relationship between human internal clocks, the circadian rhythm, and light. Studies show that certain circadian rhythms can be entrained with light [38]. Moreover, blue light at 460-470 nm has been shown to elicit the greatest circadian response[6]. Thus, disorders such as jet lag, shift work sleep disturbance, age-related insomnia, advanced- and delayed-sleep phase syndromes, and SAD (seasonal affective disorder) can be addressed. However, many uncertainties still exist in this field and more work is required in this field which proper tools can greatly facilitate.

Human biological systems are complex and not well understood, especially the human eye. Although it is widely accepted that vision is primarily mediated through cells known as rods and cones contained in the eye, biologists have realized that there are functions of the eye other than vision[5, 3]. There are cells in the eye that are believed to have the ability to reset certain biological systems when the correct amount of light is present.

A circadian rhythm is one with a cycle of about 24 hours. Circa means about and dia means day, giving: about a day or 24 hours. This internal clock is reset daily with light, which is received by photoreceptors in the body and affects our propensity to sleep or wake. Core body temperature, sleep schedules, and other physiological behaviors, are regulated by this clock. The action spectrum in Figure 5 denoted as melatonin response gives evidence to the importance of spectral content of the source, because it represents the response of the human circadian system to varying colors of light[6]. An important note is the peak around 464 nm.

The current state-of-the-art in circadian light therapy devices consists of bright white

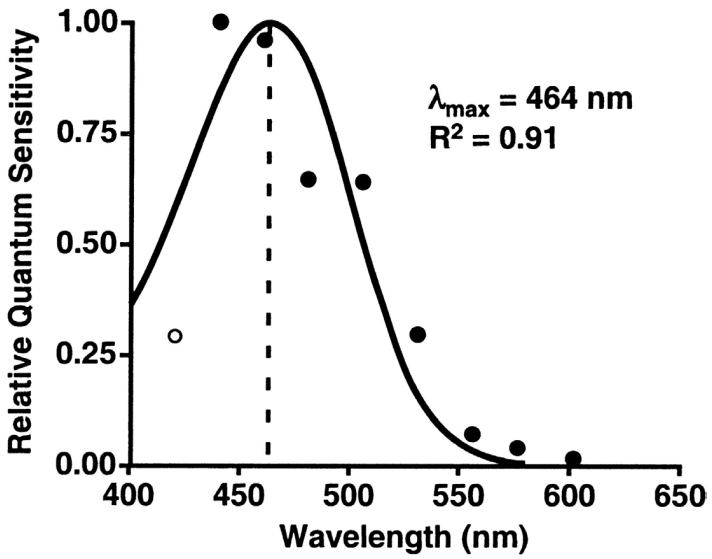

Figure 5: Action spectrum for melatonin secretion in humans

light boxes. These are used to irradiate a certain amount of light onto a subject for a specified period of time. Until recently, it was widely believed that brightness and exposure were the only important parameters in the light therapy. The evidence presented here shows that wavelength of light plays some role in circadian entrainment. The color does matter because of the way cells work, having peak responses at certain wavelengths. Solid state lighting has the ability to efficiently interact with the human circadian system on this premise.

One incarnation places circadian light devices in airplanes much like reading lights to mitigate the effects of jet lag. Each traveler would have a personal circadian light system for their specific schedule. Depending on the length or purpose of their stay the source could help them adapt accordingly. Another set of sources in the cockpit could help to keep the pilots more alert especially during transcontinental flights. This is an example of the innovative incorporation of solid state lighting in an environment that provides new functionality. Solid state lighting must employ new features offered by LEDs in coordination with the current understanding of light and how it interacts with the human body. Current lamp technologies are limited in their abilities to do this because they are designed for one function and typically only the intensity can be controlled.

CHAPTER II

BACKGROUND

2.1 Literature Survey

Dual wavelength LEDs and conventional LEDs incorporating tunnel junctions have been reported in III-nitrides. However, no systematic investigation on standalone tunnel junctions in III-nitrides is present. Additionally, low series resistance short period superlattice (SPS) structures have been reported but not as buried current spreading layers. Further investigation into these structures is necessary to optimize them for use in a dual LED. Reports of controlling phosphor combinations by multiple pump wavelengths do not exist in the literature or industry, while combining phosphors for a static device is common.

2.1.1 Tunnel Junctions and Three Terminal Dual LEDs

A dual wavelength indium gallium nitride quantum well light emitting diode was developed for applications that use fluorescence labeling of biological systems as a diagnostic technique[51] but is not in widespread use in other applications. This device consisted of three terminals with a tunnel junction underneath the middle terminal, Figure 6[51]. The tunnel junction was used as a current, spreading contact layer to the p-type layer of the bottom device. The presence of the tunnel junction in the bottom device allowed for electrically isolated devices but typically added about 1 volt to the forward voltage characteristics of the bottom device. Thus, the bottom device has higher series resistance, as seen in Figure 7, and should be improved. Optimization of the tunnel junction will provide an in-situ contacting method with suitably low voltage drop. Takeuchi et al. reported on a LED with a tunnel junction as the top contact that has been optimized with only a .6 V drop across the tunnel junction[62]. The tunnel junction is the same structure as the one used in the dual wavelength device and could lead to an improved dual wavelength emitter. However, a .6 V drop across the tunnel junction will likely be too large to develop a dual wavelength

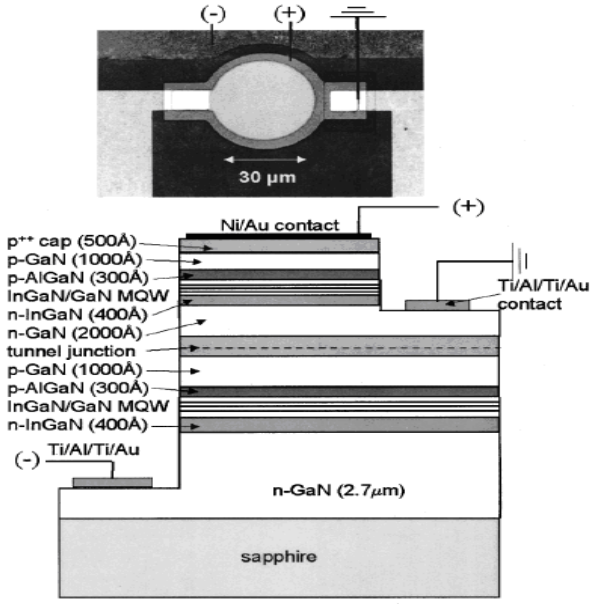

Figure 6: Ozden's dual wavelength LED with three terminals.

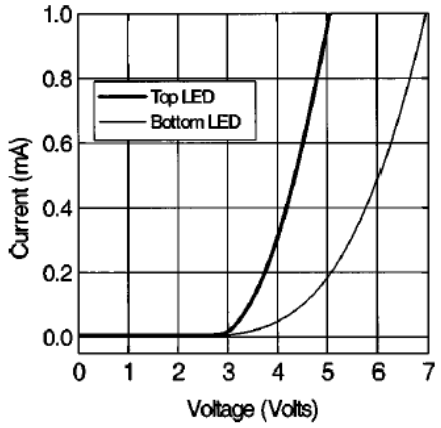

Figure 7: The current-voltage characteristics Ozden's Dual LED.

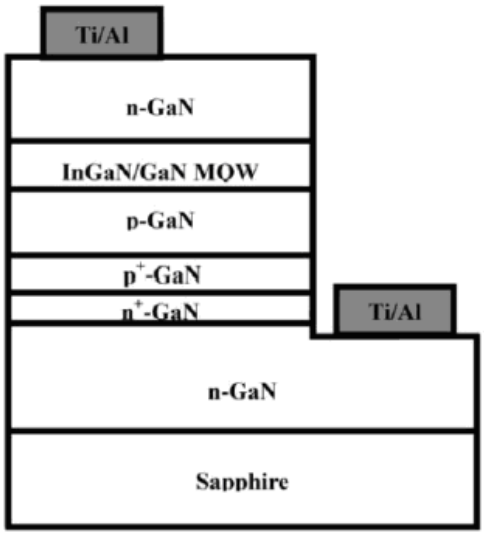

Figure 8: Previously reported inverted LED structure using TJ as buried contact.

LED suitable for widespread use. In addition, emission from the tunnel junction incorporated device typically consists of a random distribution of μm size bright spots that are thought to originate from local compositional or doping inhomogeneities within the TJ[51]. These effects are not reported in all literature on GaN tunnel junctions, and further investigations, including temperature dependent current-voltage measurements and infrared and optical microscopy, will lead to a better understanding of the current injection mechanism.

In reports published previously to Ozden's dual LED work, tunnel junctions were used in a more common application as top current spreading layers[25, 26]. A higher series resistance was observed for the TJ-LED compared to a LED with a semitransparent metal top current spreading layer. However, the TJ-LED had a higher external quantum efficiency due to the increased light transmission of the fully-transparent tunnel junction. Chi-Ming Lee et al.[35] have also reported on the growth of an inverted LED structure, Figure 8. This device has significantly higher forward voltage at 20mA (7.5 V compared to 3.5 V for typical LED) but exhibits a total efficiency of 17% compared to 9.5%[35]. The inverted LED is similar to the bottom LED of a three terminal device. M. Diagne, Y. He et al.[15] have shown that a tunnel junction can be used as a current spreading layer in a vertical cavity light emitting diode with an AlGaN/GaN distributed Bragg Reflector on the bottom of the device. The device structures reported to date use a n+GaN/p+InGaN junction for tunneling and all

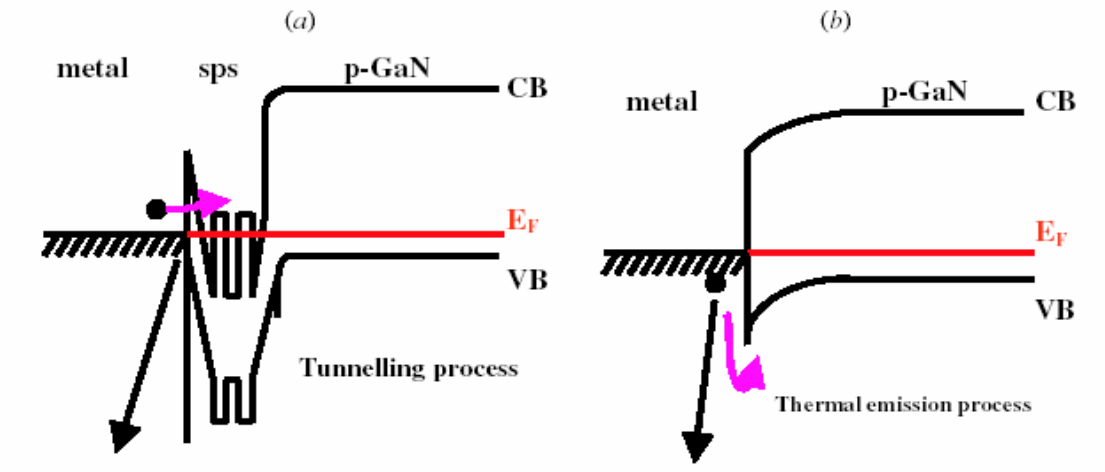

Figure 9: Energy band diagrams of (a) metal/SPS/p-GaN and (b) metal/p-GaN.

have higher series resistance than a LED with a semitransparent current spreading layer. However, a report on a LED with a Si-doped $In_{0.23}Ga_{0.77}N$/GaN short-period superlattice (SPS) tunneling contact layer shows lowered series resistance relative to a LED with a semitransparent top current spreading layer[58]. The reduction from 3.8 V to 2.95 V at 20 mA forward bias and reduced series resistance of 40 Ω to 11 Ω is thought to be due to the decreased contact resistance of the $In_{0.23}Ga_{0.77}N$/GaN (SPS)/Ni/Au versus p-GaN/Ni/Au. In addition, Liu et al report similar results and describe the band structure as shown in Figure 9[40]. There have been no reports on SPS structures used for buried contacts and how this affects overgrowth, contacting, or current spreading. The p+ layer of the tunnel junction may be improved by using a Mg-doped InGaN/GaN superlattice as suggested by Kumakura et al.[30]. They report hole generation of above $10^{19} cm^{-3}$, which may help lower the barrier to tunneling in a device. In addition, Kauser et al. suggest that this structure may be optimized by grading the indium composition in the InGaN regions[28]. There are no current reports of tunnel junctions incorporating Mg-doped InGaN/GaN superlattices. A significant piece of this work was the optimization of p and n type superlattices and junctions using those structures. An individual analysis of the tunnel junction without incorporated LED is missing from current literature concerning tunnel junctions in GaN based materials. A substantial body of work concerning Si tunnel junctions considers the details of the current-voltage characteristics of a tunnel diode[12, 41, 56, 17, 14, 42], and

can be used as a basis for further investigations of GaN based tunnel junctions. This will be discussed in more detail in Section 4.

2.1.2 Phosphor Combinations

There exist several LED manufacturers (Lumileds, Nichia, etc.) using combinations of phosphors to produce a desired spectrum visible as white light. However there are no manufacturers or any type of reports on a device that is designed to excite two or more phosphors differently with different energy photons to create a broadband spectrally dynamic white light source. This is a novel device, as it has not been developed previously, even though the dual LED, and phosphor combinations have been used for other devices.

2.1.3 Literature Search Summary

In summary, the innovations of this work include the further investigation of GaN based tunnel junctions and the development novel device that is a broadband spectrally dynamic solid state illumination source. The novel device relies on the exploitation of different phosphors with distinct excitation spectra and the use of a dual wavelength emitter to pump the phosphors. Such a device has not been reported to date.

2.2 Experimental Setup

2.2.1 MOCVD Growth

2.2.1.1 Overview of MOCVD

Metal-organic chemical vapor deposition (MOCVD) is the common name used for organometallic vapor phase epitaxy, although it does not strictly agree with general chemical nomenclature. MOCVD is a growth process used for semiconductor materials and devices. Specifically it is commonly used for growth of III-nitrides. The III-nitrides include AlN, GaN, InN and any ternary and quaternary alloys of those materials. The other common technique for growth of III-nitrides is molecular beam epitaxy (MBE), although it is only typically used for research of these materials. On the other hand, MOCVD is better suited for large scale growth and is used for manufacturing as well as research of III-nitrides. A very basic synopsis of MOCVD is the following. Gases, some of which are metal-organics, are

introduced into a heated chamber containing a substrate on which crystalline growth occurs. In the chamber the gases undergo a chemical reaction to form a chemical compound which is then incorporated into a crystalline structure present on the substrate. In this way an epitaxial layer is formed and the crystalline semiconductor is grown. In the case of III-nitrides, some combination of trimethylaluminum (TMAl), trimethylgallium (TMGa), trimethylindium (TMIn), gaseous ammonia (NH_3), and possibly gaseous hydrogen and nitrogen are introduced into a chamber heated to between 500°C and 1100°C. These gases then react to form an alloy of AlInGaN with the Al, Ga, and In compositions dependent on a number of factors including relative gas compositions and temperature. MOCVD is a complex process and many of its aspects are not fully understood[60]. The common growth model for MOCVD processes is subdivided into thermodynamic and kinetic reactions[60], where the thermodynamic model deals with the overall driving force for the process and the kinetic model is used to understand the rate at which each step of the overall process occurs. Hydrodynamics and mass transport play an important role in the growth process and determine the rate at which material reaches the growth interface. The rates at which chemical reactions occur and the surface details of the structure are also important to the overall process. Certain aspects of the growth process will be dominated by these factors leading to two growth regimes: the kinetically limited case where the reaction rate limits the growth rate and mass transport limited case where the amount of material arriving at the growth interface limits the growth rate. The theory behind MOCVD growth will be discussed in more detail in the following section

2.2.1.2 Growth Rate

MOCVD is a pyrolysis process. MOCVD growth is considered to occur in a mass-transport-limited regime meaning that the interface kinetics are much more rapid than the diffusion (mass transport) kinetics. Typically in III-V MOCVD growth the V/III ratio is $\gg 1$, and thus the growth rate is mainly limited by the amount of the III atoms present at the interface[60]. The mass-transport-limited case is true for growth temperatures above 800°C. Thus, film growth rates ($\dot{G}$) depend on gas partial pressures (P) and flow rates ($\dot{V}$)[50]. For

example, in $Al_xGa_{1-x}As$

$$\dot{G} = K(T)[P_{Ga}\dot{V}_{Ga} + 2P_{Al}\dot{V}_{Al}] \quad (1)$$

$$x = \frac{2P_{Al}\dot{V}_{Al}}{2P_{Ga}\dot{V}_{Ga} + P_{Ga}\dot{V}_{Ga}} \quad (2)$$

where K(T) is a temperature dependent constant.

2.2.1.3 Precursor Molecules

The most common Group III precursor molecules used in MOCVD of GaN are trimethylgallium (TMGa), trimethylaluminum (TMAl), trimethylindium (TMIn), and triethylgallium (TEGa). These compounds are relatively volatile and undergo pyrolysis in the MOCVD growth process. They are also pyrophoric, but stable enough to be kept indefinitely at room temperature before use[60]. TE molecules are available for Al and In as well, however TM molecules are generally preferred because of their higher vapor pressure and increased stability. TE molecules however lead to significantly less carbon contamination in the GaAs and AlGaAs[60, 21], since they do not pyrolyze into group III atoms and CH_3 radicals that decompose into C in the epitaxial layer.

The group V precursor most commonly used in GaN MOCVD is ammonia (NH_3). NH_3 however, is highly stable decomposing only 15% at 950°C. This high stability and the large bond strengths of GaN neccesitate high growth temperatures. Furthermore, nitrogen is highly volatile, and at high growth termpartures high concentrations of nitrogen vacancies are formed, making high quality growth of III-Ns difficult[60].

Dimethylhydrazine (DMHy) has been suggested as a nitrogen precursor for GaN growth at lowered temperatures[43, 36] similar to the growth temperatures of InGaN used in the MQW regions. DMHy decomposes much more efficiently at the lower temperatures thus enabling high quality film growth [52]. In addition, it has been reported[52] that p-type GaN growth with DMHy eliminates the need for thermal activation of acceptors. However, relatively high ($> 10^{19} cm^{-3}$) levels of oxygen and carbon have been observed in material growth with DMHy[60].

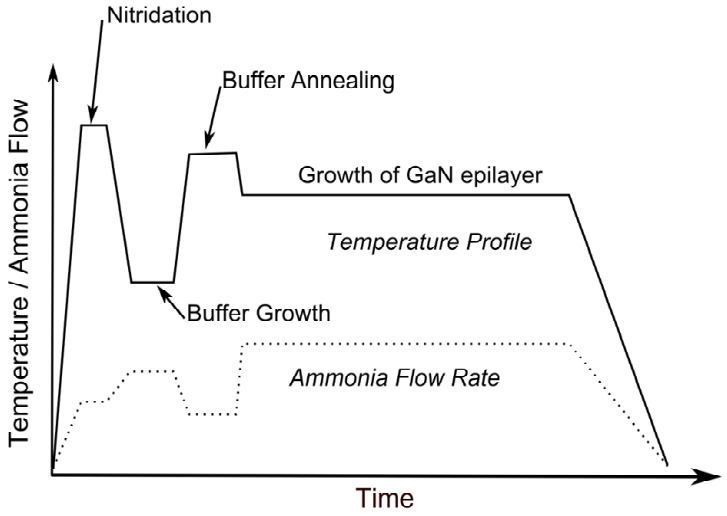

Figure 10: Sketch of typical GaN growth process

2.2.1.4 MOCVD of Group III Nitrides

MOCVD of GaN: Gallium Nitride is most commonly grown by MOCVD on sapphire substrates with orientation (0001). A number of critical steps must be performed to achieve high quality GaN growth on sapphire including: pre-growth nitridation, buffer growth, and buffer annealing. Figure 10 is a schematic showing temperature and ammonia flow with time for a typical GaN growth. In the pre-growth nitridation step the substrate is heated to temperatures above 1000°C under NH_3 ambient. This first purpose of this step is to reorganize and improve the surface[21]. Secondly, nitrogen compounds from NH_3 are formed on the surface, which is called nitridation, and aids in the growth of high quality material[21]. Next the substrate is cooled to a temperature around 500°C, and a buffer layer of GaN is grown. The buffer layer is then heated under ammonia flow to "recrystallize" and stabilize the surface, since it is of very low crystalline quality. Finally, the high temperature GaN is grown on top of the buffer. After the "recrystallization" step the buffer layer is still of low crystalline quality compared to the high temperature GaN, but acts to promote growth of high quality GaN, because the interfacial energy between high temperature GaN and its buffer is lower than that for high temperature GaN grown directly on sapphire. The lower interfacial energy enhances lateral growth of the high temperature GaN on the buffer,

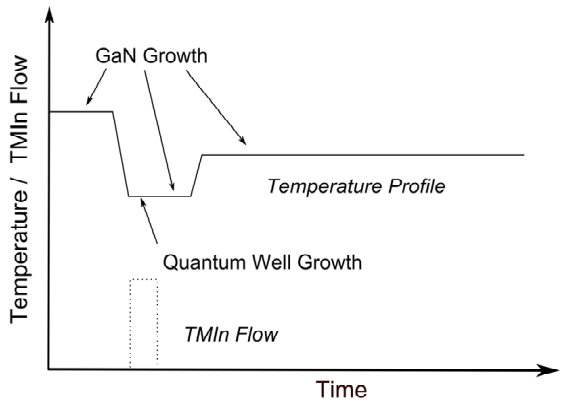

Figure 11: Schematic of a GaInN/GaN QW growth

resulting in a flat surface.

Growth of GaInN GaInN is of great importance for LEDs as it makes up the quantum well layers used in typical III-ntiride LEDs. Growth of GaInN has not proven trivial, however. In has a much higher vapor pressure than Ga creating difficulty in growth of In rich alloys. Typically, growth of GaInN material is performed at reduced temperatures from normal GaN growth between 500°C and 850°C. In incorporation decreases as temperature is increased. Maximization of the crystalline quality of the material requires increasing the growth temperature as much as possible. Growth of GaInN in this work was almost exclusively part of a GaN/GaInN superlattice or multiquantum well structures. Two optimum growth temperatures exist for the two materials in these structures. A schematic for a typical quantum well growth is shown in Figure 11. The GaInN is grown at a reduced temperature for the desired In content, then a thin layer of GaN is grown at the same temperature to protect the GaInN layer from a subsequent temperature ramp where GaN is grown again. The higher temperature for the GaN growth is ∼900°C which is not ideal for GaN growth but is optimzed between crystalline quality and damage to the underlying GaInN layer.

2.2.2 Characterization

Characterization of material and devices involved in this work includes non-destructive techniques such as photoluminescence (PL), x-ray diffraction (XRD) and atomic force microscopy (AFM), as well as destructive techniques such as Hall effect, electroluminescence (EL), current vs. voltage (IV), light vs. current (L-I) and secondary ion mass spectrometry (SIMS). these techniques are powerful tools in the research of new materials by providing feedback for the development process. Ultimately, for light emitting diodes EL, I-V and L-I measurements provide the performance metrics that determine the quality of the end device, however, they do not often provide enough information to fully understand issues in a device. The other techniques mentioned, such as PL, XRD, SIMS, Hall effect and AFM can provide insight into specific material issues that may be hindering device performance. Each of these techniques is discussed in further detail in the following sections. Additionally, the specific setup for this work is discussed for each technique.

2.2.2.1 Photoluminescence Spectroscopy

Photoluminescence is defined as luminescence in which the excitation is produced by visible or invisible light. Light when directed onto a sample is absorbed and imparts excess energy into the material in a process called photo-excitation. One way this excess energy can be dissipated by the sample is through the emission of light, or luminescence. In the case of photo-excitation, this luminescence is called photoluminescence. The intensity and spectral content of PL is a direct measure of material properties. Photo-excitation moves electrons into excited states. On return to equilibrium states excess energy released and may include the emission of light (a radiative process) or may not (a non-radiative process). The energy of the emitted light (PL) relates to the difference in energy levels. The quantity of emitted light is related to contribution of radiative process. The permissible electron states involved in radiative recombination can be: band-to band, donor to valence band, conduction band to acceptor. Non-radiative recombination can occur via an intermediate state. The schematic of these cases is shown in Figure 12. Shallow levels, near the band edge, participate in radiative recombination, but temperature must be low to discourage thermal activation.

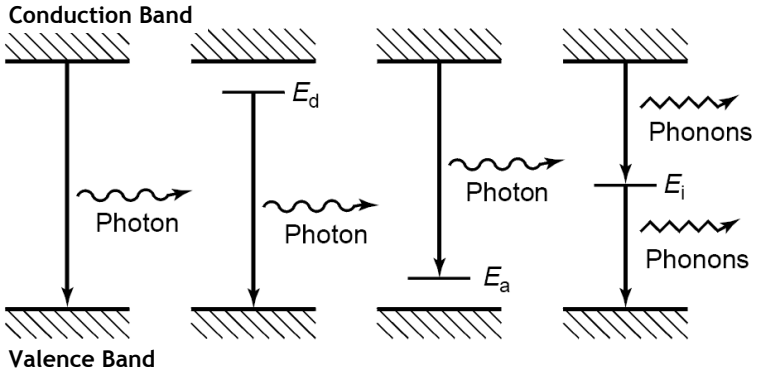

Figure 12: Possible recombination processes for excited electron.

Deep levels facilitate non-radiative recombination.

In crystalline material, such as semiconductors, translational symmetry leads to formation of electronic energy bands. Defects/impurities perturb band structure creating a discrete energy level within the bandgap. Depending on the defect or impurity, the state acts as a donor or acceptor, or other intermediary state. On radiative recombination, the energy of the emitted light can be analyzed to determine the energy of defect/impurity level. PL spectroscopy measurements are commonly performed on semiconductor materials by shining an intense light, usually a LASER, onto the sample and then collecting the PL from the semiconductor sample. A schematic of how a PL setup might work is shown in Figure 13. PL spectroscopy is a contact-less, nondestructive, simple and versatile method of probing the electronic structure of materials. A typical ordinary PL spectroscopy setup requires:

- Optical Source
- Optical Power Meter/Spectrometer
- Focusing Optics
- Camera/Detector

The optical source is typically a LASER that is either continuous wave or pulsed. The photonic energy of the LASER is usually higher than the band-gap of the target material so as to excite all PL energy states. The spectrometer separates the wavelengths of the

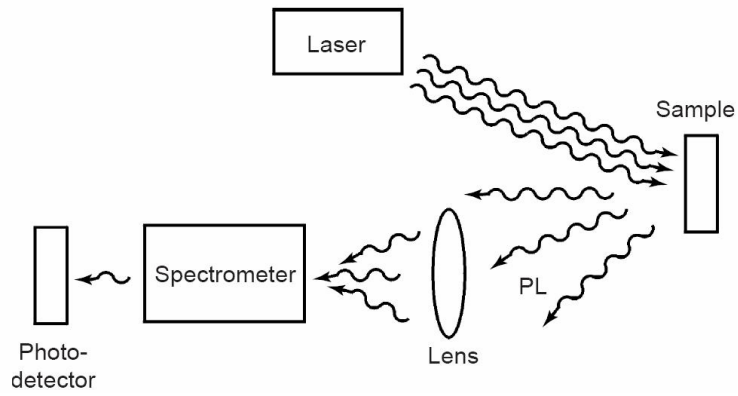

Figure 13: Schematic of PL setup

PL light to measure the spectral power distribution. Focusing optics are used to focus the light of the optical source onto a specific area of the sample under investigation, and then used to collect the PL and focus into the detector. Proper focusing of light is essential for high signal strength to distinguish the useable signal from the noise. The camera/detector collects the focused light and is used to record the desired data.

Defects, impurities, dangling bonds, surfaces and interfaces can contribute to the PL spectrum of a material. Surfaces and interfaces have high defect and impurity concentrations. Dangling bonds can also provide numerous mid-gap states that affect the PL spectrum of a material. Figure 14 shows some PL spectra of Si with different impurities contributing to the PL spectra. The PL setup used in this work is shown in Figure 15. Light is emitted from the Laser, and reflected 90° where it is focused onto the sample. The light from the sample is then collected by the optics and the monchromator, which feeds data to a computer. Quantum wells (QW) commonly used in LED design typically have large PL peaks associated with them. Furthermore, high quality multi-quantum well (MQW) structures with highly uniform well widths exhibit narrower PL peak widths than MQW structures with a larger range of well widths.

2.2.2.2 X-Ray Diffraction

X-Ray Diffreaction (XRD) is an analytical tool for the non-destructive characterization of compound structures. This technique is based on Braggs law, $n\lambda = 2dsin\theta$, where n is an

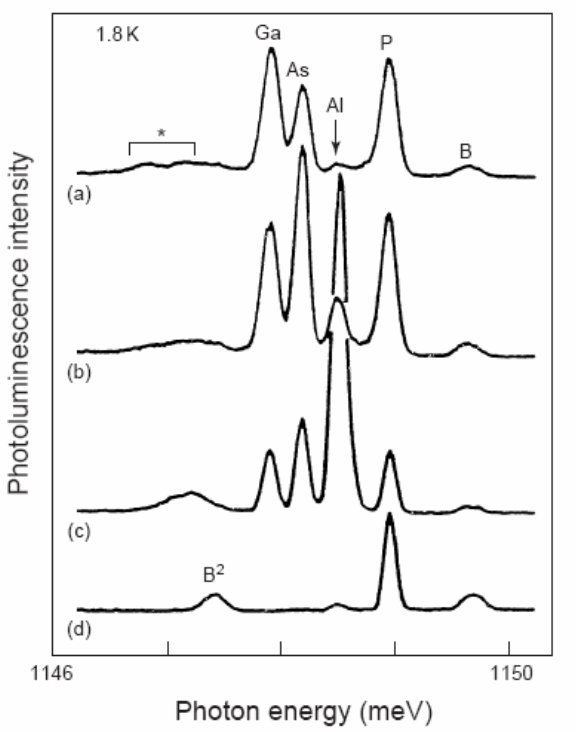

Figure 14: Sample PL spectra from Si

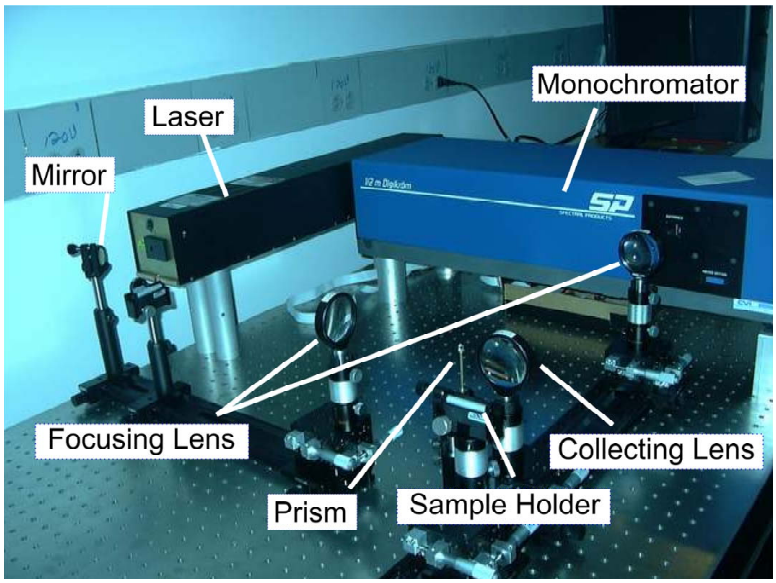

Figure 15: A picture of the PL setup used in this work

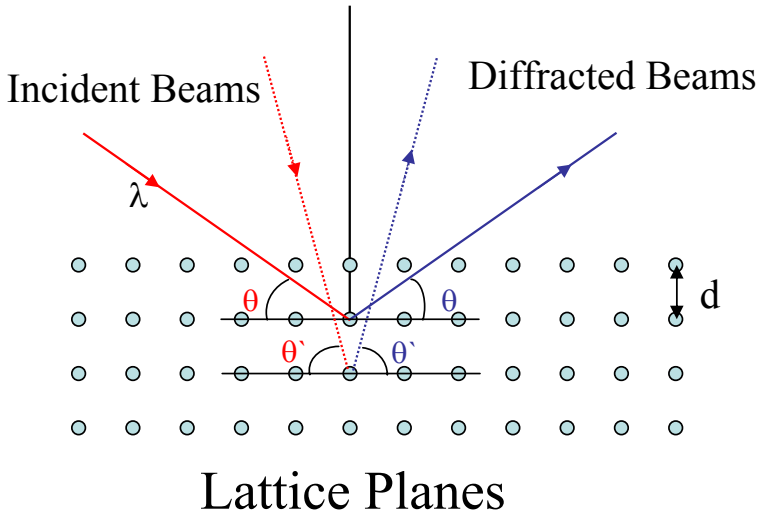

Figure 16: Schematic of X-Ray Diffraction

integer, λ is the wavelength of the x-ray source, d is the lattice spacing, and θ is the Bragg angle. X-rays are focused on to the sample where they are diffracted. The diffracted light is collected over a range of angles and the intensity is measured as shown in Figure 16. Every crystalline material has a unique lattice constant, corresponding to a unique Bragg angle. The reflected diffraction pattern from the epilayer determines a-spacing and c-spacing lattice constants of a material according to Braggs law. The linewidth of a rocking curve measurement, i.e. full width at half maximum (FWHM), determines the crystalline quality. Figure 17 is an example XRD measurement of AlN. A scan along the c-axis of GaN evaluates the c-spacing of GaN to be 5.18 Åand a relative scan along the a-axis provides the a-spacing, 3.18 Å. In addition, a rocking curve scan on an a-axis or c-axis estimates crystalline quality. MOCVD growth gives FWHM between 200 300 arcseconds from XRD peak on (0 0 0 2) reflection plane of GaN. Figure 18 is a picture of system used in this work. The X-Ray source, sample holder and detector are labeled.

2.2.2.3 Hall Effect

Hall effect measurements can be used to determine carrier density, mobility, and resistivity of a sample with one measurement. This makes Hall effect measurements a powerful tool in characterizing semiconductor materials. Resistivity, carrier density, and mobility each

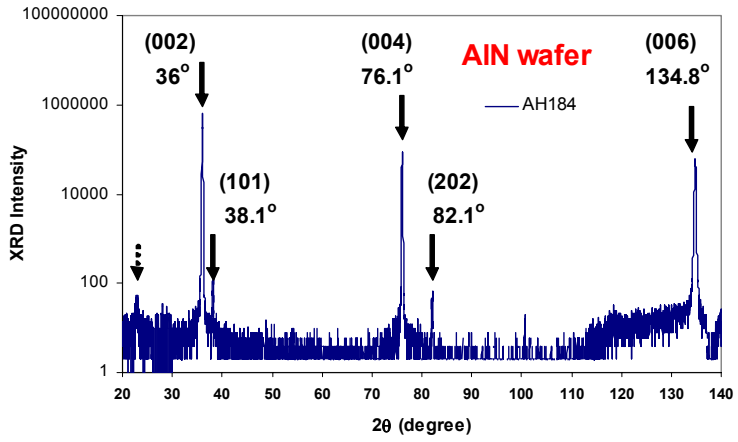

Figure 17: Example XRD measurement for AlN

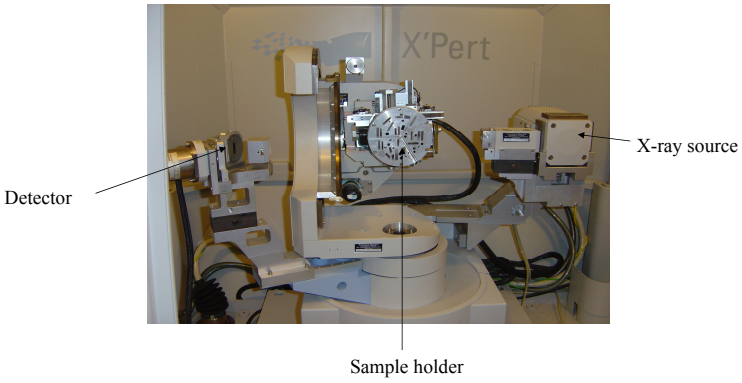

Figure 18: Picture of XRD system used in this work

effect the electrical performance of the material and thus the electronics devices made from that materials. Hall effect measurement is, however, a destructive technique, and proper procedures must be followed to insure accurate results. This section will discuss basic theory behind Hall effect measurements and the setup used in this work. It will also discuss some of the issues involved in measuring the materials grown in this work. The Hall effect is named after Edwin Hall, who in 1879 discovered that a magnetic field applied to a conductor perpendicular to the current flow direction produces an electric field perpendicular to the magnetic field and the current. This is shown in Figure 19 which is a schematic of a p-type semiconductor with current in the x-direction given by:

$$I = qApv_x = qwdpv_x \tag{3}$$

and a magnetic field B applied in the z-direction The voltage along the x-direction, V_ρ, is

$$V_\rho = \frac{\rho s I}{wd} \tag{4}$$

The resitivity can then be derived as

$$\rho = \frac{wd}{s}\frac{V_\rho}{I} \tag{5}$$

There also exists a force on the holes moving through a uniform magnetic field, of strength B, given by

$$\mathbf{F} = q\left(\mathcal{E} + \mathbf{v} \times \mathbf{B}\right) \tag{6}$$

The Hall coefficient is then defined as

$$R_H = \frac{dV_H}{BI} \tag{7}$$

From this the carrier concetration sample can be measured calculated as:

$$p = \frac{1}{qR_H}; n = -1\frac{1}{qR_H} \tag{8}$$

Typically, the measurement is performed by placing a known magnetic field and current and measuring the Hall voltage, V_H.

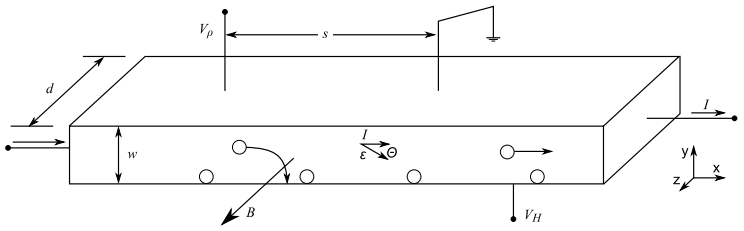

Figure 19: Schematic illustrating Hall effect in a p-type sample

2.2.2.4 I-V

The current-voltage characteristics of an LED are one the major performance measurements used to determine the quality of a device. Current-voltage measurements are usually performed by connecting a device to a voltage source and sweeping an input voltage over a certain range. At the same time, current through the device is measured as a function of the input voltage. When plotted, this data looks similar to. One of the major factors determined by I-V measurements is the series resistance of a device. Device performance is generally degraded by series resistance which depends on the the semiconductor resistivity, contact resistance, and possibly on the geometry of the device. The current in a diode is often written as a function of the diode voltage V_d as

$$I = I_0 \left(e^{\frac{qV_d}{nkT}} - 1 \right) \tag{9}$$

where I_0 is the saturation current and n is the ideality factor. The voltage across the space-charge region excluding any voltage drops across the p and n quasi-neutral regions is the diode voltage V_d. If Figure 20 is taken as the equivalent circuit of a diode then

$$V = V_d + Ir_s \tag{10}$$

and the current through the diode can be written as

$$I = I_0 \left(e^{\frac{q(V - Ir_s)}{nkT}} - 1 \right) \tag{11}$$

At high currents the series resistance of the diode has greater affect and can be seen as sloping over of the I-V curve. At high currents the series resistance can be determined from

$$r_s = \frac{\Delta V}{I} \tag{12}$$

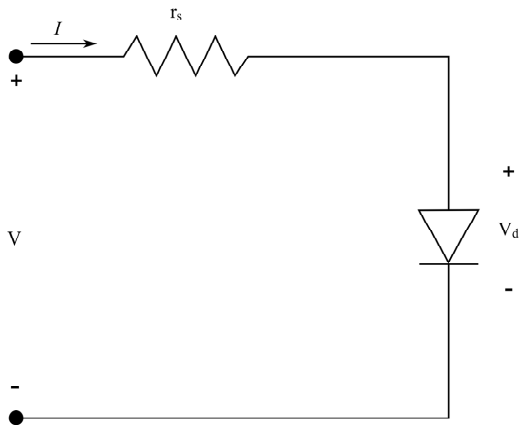

Figure 20: Equivalent circuit of a diode

Another important factor that is determined with I-V measurements is the forward voltage of a diode at a certain operating current. This number is often quoted as a performance characteristic when describing a device. In the high brightness LED industry the forward voltage at 20 mA is often quoted. 20 mA is a relatively low operating current, and as such manufacturers will often only use this number for comparison purposes amongst devices. They will often provide a forward voltage at the desired operating (typically >300 mA) current in order for customers to design proper drive circuitry.

2.2.2.5 EL

Electroluminescence measurements are performed by injecting current into the LED and collecting the light output from the device. Electroluminescence is the normal operation for an LED. Typically devices are fabricated with metal contacts on the n and p regions. The device is then connected to a power source, and situated so that the light output can be collected using optics and directed towards a spectrometer and/or light power meter, similar to PL spectroscopy. The spectrum and the overall power output are important in EL measurements. Spectral only measurements are much simpler to perform since it is assumed that the light output is uniform over the device and only light from one point needs to be collected. Since EL is the operating process for LED, EL spectroscopy measurements provide a direct correlation to how the device will operate. However, if the total luminous

flux is desired then, all the light from the device must be collected or a tightly calibrated setup must be used. An integrating sphere is a common tool for collecting the total output from a device. In this arrangement the device is inserted into one side of the sphere. The interior of the sphere is coated in a highly reflective materially which reflects the light onto a point in the sphere. The system is calibrated to so that the light measured from the sphere corresponds to a total light output of the device. Another arrangement involves collecting the light at specific location in relation to the LED, and calibrating that measurement with a known light output. This arrangement is less accurate than use of an integrating sphere because of error introduced in placing the collecting optics of the system as well as the device placement. Additionally it is difficult to account for variations in the radial distribution of the light emitted from the LED. However contacting of the device is simplified in this setup as it can be placed on a probe station. Efficiency of the device can be determined from the EL total luminous flux measurements. The external quantum efficiency of a LED is determined by measuring the light output power and dividing it by the input power. This metric is often quoted in lumens per watt or watts per watt, and is one of the fundamental metrics used in evaluating LED performance.

2.2.2.6 L-I

Luminescence-current measurements are an extension of EL measurements. EL total luminous flux and spectrum are collected while sweeping over a specified current range. these measurements provide data on how a device performs with changing drive current, and can provide insight into issues involved with device performance.

2.2.2.7 AFM

Scanning Probe Microscopy (SPM), which includes Scanning Tunneling Microscopy (STM) and Atomic Force Microscopy (AFM), are experimental techniques used to image both organic and inorganic surfaces with (near) atomic resolution. It was in the 1980's that IBM scientists, Binnig and Rohrer developed the STM. The STM measures the tunneling current between a sharp conducting tip and a conducting sample. The STM can image the samples topography and can measure its electrical properties by tunneling current between

a sharp conducting tip and a conducting sample. The STM can also measure the electrical properties of the sample by the tunneling current between them. However, it cannot be used for non-conducting material[31]. To provide a solution to this problem, in 1986, Gerd Binnig and Christoph Gerber used a cantilever made by gluing a shard of diamond onto a strip of gold foil to examine insulating surfaces. A small hook at the end of the cantilever was pressed against the surface while the sample was scanned beneath the tip. The force between tip and sample was measured by tracking the deflection of the cantilever. The force microscope emerged in this way. Nowadays, the tip-cantilever assembly is usually fabricated from Si or Si_3N_4.

Physical principle and instrumentation: In the AFM, a cantilever with a small tip at the end can be mounted on a piezoelectric crystal that can move in the X, Y, and Z directions. If the tip is scanned over a surface, the probe moves up and down over its topography and the displacement caused by the features on the surface can be measured to create an image. The AFM measures the Van der Waals force between the tip and the surface; this may be either the short-range repulsive force (in contact-mode) or the longer-range attractive force (in non-contact mode). By manufacturing extremely small tips, it is possible to image atoms and molecules on a surface. The tip is scanned over a surface with a feedback mechanisms that enable the piezo-electric scanners to maintain the tip at a constant force (to obtain height information), or height (to obtain force information) above the sample surface. The AFM uses an optical detection system in which the tip is attached to the underside of a reflective cantilever. A laser diode is focused onto the back of a reflective cantilever. As the tip scans the surface of the sample, moving up and down with the contour of the surface, the laser beam is deflected off the attached cantilever into a dual element photodiode. The photodetector measures the difference in light intensities between the upper and lower photodetectors, and then converts it to a voltage. Feedback from the photodiode difference signal, through software control from the computer, enables the tip to maintain either a constant force or constant height above the sample. In the constant force mode the piezo-electric transducer monitors real time height deviation. The main

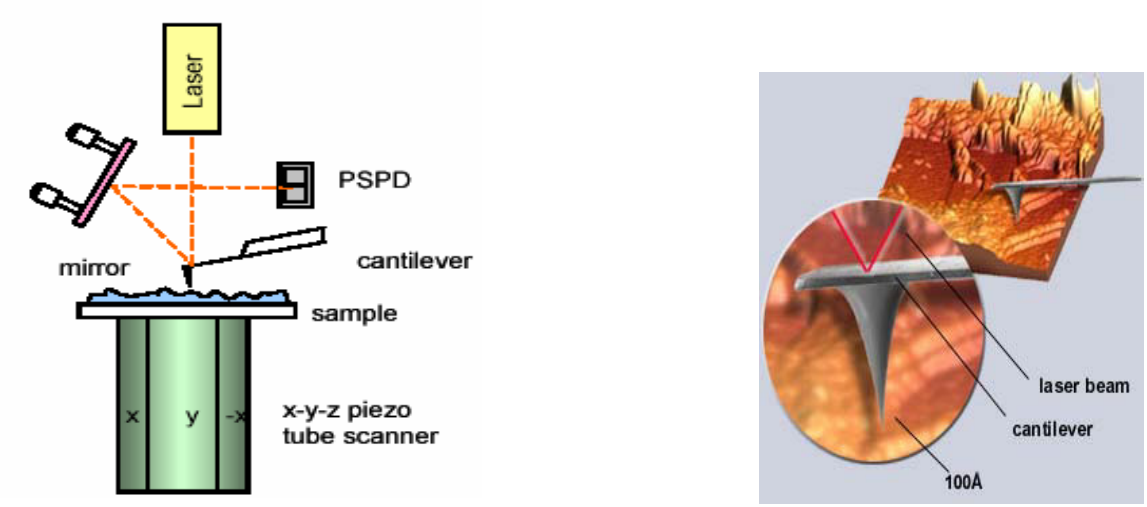

(a) (b)

Figure 21: Diagram of (a) conventional AFM and (b) cantilever

function of the instruments is to quantitatively measure surface roughness and provide an image of surface topography. Three dimensional topographical maps of the surface can be constructed by plotting the local sample height versus horizontal probe tip position. There are three scanning modes associated with the AFM, namely, contact mode, tapping mode, and non-contact mode. Contact mode is the scanning mode in which the tip is in contact with the surface and the image is obtained by the repulsive forces between the tip and the sample. In tapping mode, the image is obtained by the tip, which just taps the surface for small periods of time. In non-contact mode, the tip oscillates above the surface and the image is obtained by the attractive forces between the tip and the sample. For QD analysis, mostly tapping mode or contact mode tip is used. The contact mode tips used for scanning QDs usually have a higher spring constant so that it can scan over the rough QD sample without breaking. In order to obtain good AFM results, a vibration isolation platform is needed to damp out any external vibrations that may affect the measurements.

2.2.2.8 CIE, Correlated Color, CCT, and CRI

The International Commission on Illumination or Commission Internationale de l'Eclairage (CIE) has developed a chromaticity diagram, Figure 22, on which any color of light can be plotted. The edges represent single wavelength or saturated colors and any point in

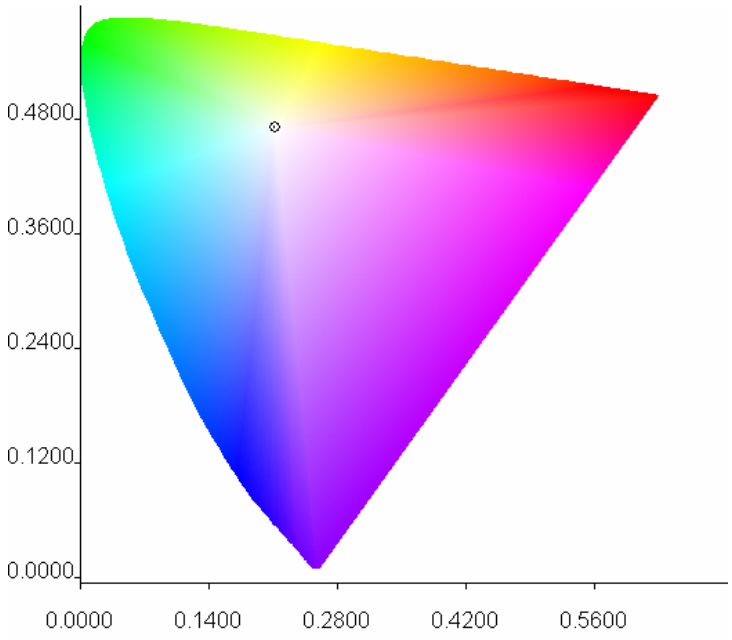

Figure 22: 1976 CIE Diagram

the middle corresponds to some spectral broadening or mixing of those wavelengths. The Planckian Locus, a set of points corresponding to a black body's radiation (Figure 23) at different temperatures can then be mapped onto this diagram. By creating light with coordinates on the Planckian Locus, the light is said to have a certain color temperature, meaning that is looks the same to the eye as a black body heated t o that temperature. Chromatic adjustment by the human eye causes colors that are close to look the same when they are not next to each other. By moving slightly off the curve in any direction the source can be characterized by a correlated color temperature, corresponding to the isotemperature lines in Figure 22 drawn through the Planckian at certain color temperatures. It is important to note that an increase in temperature essentially corresponds to an increase in the amount of blue light contained in the spectrum as indicated by the arrow in Figure 23. In fact, for a 6000K source the intensity at 470nm (blue), near the maximum of the circadian response, is about 250 times greater than that of a 3000K source. Daylight moves along the Planckian through the day corresponding to shifting color temperature as shown in Figure 24.

Another important lighting metric is the Color Rendering Index (CRI). A sources ability to render colors as compared to a standard source is measured on this index which usually

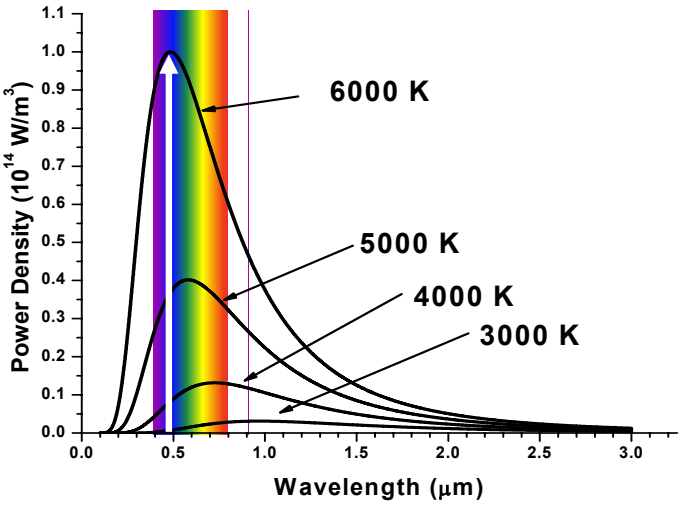

Figure 23: Black Body Radiation Curves at Various Temperatures

Figure 24: Comparison of CCT for various sources

ranges from 1 to 100. This is essentially how similar different color samples appear when viewed under a test source as compared to the standard source. A CRI of 100 would mean that all the samples looked the same under the test source as the standard source8. Manufacturers commonly use this index to characterize the quality of their sources; it does not however correlate with how "good" the colors look. As a standard metric it is important to take into consideration when developing a new source.

2.2.3 Fabrication

Fabrication of LEDs currently requires the use of tools commonly found in the microelectronics industry. LED chip fabrication is the process of isolating chip size areas of a wafer with the appropriate semiconductor material and contacting the p and n sides of each chip with metal. These chips can then be cut from the wafer and packaged as desired. In this work, photolithography was used to create a pattern on the the wafer for each fabrication step. Reactive ion etching (RIE) or inductively coupled plasma (ICP, a form of RIE) was used to remove material around each chip, thus isolating them from surrounding chips and exposing n-type material for contacting. Electron beam (E-beam) evaporation of metal was used to deposit contacts on to each device. Each of these techniques and the principles behind their use are discussed further in this section. Then, the specific process used for devices in this work is described in detail.

2.2.3.1 Rapid Thermal Annealing

Rapid thermal annealing (RTA) is a heating process used commonly in semiconductors to quickly heat a sample for a designated period of time and rapidly cool the sample afterward. The RTA system used in this work contained an metal filament that can be heated very rapidly by passing a current through it much like an incandescent bulb. A large part of the energy emitted from the filament is in the form of infrared radiation, which is used to heat the sample. Once the current to the filament is turned off the sample begins cooling down. A typical RTA system can reach +800°C in 30 seconds or less, decreasing the effects of heat during the temperature ramp on the sample. The system is controlled to maintain a designated temperature by increasing or decreasing the current through the filament based

on the current temperature reading at the sample. Another feature of most RTA systems is the ability to introduce a gas into the chamber at the time of annealing. In the case of this work N_2 and air ambients were used for annealing steps.

2.2.3.2 Photolithography

Photolithography, also known as optical lithography, is a process used to transfer a pattern from a photomask to a substrate. Photolithography may involve the following:

- substrate preparation
- photoresist application
- soft-baking
- exposure
- crosslinking-baking
- developing
- hard-baking

Substrate preparation is important to avoid contamination and in this work involves cleaning with solvents. Cleaning prepares the surface for photoresist application, which is typically done by spinning the photoresist onto the sample. An appropriate amount of photoresist into cover the entire sample is placed in the center of the sample. A typical spinner setup has a vacuum chuck to hold the sample on a spindle, which rotates at several thousand rpm spreading the photoresist over the sample uniformly by centrifugal force. The thickness of the photoresist layer is partly determined by the rate at which the spinner spins. Soft-baking occurs at a relatively low temperature to slightly harden the photoresist so that it can be handled and placed into the exposure tool, without changing the chemical properties of the photoresist. Exposure is typically performed with a mask aligner whose function is to bring the sample and the mask closely together and align them if necessary with the mask between the sample and the exposure light source. The mask aligner then exposes

the sample to a specific wavelength of ultraviolet light that changes the chemical property of the photoresist. This only occurs under areas of the mask that have no metal patterning, resulting in a pattern transfer to the photoresist layer. The photoresist in this work then requires a crossover bake that once again changes the chemical properties of the photoresist, but acts differently on the exposed and unexposed areas of the photoresist. The sample is then placed in a developing solution that removes one of the exposed or unexposed areas of photoresist, but not both. Whether the unexposed or exposed areas is removed is a function of the photoresist. After developing, a pattern that is either the positive or negative of the photomask is left on the wafer in the form of photoresist. The photoresist is then typically baked at a high temperature to make it resistant to further fabrication steps, such as etching where it is desired to remove only substrate material not covered by photoresist. A metal pattern can also be transferred to the substrate with a photoresist pattern and etching or lift-off techniques. Finally, the photoresist is removed using a specialized stripper solution, or acetone. This process can then be repeated to transfer another pattern over the previous pattern[10]. The specifics of the photolithography for this work are discussed below in Section 2.2.3.5.

2.2.3.3 Reactive Ion Etching

Reactive ion etching (RIE) is an anisotropic dry etching process in which a plasma of reactive ions is used to etch a material. For example a GaN sample is placed in a chlorine ambient on a powered electrode used to strike a chlorine plasma as shown in Figure 25. The plasma causes ion bombardment of the sample surface where chemical and kinetic forces etch away the surface. Anisotropy is prevalent because ion bombardment is very small on the vertical walls of the sample and only the horizontal surfaces see the etching.

2.2.3.4 Electron Beam Evaporation

Electron beam evaporation is a form of physical deposition in which a material (the charge) is evaporated by a focused electron beam and deposited somewhere else. The electron beam provides heat to the charge until it evaporates at a rate desired by the user. Metals are evaporated by this method and deposited as the contacts for LEDs. The metal charge sits

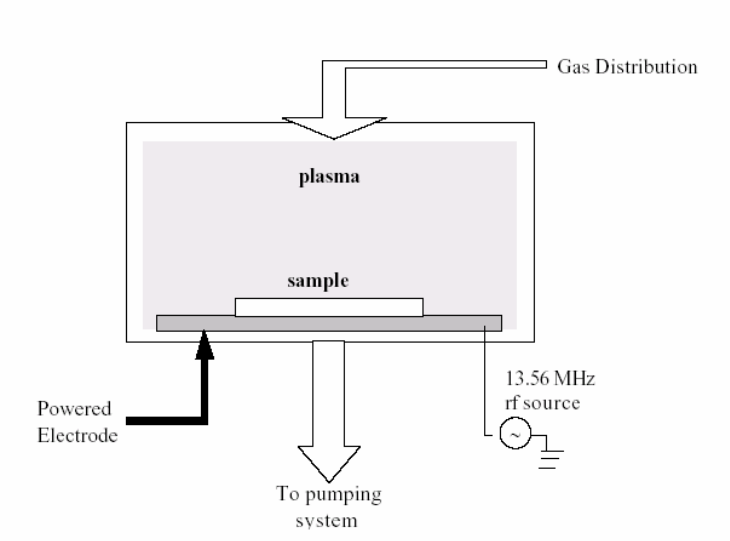

Figure 25: Schematic of a typical RIE system

in a crucible made of graphite at the bottom of a deposition chamber that is pumped to $\sim 10^{-6}$ torr. The sample for deposition is placed deposition side down or facing the charge and crucible as shown in Figure 26. An electron beam is focused onto the charge and heats it. As atoms evaporate from the charge they travel upward to the sample and deposit forming a film. The rate of deposition is dependent on the material and the power of the electron beam as well as the pressure of the reactor. In general the evaporated material is assumed to have uniform flux over a semisphere above the charge. If the deposition sample is placed suitably far away, a film of relatively uniform thickness can be expected.

This work included the evaporation of:

- Nickel (Ni)
- Gold (Au)
- Titanium (Ti)
- Aluminum (Al)

2.2.3.5 Fabrication Process Specific to This Work

This section will step through the fabrication process used in this work for LEDs and other diode devices. Some discussion of the reasons and issues for each step will be included. The

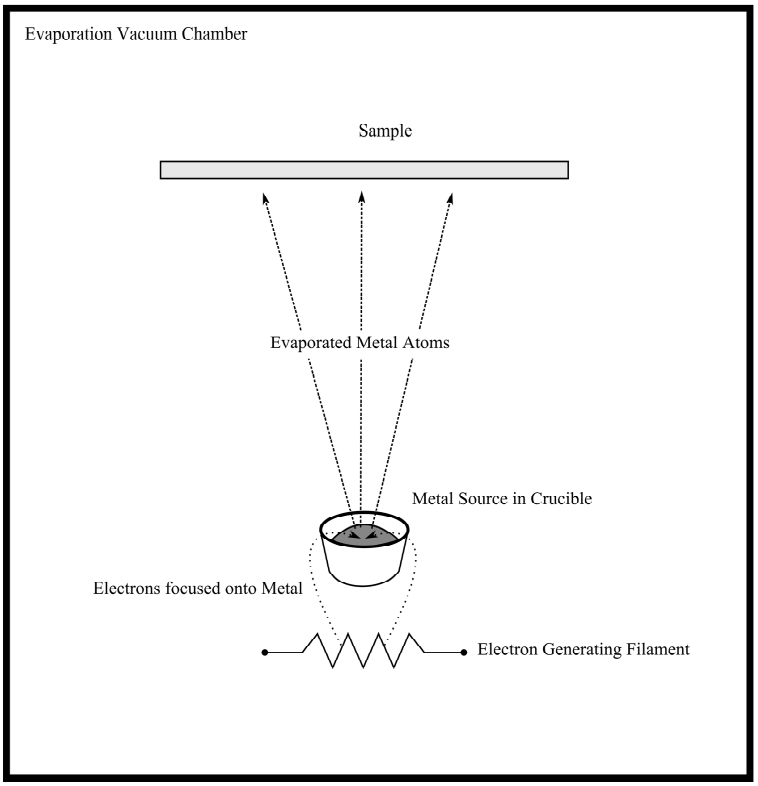

Figure 26: Schematic of an E-beam evaporation setup

major processes involved in the fabrication of LEDs are discussed Sections 2.2.3.1- 2.2.3.4.

Solvent Cleaning Routine A LED wafer is removed from the MOCVD growth chamber, and is either fabricated whole or cut into pieces for device fabrication. The sample is then cleaned using a solvent cleaning routine . The sample is sprayed with Trichloroethane (TCE) first to remove any organic matter that may have deposited on the sample. Acetone is then used to remove the TCE and any residual contaminants. Methanol is then sprayed on the sample to remove the Acetone and other residual contaminants. The sample is then thoroughly washed with deionized water to remove any methanol and other contaminants. Finally, the sample is thoroughly dried with a nitrogen gun.

Anneal - pGaN Activation The sample is annealed in the RTA system at 800°C for 4 minutes under N_2 ambient. This steps serves to drive hydrogen out of the pGaN layer on top of the device thereby activating the Mg dopants as acceptors in the lattice.

Metal Deposition - Semitransparent Contact A semitransparent metal layer is deposited next. 5 nm of Ni followed by 5 nm of Au are deposited directly on the annealed sample. This metal layer serves as a current spreading layer that allows light to pass. In the next step, it is made to help form an ohmic contact to the pGaN surface.

Anneal - Current Spreading Contact Annealing the previous Ni/Au layer in an oxygen ambient causes oxygen to diffuse into the metal layer and form NiO at the metal semiconductor interface which aids in making an ohmic contact to the pGaN surface. The sample is annealed in the RTA at 500°C for 2 minutes in standard atmosphere which contains oxygen.

Pattern transfer - Mesa Photolithography is used next to transfer a mesa pattern to the sample that will define the semitransparent Ni/Au pattern as well. Photoresist is spun on the sample at 2500 rpm for 30 seconds, followed by a second photoresist layer at the same parameters. The photoresist layer is then soft-baked at 100°C for 1.5

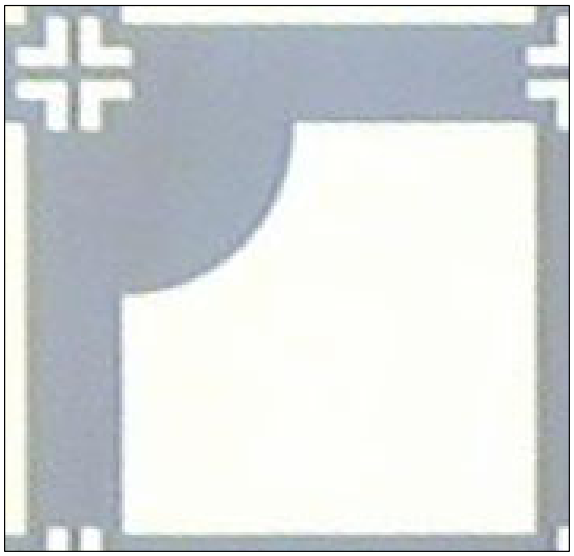

Figure 27: Picture of photomask for mesa pattern

minutes and then exposed with the mesa pattern mask shown in Figure 27 for a total of 60 $\frac{mJ}{cm^2}$ of photonic energy (for example, 10 seconds of light with intensity of 6 $\frac{mW}{cm^2}$). A crosslinking-bake is then performed at 115°C for 2.5 minutes. A flood exposure is then performed without a mask for a total of >180 $\frac{mJ}{cm^2}$. Finally, the photoresist is developed in a solution of 5:1 H2O:AZ 400K for 1 minute.

Metal Etch - Semitransparent The sample is then submerged in potassium iodide which removes any metal not covered with photoresist. Potassium iodide is typically used as a gold etchant but is used here to etch both the Ni and Au.

Hard-bake A hard-bake in a laboratory oven at 120°C for 30 minutes is required before the sample can be dry etched. The photoresist layer must be cured in the oven to prevent its etching in the dry etch process. This will insure that the material underneath the photoresist remains intact.

Dry Etch - Mesa Reactive ion etching of the sample is performed to define the mesa structure of the device and expose the n-type GaN layer for contacting. A typical etch depth for an LED device in this work is 1.2 μm.

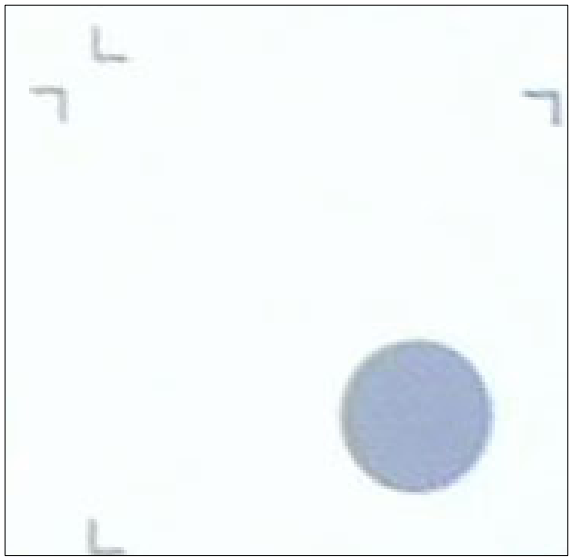

Figure 28: Picture of photomask for p bonding pad

Photoresist Stripping Reactive ion etching causes some damage to the photoresist increasing the difficulty of totally removing the photoresist layer. However, an ultrasonic bath of acetone for 15 minutes removes all residue of the photoresist. Methanol is then used to remove and acetone residue, and de-ionized water is used to remove any methanol. Drying with a nitrogen gun is the final setup before the next patterning step is performed.

Pattern Transfer - pGaN Bonding Pad The pattern transfer for the pGaN bonding pad is very similar to the mesa pattern transfer, except only on layer of photoresist is deposited, and the soft-baking and crosslinking-baking times are reduced to 1 min and 2 minutes, respectively. Figure 28 shows the mask pattern for the pGaN bonding pad. The mask and sample patterns must be aligned so that the pGaN bonding pad is at the proper place relative to the mesa for each segment of the pattern.

Metal Deposition - pGaN Bonding Pad Electron beam evaporation of 50 nm of Ni followed by 250 nm of Au creates the metal layer for the pGaN bonding pad. The thickness of the Au layer determines how well a wire bonder will be able to bond a lead wire. If the Au is too thin it will peel off with the wire bonding process.

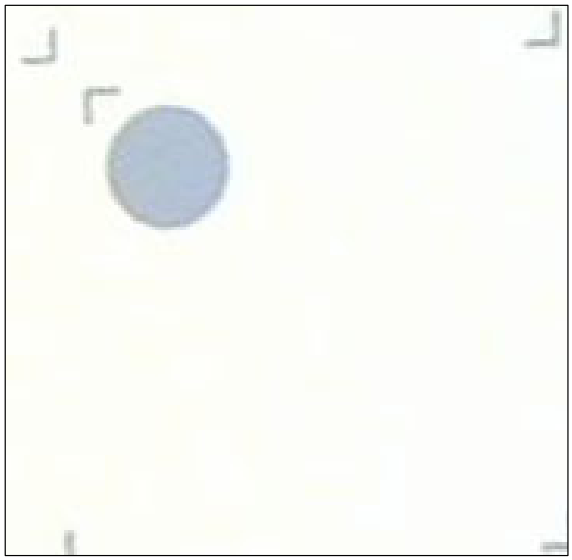

Figure 29: Picture of photomask for n bonding pad

Metal liftoff - pGaN Bonding Pad Metal deposition covers the entire sample, including the areas covered by photoresist. An ultrasonic acetone bath strips away the underlying photoresist and any metal that is covering it, leaving metal only on the areas that were not covered by photoresist. This process is called metal lift-off because the metal is lifted away with the underlying photoresist, leaving only the desired pattern.

Pattern Transfer - nGaN Bonding Pad The pattern transfer for the nGaN bonding pad is exactly the same as the pGaN bonding pad, except that the nGaN bonding pad mask is used instead of the pGaN mask. The nGaN bonding pad mask is shown in Figure 29.

Metal Deposition - nGaN Bonding Pad Electron beam evaporation is used to deposit 10 nm Ti, 50 nm Al, 10 nm Ti and 250 nm Au in that order. The gold capping layer must be thick enough to allow wire bonding.

Metal Liftoff - nGaN Bonding Pad The metal lift-off for the nGaN bonding pad is exactly the same as for the pGaN bonding pad.

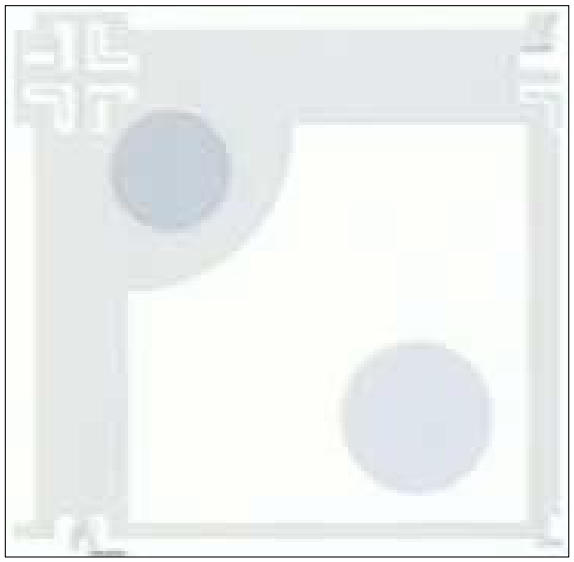

Figure 30: Picture of all photomasks overlayed

Figure 30 is a photograph of the each of the photomasks overlayed to show the final pattern. Figure 31 shows the electroluminescence from an LED grown and fabricated using the process described above.

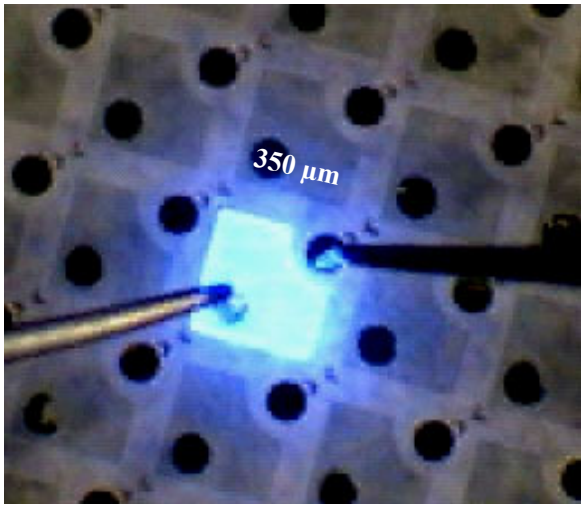

Figure 31: Electroluminescence from a MQW III-nitride LED

CHAPTER III

MODELING & DEVICE DESIGN

3.1 Optical Modeling & Device Design

3.1.1 Optical Modeling Approaches for LEDs

3.1.1.1 Introduction

In this section, a guided wave approach is first introduced, and a LED is modeled as a multi-layer waveguide structure. Light emitted from the LED is classified into guided modes and leakage modes. Also, the back reflector at the bottom of the LED dies effectively doubles the LED die thickness to increase the light extraction efficiency. Moreover, replacement of a back reflector with a diffractive reflection grating further improves light extraction efficiency.

3.1.1.2 Guided Wave Approach for LED Modeling

The LED die can be modeled as two types of optical waveguides as shown in Figure 32: the first waveguide consists of the single or multiple quantum well (MQW) active region and n-layer and p-layer of the LED. Optical waves are generated in this waveguide structure, which we call an active waveguide. The second waveguide structure consists of a sapphire or SiC substrate and medium surrounding its sidewalls, defined as a passive waveguide; and its main function is to support optical waves generated in the active waveguide. The refractive index of the substrate is lower than that of active waveguides.

In general, the active waveguide consists of several thin film layers, several microns in thickness and several hundreds of microns in the lateral dimension. It can be treated as a slab waveguide and acts as an optical photon generator. On the other hand, the thickness of the passive waveguide is usually several hundreds of microns, with the same lateral dimension as the active region. Based on the above analysis, it is believed that the passive waveguide will make the main contribution to light extraction from the LED die. However, the active waveguide will also play an important role in light generation and extraction,

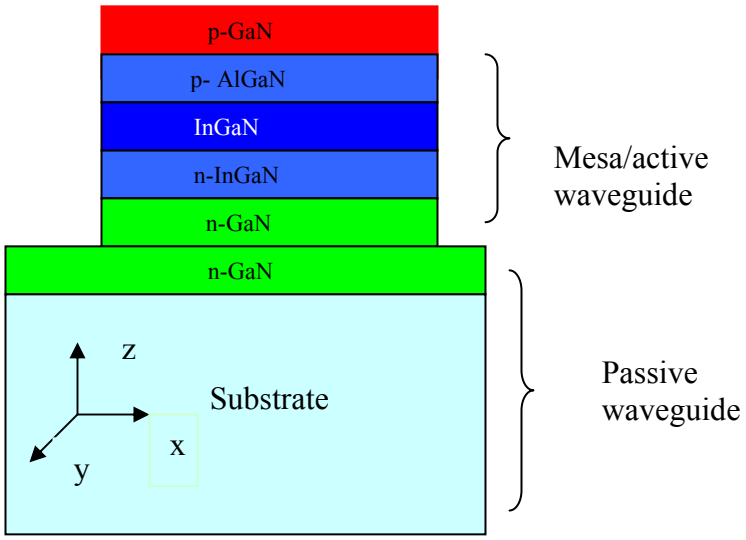

Figure 32: Waveguide Structure of a GaN LED

which is a key factor in improving the brightness of LEDs.

Photons generated in the active region from electron-hole pair recombination can be modeled as multi-mode optical waves with a certain mode distribution. Among these multi-mode optical waves, a longitudinal wave represents those modes propagating along the z direction, i.e, the direction of layer variation of a LED structure, and the transverse mode wave propagates along the x and y directions, lateral directions.

In the nitride heterostructure of LEDs, the guiding layer of the active region consists of the InGaN/GaN MQW. The p-GaN, p-AlGaN layer, n-GaN layer, and n-InGaN layer surrounding the active region form the cladding region. This waveguide does absorb blue light because of the high absorption from the InGaN layer.

Since the x-y dimension, the lateral direction, is fairly large relative to the z dimension, the transverse mode of optical waves can be solved using the slab wave guide theory. Because the absorption of InGaN is strong at the blue wavelength region, the transverse modes, which are defined as propagating along the (x y) plane, hardly reach outside the waveguide. As a result, the transverse optical wave almost makes no contribution to the light coupling and extractions.

The mesa region above the substrate in a LED die is the region of the active waveguide,

which is responsible for photon generation and coupling into its surroundings. Alteration of the lateral shape of the mesa results in almost no change to light emission because this part is modeled as a slab waveguide. The passivation layer coated on the mesa will influence the structure of the active waveguide. Since this passivation layer is transparent to blue light, its restriction on the light extraction efficiency comes from the interface TIR, which forces photons to undergo multiple passes through the absorption region of the active region of a LED and decreases the extraction efficiency of the light.

Both the longitudinal modes, which are mainly leakage modes, and transverse modes of photon emissions in the active waveguide region contribute to light coupling outside the LED die. Longitudinal modes are first considered. The forward propagation of longitudinal modes is coupled out of the active waveguides through a p-pad of an electrode on the top of LEDs. The backward parts of those longitudinal modes go through the sapphire substrate, the passive waveguide, and are then sustained as either a guided wave or leakage mode wave in the passive waveguide. The sapphire is transparent to blue light, and the material property of the medium surrounding the substrate changes the passive guide structures and light extraction efficiency. Most of the longitudinal modes are leakage modes, and their extraction efficiency can be improved by applying a micro-resonant cavity[57]. Because of the refractive index difference for different layers along the z-direction (longitudinal direction), the coupling efficiency of light from the active waveguide to the passive waveguide is restricted by the refractive index difference of n-GaN (n=2.42 @ 460 nm) and the sapphire substrate (n=1.78 @ 460 nm). The critical angle is calculated as c= 47.5 degrees. Beyond this angle, the light from the active waveguide is trapped inside the active guides, which undergoes the process of re-absorption; and parts of the trapped light can escape the active waveguide in the forward direction through the p-pad. Some of the light transmitted into the passive wave-guide becomes guided modes, and the rest are leakage modes. If angles are all defined in the active region, the angles below which the guided modes occur is

$$sin\,(\Theta_s) = \frac{\sqrt{(N_{sub}^2 - N_{sur}^2)}}{N_p} \tag{13}$$

where N_{sub} and N_{sur} denote the refractive index of the sapphire substrate and its surrounding medium, respectively. N_p is the refractive index of the n-layer. If the air is used as the surrounding medium, then $s = 37.5$ degrees. In other words, the light inside the n-layer above the substrate with different incident angles between 0 to 37.5 degrees becomes guided modes; that from 37.5 to 47.5 degrees becomes leakage modes in the passive waveguide, respectively. Accordingly, the light with incident angle beyond 47.5 degrees is totally internally reflected back to the active waveguide. Because the refractive index of the n-layer and substrate both are fixed, the coupling efficiency from the active waveguide to the passive waveguide is pretty much unchangeable, i.e., only a light cone defined by the angle of 47.5 degrees can be coupled into the passive waveguide layer.

Backward Light Extraction through the Passive Waveguide: Most of the light coupled into the passive waveguide becomes guided waves, with a half cone angle of 37.5 degrees (assuming air is the cladding layer surrounding to the passive waveguide); and light within a half cone angle from 37.5 to 47.5 degrees belongs to the leakage modes. In other words, about 70% of the light coupled from the active waveguide is guided wave, and the rest of light is leakage wave. The ratio of guided wave to leakage wave can be changed by either alternating the refractive index of the surrounding medium or changing shape of the die, for example, from a standard square die to a non-square die.

Assuming the material of the passive waveguide is transparent to blue light, most of the light coupled into the passive waveguide can be extracted by optimizing geometry and refractive index matching of the substrate and its surrounding medium, for example, the spherical or dome shaped encapsulation of the LED. This is especially true for flip-chip LED packaging. In standard LED packaging, the die-attached epoxy at the bottom of the substrate is highly absorptive.

First, we study light extraction from guided modes in backward propagation light. In the case of no reflector at the bottom of the substrate, the guided mode wave in the passive waveguide propagates in the waveguide until reaching the bottom of the substrate, and light is absorbed by the layer of a die-attached epoxy. The absorption decreases the light

extraction efficiency.

By putting a back reflector at the bottom of the substrate, the guided mode optical wave is reflected back to avoid strong absorption at the bottom of the substrate, and light extraction efficiency is increased. However, the reflector folds back the light path and forces light to re-enter the active waveguide region and is absorbed again by the active layer. The reflected light at the reflector needs to be further diffracted by a grating, and the diffracted light can escape from the passive waveguide before it enters the active region to undergo re-absorption. Also, more energy of the light can be shifted into leakage modes from guided modes by changing the structure of the passive waveguide structure, for example, the refractive index of the surrounding medium and the shape of the waveguide structure. For leakage modes in backward propagation light, the substrate and the die-attached epoxy play major roles. The highly absorptive die-attached epoxy layer sitting at the bottom of a substrate has little influence on the leakage modes because the light of leakage modes hardly strikes the bottom of the substrate. To couple the leakage mode as much as possible, the interface between the substrate and its surrounding medium needs to be designed better, for example, tapered sidewalls, or textured surfaces of LEDs can improve light extractions of leakage modes. LEDs with regular geometry can redirect some leakage modes into the active waveguide.

Forward Light Extraction from the Active Waveguide Layer: Because of the reflection at the interface between the n-layer and the sapphire substrate, the backward light gets reflected from this interface and joins the forward emitted light from the active region of a LED. This combined forward light strikes on the semi-transparent contact, the p-pad, where the total internal reflection (TIR) occurs (assuming the refractive index of the transparent contact is about 1.5). About 38% of the forward light with a half angle of 38 degrees, determined by the TIR, can be coupled out through the semi-transparent contact. The TIR occurs again at the interface between transparent contact and a passivation layer on the top of the LED. By applying the waveguide theory, functions of the active waveguide and passive wave guide can be seen clearly. The different contributions to light extraction

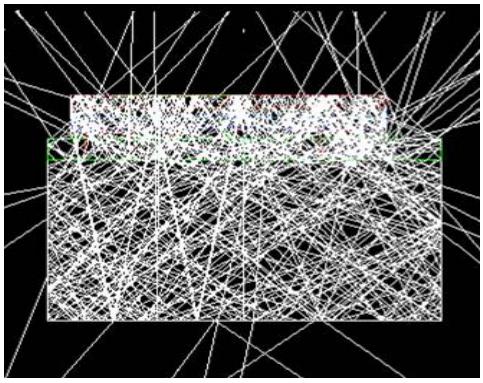

Figure 33: Geometrical ray tracing of a LED die.

from guided modes and leakage modes can be analyzed. The passivation layer and medium surrounding the die are analyzed through the total internal reflection. It is shown that the reflector only influences guided modes and has little effect on leakage modes in the passive waveguide. The coupling efficiency of the leakage mode is mainly determined by the interface between a substrate and its cladding layer, i.e., its surrounding medium.

3.1.1.3 Improved light extraction using a back reflector and thick substrates

A typical bare LED die consists of a p-GaN layer, n-GaN layer, and active region with AlGaN and InGaN. InGaN strongly absorbs in blue region, and both the p-GaN and n-GaN layers also absorb blue light with relatively small absorption coefficients compared to InGaN. The semitransparent contact Ni/Au on the top of the p-GaN layer of the LED die absorbs about 10% light. A Ti/Al contact was deposited on the n-GaN layer after the etch process. The whole device structure is grown on the sapphire substrate. All of these above layers form the absorption region of blue light. The problem is that light generated at the active region has to experience multiple passes and reflections inside these absorption regions before coming out of the LED die, as shown in Figure 33 and Figure 34. At the bottom of the LED substrate, there is a highly absorptive layer of the die-attached epoxy, which absorbs some light propagating toward the LED bottom, especially those guided modes. One way to increase light extraction efficiency is to use a thick substrate. With the thick substrate, more light is able to escape the LED chips through its sidewalls before reaching

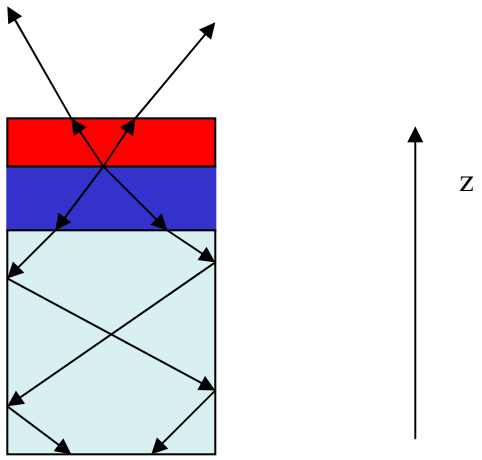

Figure 34: Forward and backward propagation of light in a LED

the bottom of the substrate. On the other hand, the light extraction efficiency of the LED can be increased by coating a metal mirror, such as an aluminum reflector at the bottom of the sapphire substrate, to avoid light absorption by the die-attached epoxy. Another function of the back mirror is that it folds the light path and equivalently doubles the actual thickness of the LED die experienced by backward emissions from the LED active region, which also increases light extraction efficiency. As a result, the light extraction efficiency is increased more than 20% by applying this back reflector. The substrate thickness and mirror reflectivity can be optimized using our model.

3.2 Optical Modeling for a Dual Wavelength LED

3.2.1 Dual wavelength LED Device Structure

Current white LEDs schemes are either based on a short wavelength LED pumping a longer wavelength phosphor (phosphor converted LED) or discrete red, green and blue chips coupled with light mixing technology (RGB LED). Each of these schemes has particular advantages; however, there are also significant disadvantages associated with each as well. The blue LED / YAG:Ce scheme is the most common type of white LED and is the cheapest of the white LED solutions. However, the color rendering quality of the light from a LED/YAG device is typically low due to deficiencies in the power spectrum especially for the red wavelengths. Various phosphors can be employed in similar white LED schemes to

produce more red light; however, the efficiency of the device is decreased due to the increase in stokes shift associated with pumping a longer wavelength phosphor. Additionally, there is no functionality for dynamic control of the power spectrum for a phosphor converted (PC) LED such as with a RBG LED. The power spectrum of an RGB LED can be controlled by varying the relative intensities of the red, green or blue sources, which allows for two things: dynamic sources and color correction over the lifetime of the device. On the other hand, the spectrum from a RGB LED is sharply peaked and may not render colors well if a valley in the power spectrum corresponds to them. In addition, RGB LEDs are more expensive than PC LED due to the requirement for more advanced packaging. Another concern for RGB LEDs is proper mixing of the light because the sources must have some finite distance between them, which may affect the lighting uniformity at a distance far from the source.

To solve these problems, first, new RGB phosphors need to be developed to improve color mixing and performances; second, new LED structure design and improved efficiency to couple light into phosphor should be initiated to overcome these problems[18, 19]. A dual wavelength LED structure, with one active region emitting where λ_1 ~400 nm or 460 nm emission for efficient pumping of the blue/green phosphor, and another active region with λ_2 ~460 nm or 530 nm emission matching to the red phosphor, is proposed to improve the color mixing of the solid state lighting (If λ_1 ~400 nm, then λ_2 ~460, and if λ_1 ~460 nm, then λ_2 ~530 nm). This dual wavelength InGaN LED can be fabricated using a tunnel junction, and three terminals are used for independent electrical control of the emission intensity for each wavelength.

A dual wavelength LED with two emission wavelengths at 470nm and 535 nm is used as a reference design as shown in Figure 35[51]. This LED includes two separate PN junctions, and each junction has an active region of InGaN MQWs. These two sets of different MQWs have different mole fractions of indium in InGaN materials, which dictate two different emission wavelengths. These two electrically independent PN junctions are integrated into a single vertical heterostructure. This dual wavelength LED was grown by organometallic vapor deposition on sapphire substrate as depicted in Figure 35. The first PN junction of the LED with a peak emission wavelength about 530 nm, is grown on a n-GaN buffer layer.

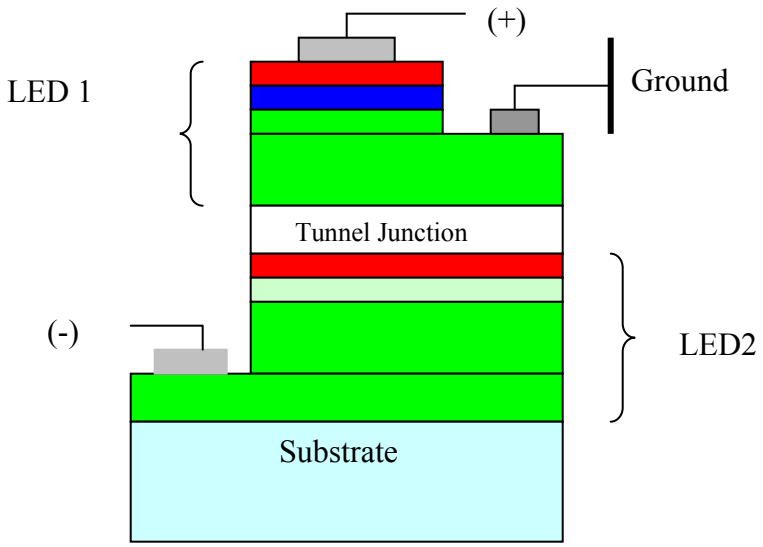

Figure 35: Structure of a Dual Wavelength LED

A 40 nm thick n-InGaN layer is deposited on the top of this buffer layer. Its active region is four $In_xGa_{1-x}N$ MQWs with GaN barriers; with the well width is 3 nm and the barrier width 5 nm. Those layers were followed by a 30 nm thick layer of p-$Al_{.07}Ga_{.93}N$ for electron blocking, and a 100nm thick p-GaN layer.

A p++/n++ GaN tunnel junction (TJ) in this device separates the two PN junctions and makes it three-terminal device. Another function of the TJ is that it serves as a lateral current spreading layer for the PN junction underneath. Figure 36 shows the detailed configuration of this TJ. A 200 nm thick n-GaN cap layer is grown on the top of this TJ followed by a second LED, where a similar MQW structure of $In_xGa_{1-x}N$ is grown, and the indium component is designed to emit a peak wavelength of 470 nm. The device structure of the second LED is very similar to the first one, except for a heavily doped p-GaN cap layer with 50nm thickness for the electrical contact in the second LED. The p-contact was made using a thin layer of Ni and Au on the top of the dual wavelength LED, and the Ni and Au also serve as a current spreading layer to improve the conductivity of p-GaN. Because both Ni and Au absorb some light, the p-contact is also called a semitransparent P-Pad. To fabricate the electrical contact for the common ground and n-contact, two etch

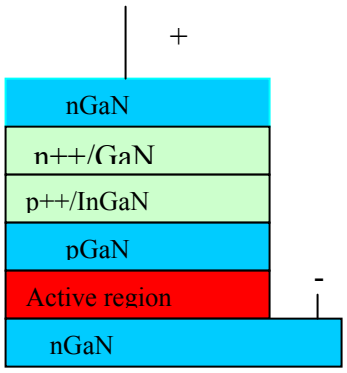

Figure 36: Structure of a Tunnel Junction

steps are required. The first etch, for the n-contact, must reach the n-GaN buffer layer on the top of substrate, and the second etch, for the common ground should reach the n-GaN layer above the TJ.

Finally, Distributed Bragg Reflection grating (DBR) pairs may be applied to this dual wavelength terminal device to form a micro-resonant cavity as shown in Figure 37. The first DBR can be positioned between the n-GaN buffer layer and n-InGaN layer of the bottom LED. The second DBR is just below the p-GaN layer of the top LED. This proposed micro-cavity may triple the light extraction efficiency[4]. In the meantime, it can shape optical beams from both LEDs to improve the color mixing, which is important to light coupling to phosphors. The technical challenge to design and fabricate DBRs for a dual wavelength LED is that the small refractive index difference (contrast) of materials currently available to GaN based LEDs limits the stop bandwidth of DBRs. As a result, currently available DBRs, such as AlGaN/GaN, fail to cover the broad spectrum of dual wavelength LEDs. So, the alternative to DBR pairs may be the application a back reflector at the bottom of the sapphire substrate.

3.2.2 Distributed Bragg Reflection Grating (DBR) for high brightness LEDs

Using a pair of distributed Bragg Reflection gratings (DBR), a resonant cavity can be used to improve light extraction efficiency of LEDs by altering the distribution of spontaneous emissions. For GaN based LEDs applications, there are dielectric DBRs and semiconductor

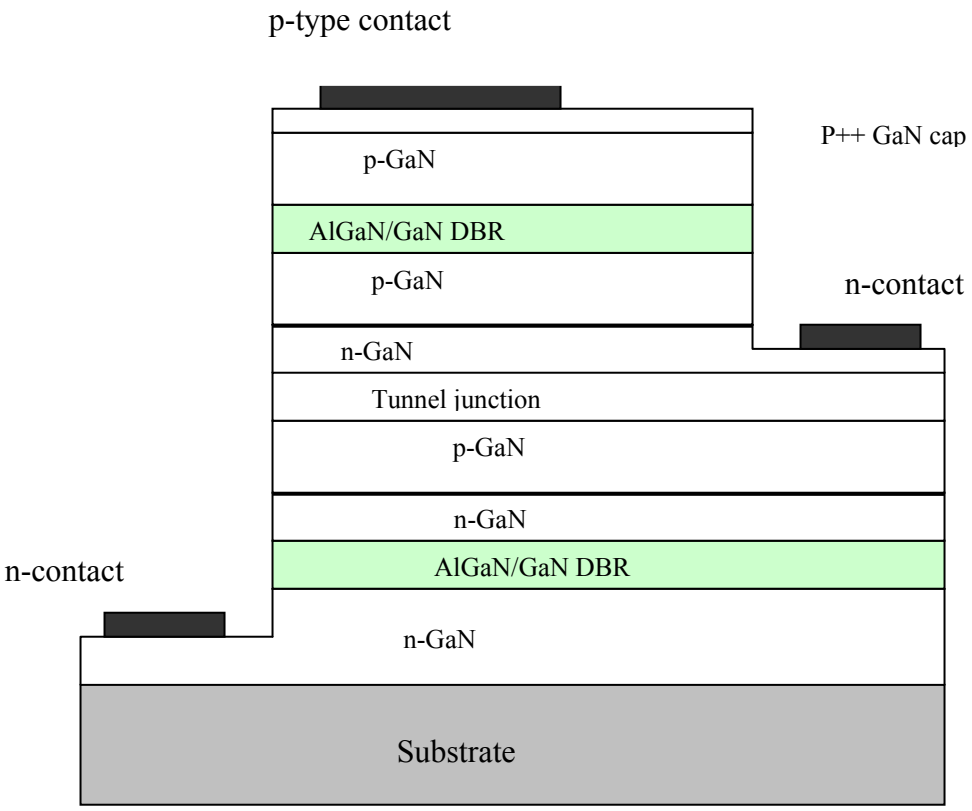

Figure 37: A Micro-Cavity for a Dual Wavelength LED

based DBRs. The dielectric DBR, using HfO_2/SiO_2, offers a large bandwidth of reflection about 80 nm because the relative large difference of refractive indexes between HfO_2 and SiO_2[15]. However, this type of DBR requires more complicated processing. An AlN/GaN based DBR has a medium reflection bandwidth of about 45 nm because the large index of refraction contrast[47]. An in situ grown DBR can an AlGaN/GaN, and this type DBR is easily integrated into a LED structure; however, its limited reflection bandwidth is only about 20 nm[44, 59, 33]. The low contrast of refractive indices of AlGaN/GaN makes the grating a fuzzy DBR. Here, we will focus on the semiconductor based DBRs. The application of DBR to a single wavelength emitter has been successful. Its application to a dual wavelength remain technical challenge because it is difficult to fabricate a DBR to cover the wide optical spectrum of a dual wavelength device, and it is also difficult to select corresponding resonant modes for both peak wavelengths.

3.2.2.1 Theory of Distributed Bragg Reflection Grating (DBR)

Here, we will briefly summarize the concept of a DBR. A DBR structure can be viewed as a periodic structure of layered medium, with two different refractive indices n_1 and n_2, which is shown in Figure 38. A Bloch wave is generated when a plane wave is launched into such a periodic structure. If the Bloch wave falls in forbidden bands, this periodic medium can totally reflect the incident light. By properly engineering refractive indices, a high reflective reflector for a certain selected spectral regions can be realized. For normal incident light into a quarter-wave stack of a DBR, this implies:

$$kn_1a = kn_2b = \frac{1}{2}\pi, k = \frac{2\pi}{\lambda} = \frac{\omega}{c} \tag{14}$$

where ω is the center angular frequency of the reflection band. The reflection bandwidth is given by[65]:

$$\Delta\omega = \omega\frac{4}{\pi}sin^1\left(\frac{|n_1 - n_2|}{n_1 + n_2}\right) = \omega\frac{2}{\pi}\frac{\Delta n}{n} \tag{15}$$

with $n = \frac{n_1+n_2}{2}$. It is the refractive index different that determines the reflection bandwidth, and this reflection bandwidth is very critical for DBR application in high brightness LEDs. The reflectivity of a DBR is another factor to evaluate DBR performance. This reflection

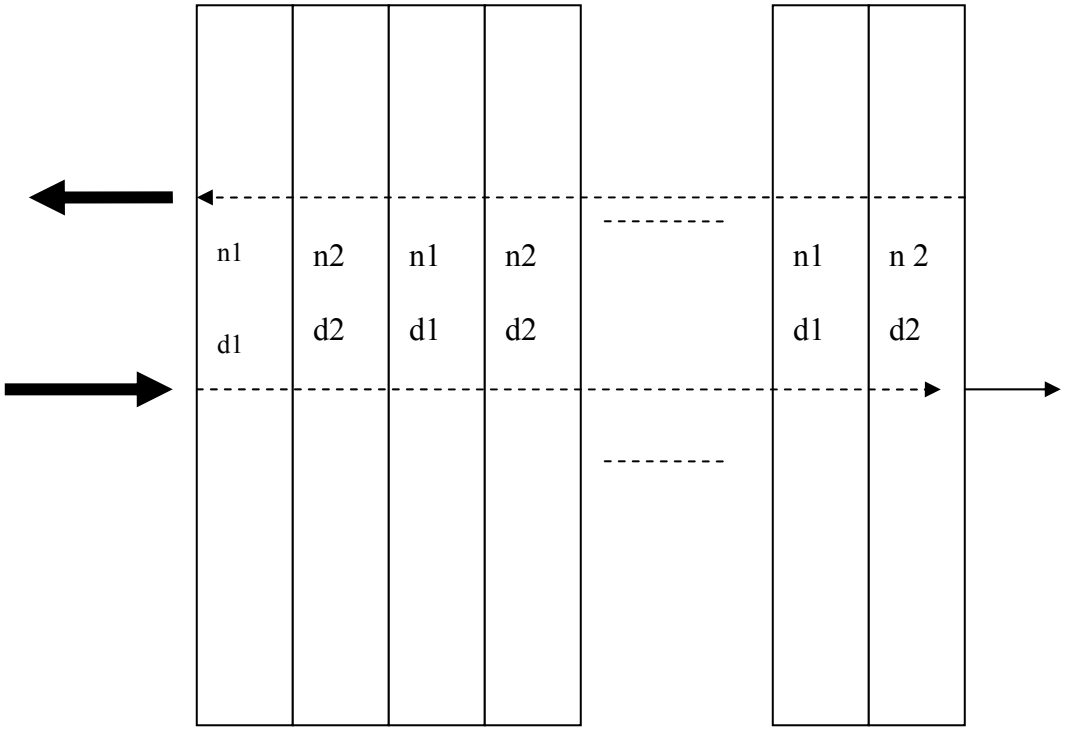

Figure 38: A DBR Diagram

also depends on the number of grating periods in a DBR. Next, we are going to show how to determine the reflectivity of a DBR.

The theory of DBRs can be easily explained using transfer matrix method. The light output and input to this DBR can be related by the following equations for a multilayer structure

$$\begin{pmatrix} E_{0,+} \\ E_{0,-} \end{pmatrix} = \begin{pmatrix} m_{11} & m_{12} \\ m_{21} & m_{22} \end{pmatrix} \begin{pmatrix} E_{s,+} E_{s,-} \end{pmatrix} \tag{16}$$

$$M = D_0^{-1} \left(\prod_{i=1}^{N} D_i P_i D_i^{-1} \right) D_s \tag{17}$$

For TE wave, the matrix D is:

$$D_i = \begin{pmatrix} 1 & 1 \\ n_i cos\theta_i & -n_i cos\theta_i \end{pmatrix} \tag{18}$$

For TM wave,

$$D_i = \begin{pmatrix} cos\theta_i & -cos\theta_i \\ n_i & -n_i \end{pmatrix} \tag{19}$$

The propagation matrix P_i is defined as:

$$P_i = \begin{pmatrix} e^{j\varphi_i} & 0 \\ 0 & e^{j\varphi_i} \end{pmatrix} \tag{20}$$

and φ_i is given by:

$$\varphi_i = \frac{2\pi n_i d_i}{\lambda} cos\theta_i \tag{21}$$

where d_i is the thickness, and θ_i is the ray angle in layer i. Moreover, the transfer matrix M for this DBR can be simplified as:

$$M = D_0^{-1} G^N D_s \tag{22}$$

where

$$G = \left(D_1 P_1 D_1^{-1}\right)\left(D_2 P_2 D_2^{-1}\right) \tag{23}$$

and subscripts 0 and s represent the incident medium and the substrate of the DBR, respectively. For a quarter-wave stack DBR, Equation 21 becomes:

$$\varphi_i = \frac{\pi}{2} cos\theta_i \tag{24}$$

By definition, the reflection coefficient of a DBR is:

$$r\left(\theta_0\right) = \left[\frac{E_{0,-}}{E_{0,+}}\right]_{E_{s,-}=0} = \frac{m_{21}}{m_{11}} \tag{25}$$

The reflectivity of a DBR is a function of refractive indices and layer thickness of the two different materials of the DBR and it is also depends on the number of periods, the incident angles and different polarizations. The bandwidth of reflection of a given DBR is determined by the reflective index contrast of this DBR.

3.2.2.2 Optical modeling for AlGaN/GaN DBR and AlN/GaN DBR

A quarter-wave stack AlGaN/GaN DBR with 35 quarter-wave pairs is simulated first. To design and simulate a DBR, an accurate estimate the refractive indices is required. The

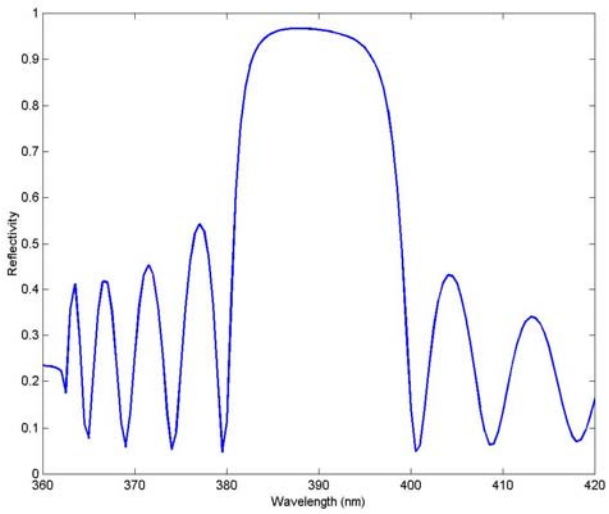

Figure 39: Reflection of AlGaN/GaN DBR from Air

refractive index of GaN for different wavelengths is calculated based on a method presented in[65], and the refractive index of $Al_{0.34}Ga_{0.66}N$ is given by[8] and[34]. To show how the incident medium change performance of this DBR, we take two different media, the air and the GaN material. In each of two incident media, a normal incident light is first simulated, and then an incident angle is changed to 5, 10 degrees without altering this DBR structure. For a normal incidence, the DBR performance is independent polarization states of light; however, the light polarization can affect performances of a DBR when a light incident angle is off the normal. These simulation results are shown in Figures 40-41. For a normal incident, the center of reflection bandwidth is at 390 nm, and the bandwidth is about 15 nm. An incidence with a slanted angle will shift the reflection center to a short wavelength region for the incident medium of GaN.

We also vary the number of the quarter-wave pairs in the DBR with light incidence from air, the center reflectivity is plotted for different quarter-wave pairs as shown in Figure 42. Because the refractive index contrast in an AlGaN/GaN DBR is small, this type of DBR has a limited reflection bandwidth. A DBR with AlN/GaN pairs with large refractive index contrast can increase the reflection bandwidth. To simulate this type of DBR, we also need to determine the refractive indices of AlN and GaN. In our simulation, the refractive index of AlN is 2.16, and the refractive index variations verse different wavelengths are taken into

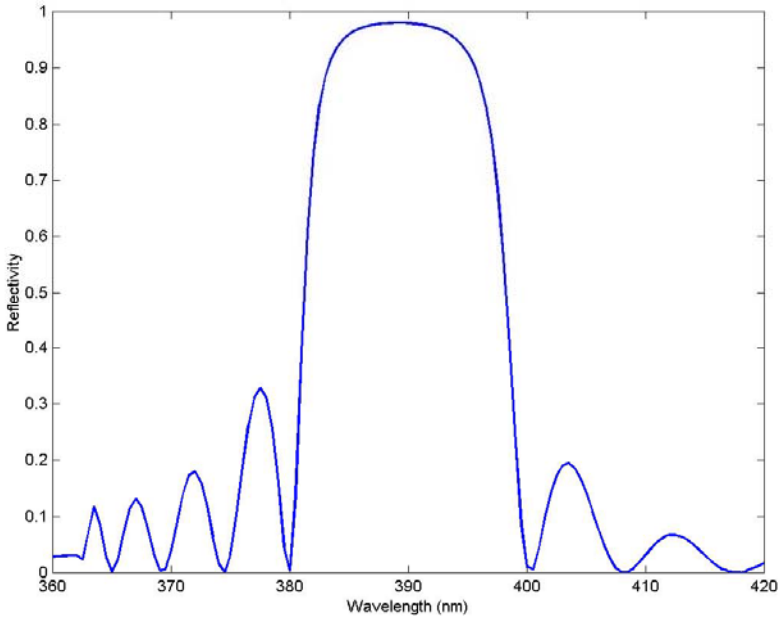

Figure 40: Reflection of AlGaN/GaN DBR from GaN

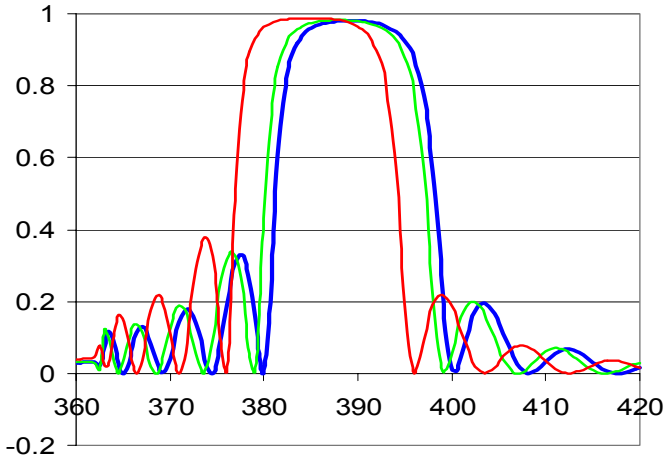

Figure 41: GaN to AlGaN/GaN DBR reflections by angle.

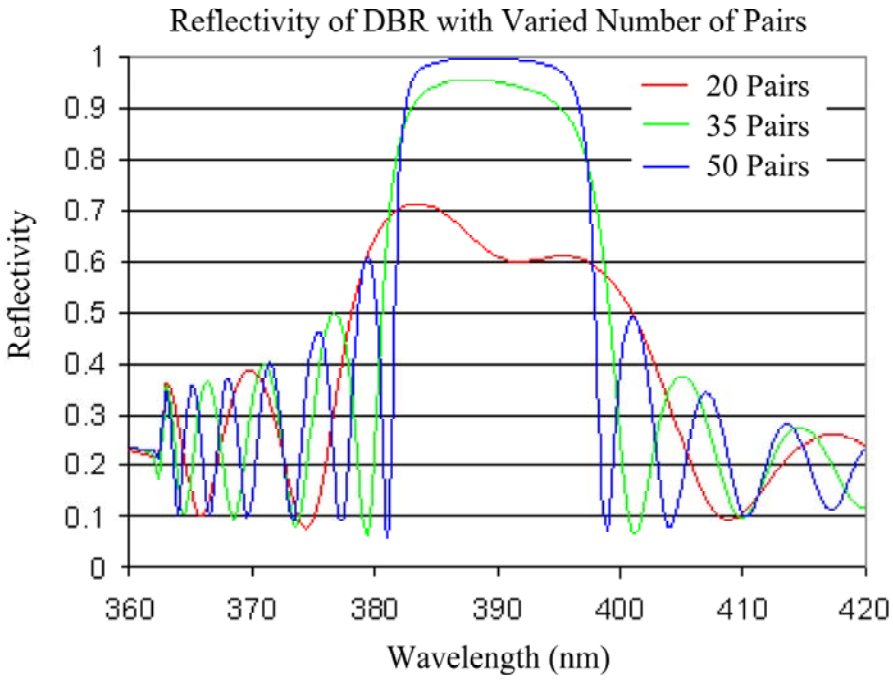

Figure 42: DBR Reflections with Varied Number of Pairs

account[47]. Figure 43 shows the reflection plot for this DBR.

3.2.3 Optical simulations for a dual wavelength LED

To perform optical modeling for a dual wavelength LED, we first need to design InGaN/GaN MWQs for two emission wavelengths. Detailed electric band structures calculation for MWQs requires many fabrication dependent parameters, which is beyond the scopes of this thesis. Here, the following approximation is used to estimate the peak emission wavelength[7, 54]:

$$\lambda_p = \frac{1240}{1.89x + 3.42(1-x) - 3.8x(1-x) + E_{1e} + E_{1h}} nm \tag{26}$$

where x is a low mole fraction of indium of $In_xGaN_{1-x}N$. E_{1e} and E_{1h} denote the first conduct band level and first valence band level of the corresponding MWQs , respectively. Also, a Gaussian distribution is assumed for the optical emission spectrum:

$$\rho(\lambda) = \frac{1}{\sqrt{2\pi}\sigma} e^{\frac{(\lambda-\lambda_p)^2}{2\sigma^2}} \tag{27}$$

The optical spectrum from the dual wavelength LED in Figure 35 can be determined using Equation 26 and 27, which is plotted in Figure 44 for MWQs with the well width of 3

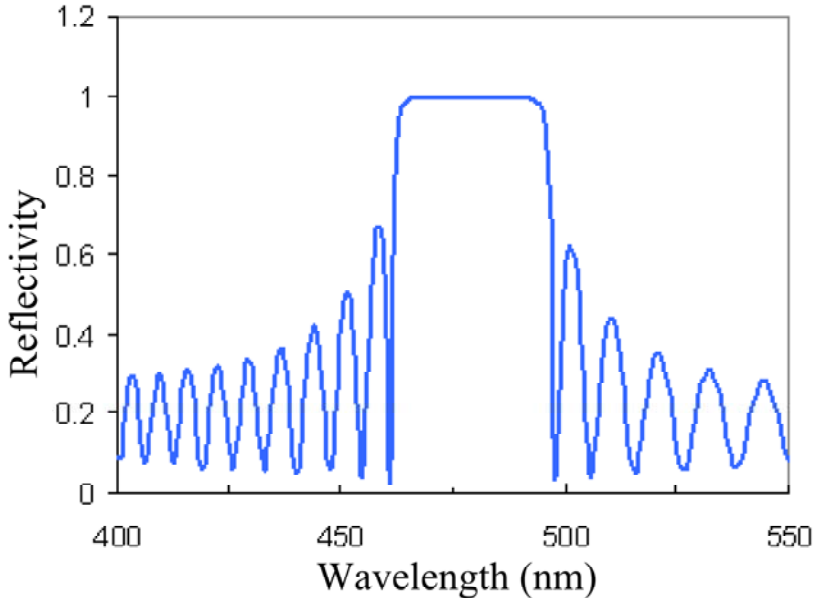

Figure 43: Reflection Plot for AlGaN DBR

nm. The $In_{0.23}Ga_{0.77}N/GaN$ is used to estimate blue emissions and $In_{0.33}Ga_{0.67}N/GaN$ for green emission. Refractive indices for bulk materials of GaN, AlGaN, InGaN, and InGaN/GaN MWQs in a dual wavelength LED are required for optical simulations. First, refractive indices for these bulk semiconductor materials are investigated. Second, an overview of refractive index estimations for InGaN/GaN MWQs is present. Brunner et al have extensively studied the refractive index of $Al_xGa_{1-x}N$[8]. They first calculated the refractive index from transmission measurements, and then use the Adachi model[1] and some fitting parameters to interpolate these experimental data. Finally, the refractive index dispersions can be plotted versus different $Al_xGa_{1-x}N$. The refractive index is estimated as:

$$n(\lambda)^2 = a(x)\left(\frac{hc}{\lambda E_g}\right)^{-2}\left[2-\left(1+\frac{hc}{\lambda E_g}\right)^{\frac{1}{2}}-\left(1-\frac{hc}{\lambda E_g}\right)^{\frac{1}{2}}\right]+b(x) \tag{28}$$

The energy band gap E_g for $Al_xGa_{1-x}N$ can be determined by [54, 8]:

$$E_g(x) = 6.13x + 3.42(1-x) + 1.3x(1-x) \tag{29}$$

Coefficients a(x) and b(x) are from Ref. 66

$$a(x) = 3.17\sqrt{x} + 9.98, b(x) = -2.20x + 2.66 \tag{30}$$

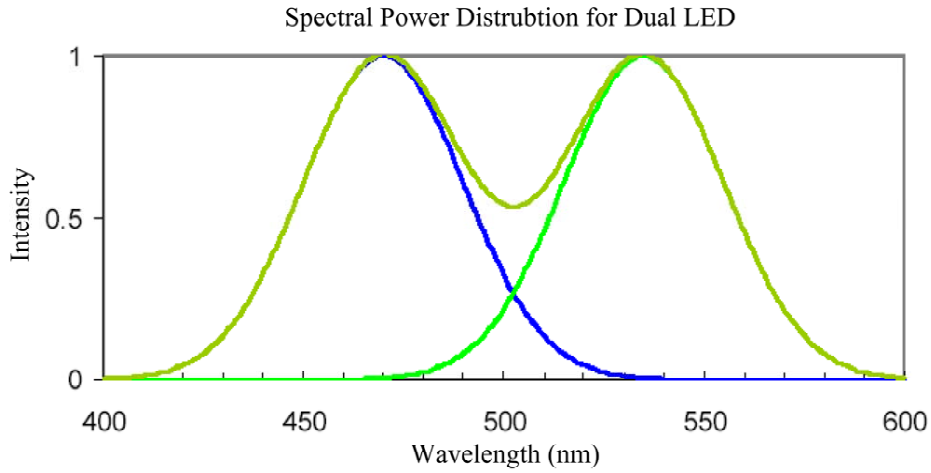

Figure 44: SPD for Dual Wavelength LED

Similarly, the refractive index calculations for $In_xGa_{1-x}N$ also use Equation 28; however, use the following formula to obtain energy band gaps[53]:

$$E_g(x) = 1.9x + 3.4(1-x) + x(1-x) \tag{31}$$

and a(x), b(x) are given by:

$$a(x) = 53.57x + 9.31(1-x), b(x) = -9.19x + 3.03(1-x) \tag{32}$$

Using Equations (7.10-7.14), refractive indices for GaN, AlxGa1-xN and InxGa1-xN can be estimated, some results are shown in Figures 45- 47. Mandy et al developed a comprehensive model to calculate the complex index of refraction of InGaN/GaN quantum well[37]. The complex dielectric function is calculated the QW, which include both quantum effects and continuum contributions. Moreover, continuum contributions are determined by weighting the InGaN well and GaN barrier continuums above the barrier energy without QW effect. If the complex dielectric function is described as $\epsilon(\lambda) = \epsilon_1(\lambda) + i\epsilon_2(\lambda)$, then, the refractive index n and the extinction coefficient κ can be given by:

$$n(\lambda) = \left(\frac{(\epsilon_1(\lambda)^2 + \epsilon_2(\lambda)^2)^{\frac{1}{2}} + \epsilon_1(\lambda)^2}{2} \right)^{\frac{1}{2}} \tag{33}$$

$$\kappa(\lambda) = \left(\frac{(\epsilon_1(\lambda)^2 + \epsilon_2(\lambda)^2)^{\frac{1}{2}} - \epsilon_1(\lambda)^2}{2} \right)^{\frac{1}{2}} \tag{34}$$

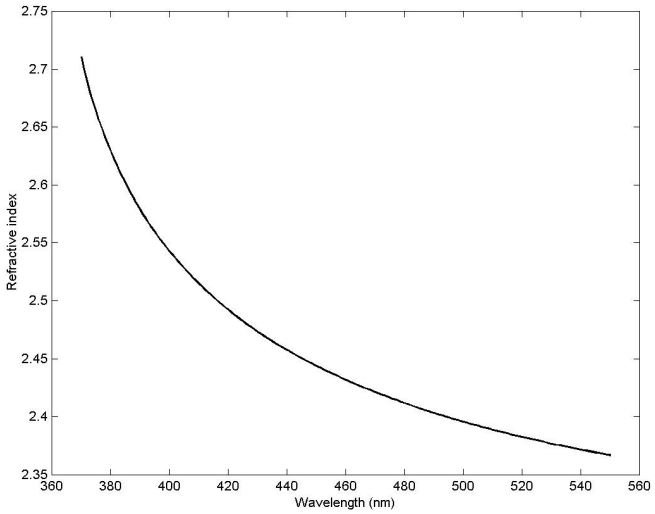

Figure 45: Refractive index plot for GaN

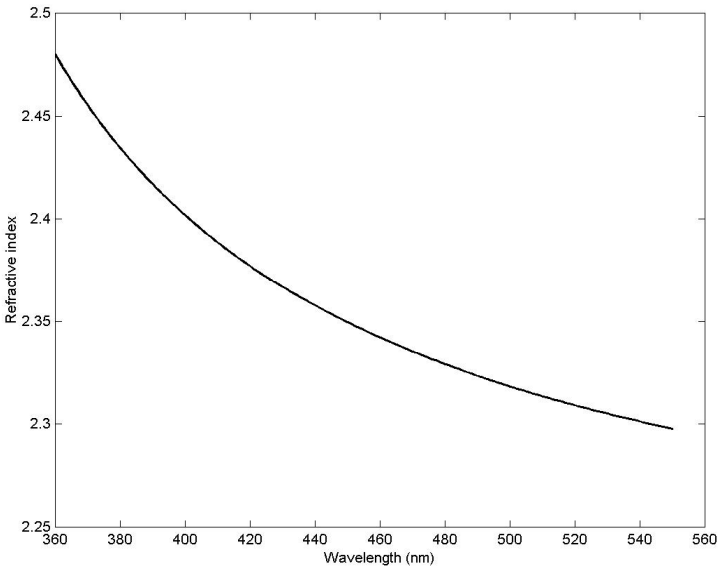

Figure 46: Refractive index plot for $Al_{0.3}Ga_{0.7}N$

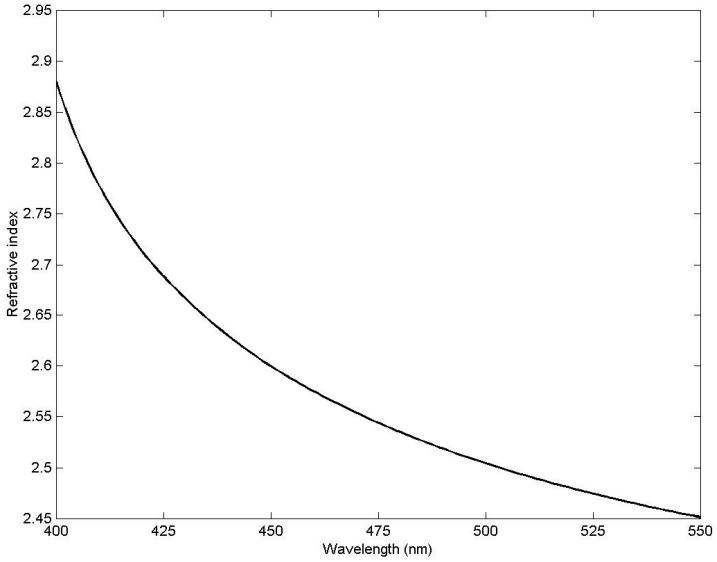

Figure 47: Refractive index plot for $In_{0.1}Ga_{0.9}N$

Table 1: Refractive indices of III-nitrides for simulations

Wavelength	GaN	AlGaN	InGaN(bulk)	InGaN(MQW)
470 (nm)	2.42	2.37	2.55	2.79
530 (nm)	2.38	2.33	2.47	2.6

Based on the above equations and detailed numerical calculations for MQW structures, the refractive index and the extinction coefficient were plotted for different In compositions and wavelengths. However, the refractive index for InGaN/GaN MWQs given by this model is below general accepted values. So the refractive index of MWQs is estimated by that of bulk materials. Before starting to do optical simulations, we list refractive indices for AlGaN InGaN GaN, and InGaN/GaN MQWs in Table 1

3.2.3.1 Optical simulation results

The device structure of this dual wavelength LED is programmed using ASAP optical ray tracing software. Two random light emitters are used to simulate dual wavelength emissions from this LED. More than one millions rays are generated, and a split level 2 as shown in Figure 48 is activated to trace these split rays at each interface from different LED layers. A detector enclosing this whole LED is used to collected the light emission coming from this LED as depicted in Figure 49. Finally, the total light extraction efficiency is calculated

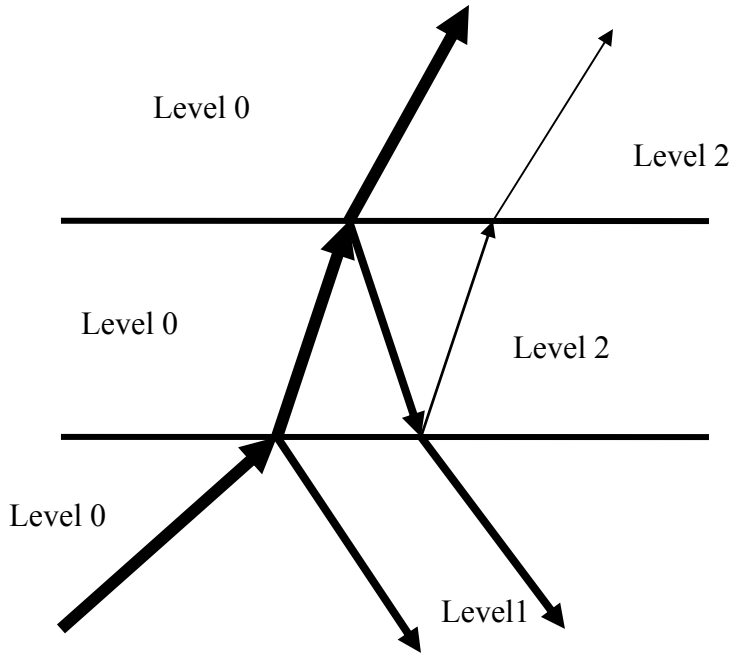

Figure 48: Level 2 ray split of optical ray tracing

based on these results from optical ray tracing. In the simulation, the polarizations of light are averaged. Emission wavelengths are selected from the optical spectrum of the LED as shown in Figure 43.

The top LED with a wavelength of 470 nm is first simulated. Its total light extraction efficiency is 5.5%. Figure 51 shows the 3-D diagram of the LED, and Figure 51 shows a cross section of the LED with some traced rays. Adding a back reflector at the bottom of the substrate does not increase the extraction efficiency of the top LED structure because most

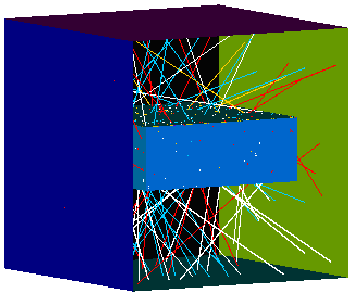

Figure 49: Light extraction efficiency collection configuration

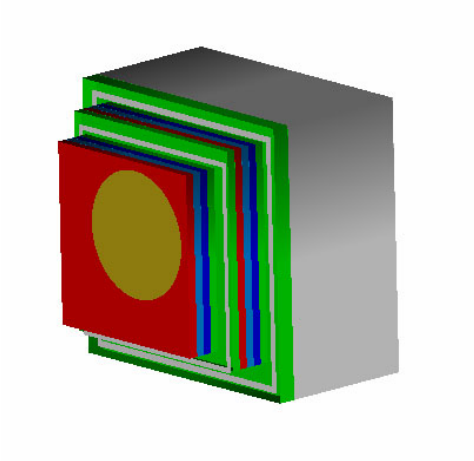

Figure 50: 3-D diagram of a dual wavelength LED

of backward emission light is absorbed or trapped into the bottom LED before reaching the substrate. To see how the refractive index and absorption coefficient of the InGaN in an active region affect the light extraction efficiency, we simulate the extraction efficiency versus index and absorption variation. Results are shown in Figure 52 and Figure 53. As we can see from these results, refractive index variation by 0.5 can change the light extraction efficiency by about 1%. Since the InGaN refractive index is difficult to be determined at a high accuracy[34], simulations for different refractive index variation is very useful to estimate the total extraction efficiency.

Without detailed simulations for the bottom LED with a peak wavelength of 530 nm, we can estimate its light extraction. Since the bottom LED is sandwiched by the top LED, a TJ and the substrate, the light emissions from this bottom LED will go through two cascaded LED structures before reaching out from the top of this dual wavelength LED. As a result, the light extraction efficiency of the bottom LED is roughly equal to the square of the light extraction efficiency for the top LED. Another reasonable guess can be made about the function of the back reflector. Since the bottom LED is close to the back reflector, it should increase the light extraction efficiency, especially the forward light emission. All of these reasonable guess about the bottom LED are verified by simulations. The light extraction efficiency of the bottom LED with a back reflector is 0.39%, close to the square of 5.5%, the light extraction efficiency for the top LED with a peak wavelength of 470 nm. The back

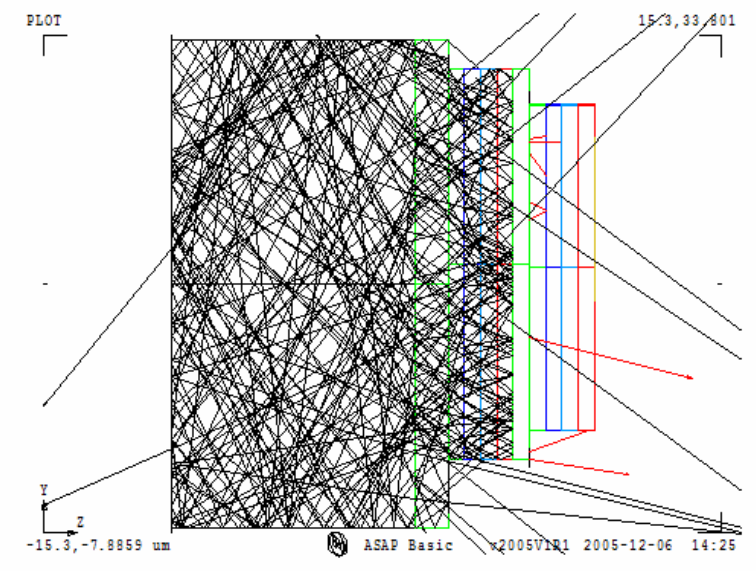

Figure 51: 2-D plot of ray tracing diagram

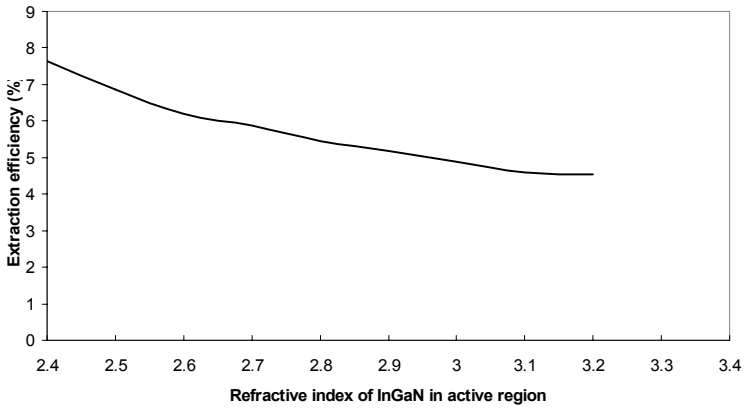

Figure 52: Top LED light extraction vs n for InGaN active region

reflector does increase the light extracted from the top surface of the dual wavelength LED, however, the total light extraction efficiency does not increase so much by adding the back reflector. Most reflected light by the back reflector get absorbed and trapped inside the LED. Similarly, Figure 54 shows the light extraction efficiency versus the refractive index of the InGaN active region, and Figure 55 for the absorption coefficients variation.

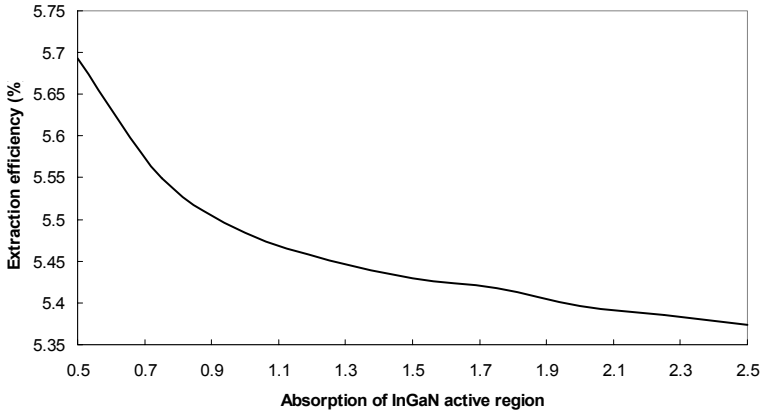

Figure 53: Top LED light extraction vs α for InGaN active region

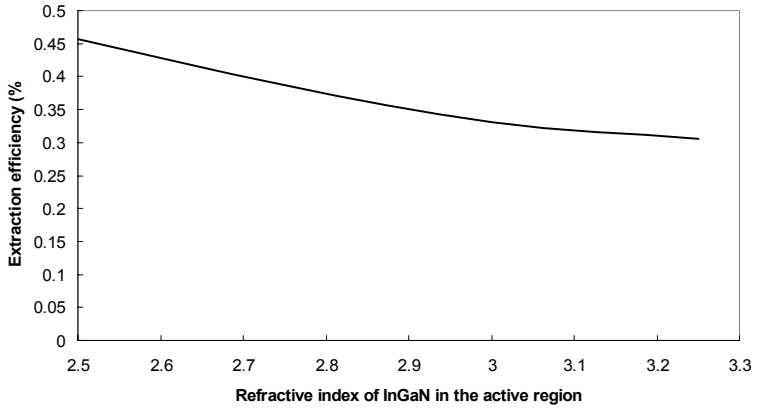

Figure 54: Bottom LED light extraction vs n for InGaN active region

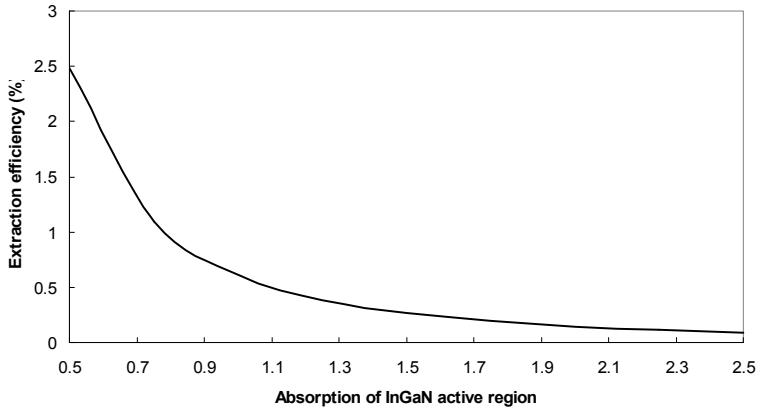

Figure 55: Bottom LED light extraction vs α for InGaN active region

3.2.3.2 Summary

In this chapter, we analyzed the device structure of the dual-wavelength LED. The DBRs based on GaN along with refraction index of GaN, AlGaN and InGaN have been investigated. The light extraction of this dual-wavelength LED has been simulated using optical ray tracing programs. The low light extraction efficiency for the bottom LED presents a problem for this dual wavelength LED application to high efficiency lighting application. The back reflector has some effects on the dual wavelength LED. The refractive index variation has a big impact on the light extraction efficiency than the absorption coefficient of the InGaN in the active region. A micro cavity is required to improve the light extraction efficiency of the bottom LED.

3.3 Electrical Modeling & Device Design

This section covers background theory on p-n junctions, LEDs, quantum wells and tunnel junctions. Electrical modeling of the two terminal dual LED was important to understand its operation and optimize performance. The relationship between drive current and spectral power distribution for the dual LED is discussed.

3.3.1 PN Junction Theory

P-n junctions are critical to the operation of most optoelectronic devices. LEDs are specialized p-n junctions that emit light under forward bias. P-n junctions are the simplest semiconductor junction diode and are formed when a p-type semiconductor and an n-type semiconductor are "brought together." Junction formation can occur via epitaxial growth, diffusion or ion implantation. In this work, however, all junctions were formed through epitaxial growth as discussed in Section 2.2.1.

A number of processes occur when a p-n junction is formed that influence the electrostatics and operation of the diode. When the junction is first formed, there is a large concentration gradient of free carriers that results in diffusion across the junction. Holes will diffuse from the point of high hole concentration (p-type semiconductor) to a point of low hole concentration (n-type semiconductor) and vice versa for the electrons. The holes

leave behind negatively charged acceptor ions in the p-region, and the electrons leave behind positively charged donor atoms in the n-region. The formation of the these immobile charges on either side of the junction results in an electric field across the junction that opposes the diffusion of more free carriers until an equilibrium is reached between the diffusion process and the electric field. Thus, in equilibrium there is no net current flow. The region of immobile positive and negative charges on opposite sides of the junction is known as the depletion, space-charge, or transition region. The width of this depletion region will have an impact on the operation of the device and is given by

$$W = x_n + x_p \tag{35}$$

where x_n and x_p are the widths of the depletion layer in the n and p-regions respectively. Additionally when the junction is at equilibrium a built-in voltage, V_{bi}, is established based on the electric field gradient according to

$$V_{bi} = -\int E dx \tag{36}$$

and can be calculated from

$$V_{bi} = \frac{k_B T}{q} ln\left(\frac{N_A N_D}{n_i^2}\right)(V) \tag{37}$$

or

$$V = \frac{k_B T}{q} ln\left(\frac{n_{NO}}{n_{PO}}\right) \tag{38}$$

where

$$n_{NO} = N_C \cdot e^{\frac{-(\mathcal{E}_g - \mathcal{E}_F)}{k_B T}} \tag{39}$$

and

$$n_{PO} = N_C \cdot e^{\frac{\{(\mathcal{E}_g + qV_{bi}) - \mathcal{E}_F\}}{k_B T}} \tag{40}$$

From these equations the direct dependence on bandgap of V_{bi} can be seen. This is also schematically shown in Figure 56. In Figure 56 the band diagrams for the p-type and n-type semiconductor are shown separately (a) and then when the junction is formed (b). The Fermi level is at the same potential throughout the device at equilibrium and so the bands must bend to accommodate this, creating a built-in potential. Since the Fermi level

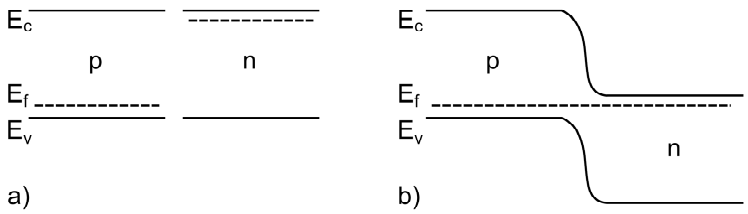

Figure 56: Schematic p-n junction formation

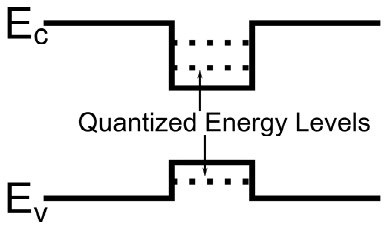

Figure 57: Schematic band diagram for a QW

in the n-type and p-type semiconductors is dependent on the doping level and the respective band edge, then the built-in potential is also dependent on these two properties. V_{bi}, plays a major role in the a device's operating conditions, as it partially determines the forward bias need to operate a device.

3.3.1.1 Quantum wells

Heterojunctions, specifically quantum wells, form the basis of current LED operation. A heterojunction is formed when two semiconductors of different band-gap and/or lattice constant are brought together. Quantum wells are a special type of heterojunctions and in this work were formed by MOCVD. Quantum wells can provide optical and carrier confinement which can drastically improve the performance of a device. A quantum well is formed when a material of lower band-gap is sandwiched between two materials of higher band-gap, as shown in Figure 57 creating a potential well. Carriers are no longer free to move in three dimensions, but are now confined to a 2 dimensional plane. The allowed energy levels can become quantized as shown in Figure 57 dependent on the materials used and the width of the quantum well.

3.3.1.2 Current-Voltage Relationship

Two types of current can flow across the junction: drift and diffusion. Each has a component from the n-region to the p-region and vice versa resulting in four components of current across the junction: $J_h^{p\to n}, J_e^{p\to n}, J_h^{n\to p}, J_e^{n\to p}$. Drift current, $J_h^{n\to p}$ and $J_e^{p\to n}$, are due to thermally excited minority carriers that are "swept" across the junction by the electric field. Diffusion current, $J_h^{p\to n}$ and $J_e^{n\to p}$, depends on the injection of majority carriers to the opposite side and their subsequent diffusion and is exponentially depending on applied bias. At equilibrium the drift and diffusion currents must balance giving:

$$J_h^{p\to n} = J_h^{n\to p} \tag{41}$$

and

$$J_e^{n\to p} = J_e^{p\to n} \tag{42}$$

Junction under forward bias A bias applied to a junction will almost completely drop across the depletion region because of its high resistivity. Thus, the effective bias across the depletion region when a forward bias, V_f, is applied is

$$V_d = V_{bi} - V_f \tag{43}$$

where V_d is also known as the diffusion potential. The band diagrams of a junction under forward bias and reverse bias is shown in Figure 58 (a) and (b), respectively. As the potential barrier is lowered more holes from the p-region and electrons from the n-region can diffuse across the depletion region. However, the same number of holes from the n-region and electrons from the p-region are still contributing to the drift current. The imbalance now present between the drift and diffusion currents leads to a rise in the over all current. For the ideal diode, this current-voltage relation ship is written as:

$$J = J_0 \left(e^{\frac{qV_a}{k_B T}} - 1 \right) \tag{44}$$

where J_0 is the saturation current, and V_a is the applied bias.

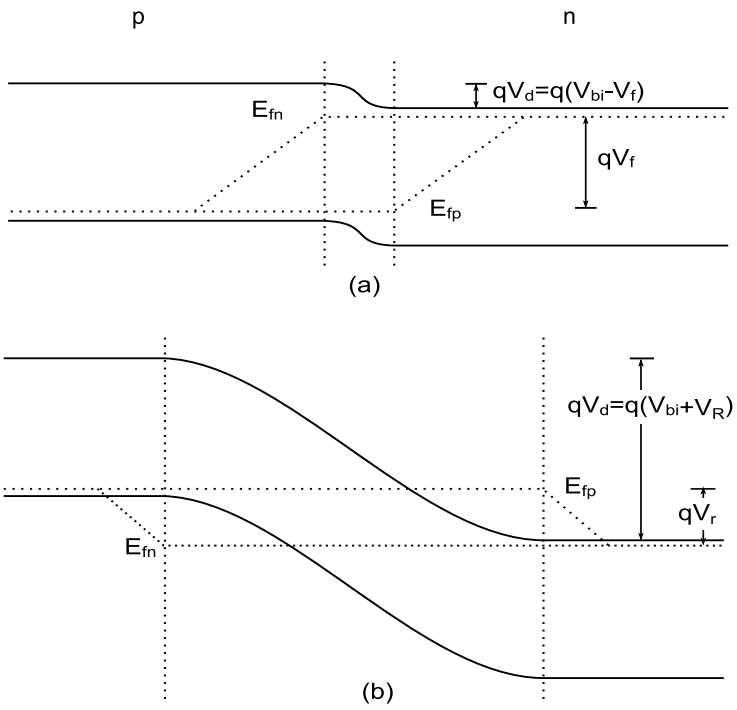

Figure 58: Schematic of a p-n junction under forward and reverse bias

Reverse Bias Once again the applied bias is dropped almost completely across the depletion region as shown in Figure 58(b). The increased barrier height makes it harder for carriers to diffuse across the depletion region, thus the current present, named the reverse saturation current, J_0, is composed of drift current due to thermally generated minority carriers.

$$J_0 = J_h^{n\rightarrow p} + J_e^{p\rightarrow n} \tag{45}$$

It is this saturation current, J_0, that is used in the diode equation.

A plot of diode current from this equation is shown in Figure 59. Reverse bias will be discussed in further detail in Section 4.

3.3.2 LED Theory

Photons with energy near the band-gap are emitted from a junction LED by the process of electroluminescence. This is the same process for light emission from MQW LEDs, but the energy of the photons is dependent on the QW characteristics instead of the junction material. In the case of the homojunction LED electrons are injected into the normally

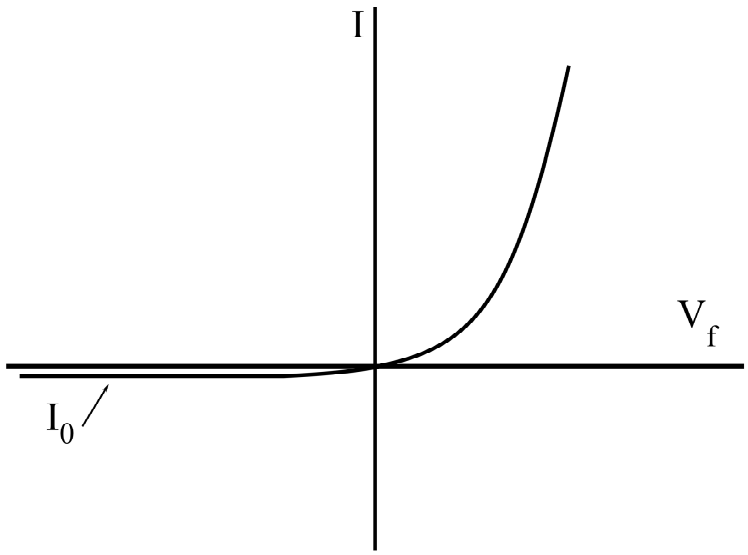

Figure 59: Schematic plot of ideal diode I-V relationship

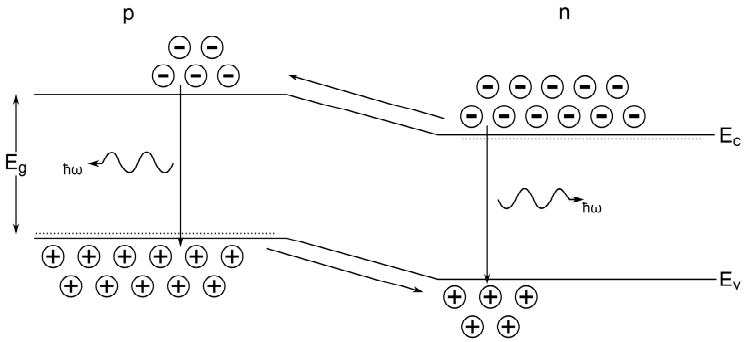

Figure 60: Schematic of light emission from a p-n junction

empty conduction band and recombine with holes in the valence and photons are emitted by spontaneous emission, as shown in Figure 60. In this way an LED converts electrical energy into optical radiation. The process is similar for a LED containing quantum wells, except that the electrons and holes are caught in the quantum well and recombine radiatively there instead of the bulk material, as shown in Figure 61. The photon energy from a MQW (multi quantum well) LED is controlled by changing the QW composition and thickness. The bulk material proprties remain the same. GaN/InGaN/GaN quantum wells were used in this work, where the In composition only was typically varied to provide the desired output wavelength.

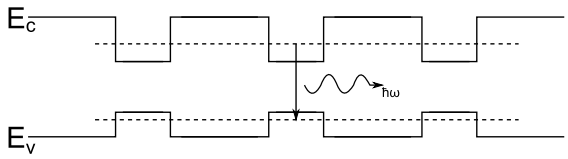

Figure 61: Schematic of light emission from a MQW structure

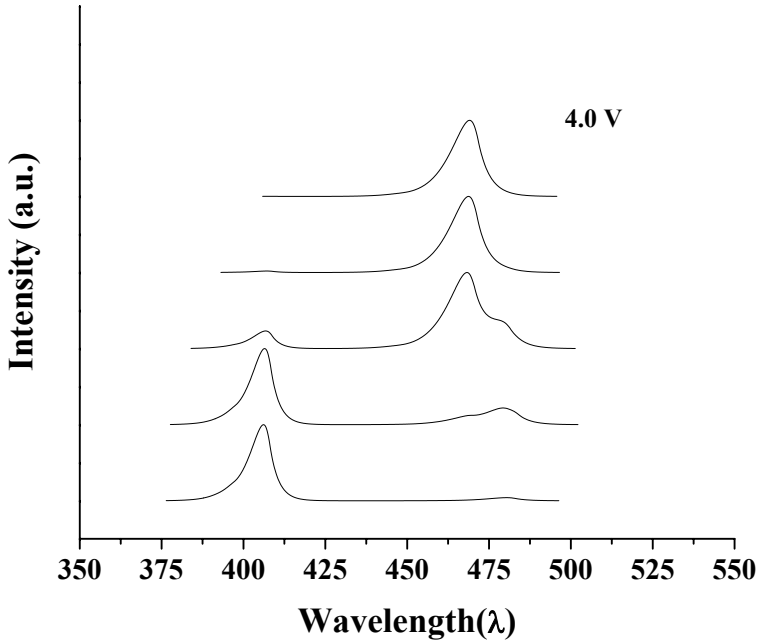

Figure 62: Simulation results for barrier doping of $10^{18} cm^{-3}$

3.3.3 Simulation of Dual LED

3.3.3.1 Simulation with SiLENSe

Simulation of dual LEDs was performed to gain an understanding of the current injection and light emitting mechanisms present in the devices. A commercially available program, SiLENSe, was used for these simulations. β is used to denote the ratio of long wavelength QW intensity to the short wavelength QW intensity in this section and others throughout this work. Figure 62 shows the EL spectra for a simulated device with the barrier between QWs 3 and 4 with electron concentration of $10^{18} cm^{-3}$. Figure 63 shows the change in β with current density. The simulation shows very strong effect of drive current on β that is linear.

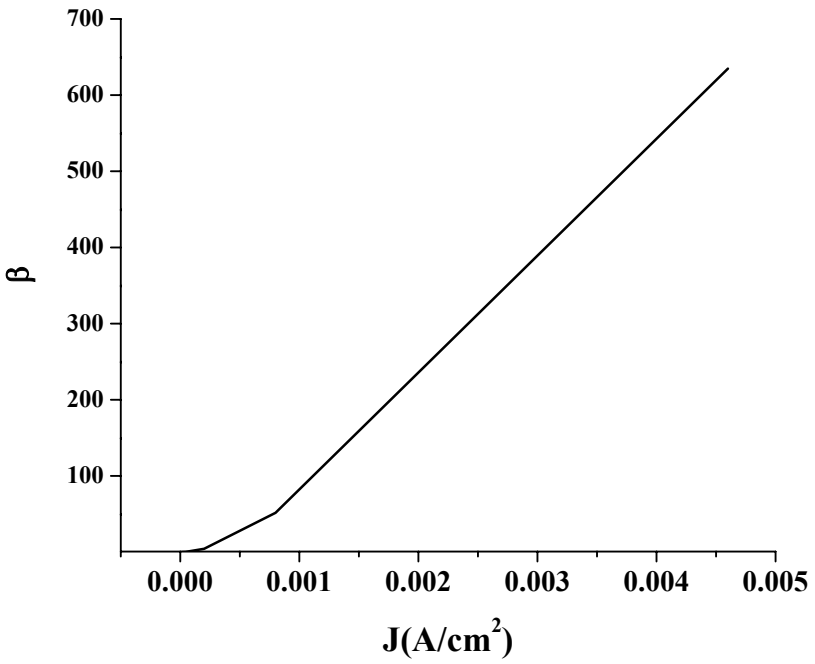

Figure 63: β vs. J for simulated Dual LED with doped barrier

3.3.3.2 Modeling of β for a Dual LED

In Figure 98 the n-type region lies to the left of the QWs and the p-type region is to the right. The relatively high In concentration in the Qws 1-3 leads to electron trapping and blocking, making it more difficult for electrons to travel to QWs 4-6. This effect is best observed in a dual LED with no doping where the QWs 4-6 are preferentially excited at low currents. In the case of no doping holes are more free to move to QWs 1-3 than electrons are to move to QWs 4-6 at low currents. As current is increased the electrons fill higher energy states and are able to travel to QWs 4-6. At this point the mobility of the carrier influences β. QWs 4-6 are more preferentially pumped because holes have lower mobilities and do not travel as far as the electrons, thus recombination is more likely in QWs 4-6. On the other hand, the doping of the barrier between QWs 3 and 4 creates a barrier to hole transport to the QWs 1-3. In the case of the doped barrier the hole blocking washes out the effect of electron blocking at low currents. The holes are trapped in QWs 4-6 until current is high enough to promote some holes over the doped barrier and into QWs 1-3. At this point the

electron trapping effect influences β and recombination preferentially occurs in QWs 1-3. β is the ratio of the intensity of the long wavelength peak to that of the short wavelength peak which is the same as the recombination rates in each of those regions. Thus,

$$\beta = \frac{R_l}{R_s} \tag{46}$$

where, R_l and R_s are the recombination rates in the long and short wavelength regions respectively. The rate for spontaneous recombination which is true for LEDs can be expressed as

$$R = B_r np \tag{47}$$

where B_r is a the recombination coefficient in units of $\frac{cm^3}{s}$ and n and p are the electron and hole concentrations. B_r is related to the transition probability [], and is temperature dependent. Thus,

$$\beta = \frac{R_l}{R_s} = \frac{B_r n_l p_l}{B_r n_s p_s}. \tag{48}$$

It can be seen that electron trapping in the relatively deep quantum wells of the long wavelength region will be higher than hole trapping in the short wavelength quantum wells, as shown in Figure 64, which is the band diagram of a MQW region with undoped barriers. On the other hand, hole mobilities are higher which will keep holes in the short wavelength region. Thus, two rate equations control β with an undoped barrier MQW: (1)electron trapping in wells and (2)hole transport due to low mobility. Experimental data will show that electron trapping dominates at low current densities while hole transport dominates at higher current densities. However, if the middle barrier is doped as shown in Figure 65, hole transport to the long wavelength region is further limited by the lowering of the band diagram in the middle. It can also be seen that further increases in doping concentrations of the barrier will further limit the transport of holes. to the long wavelength region. The wells of the long wavelength region remain the same after doping and will continue to trap electrons. Thus, two rate equations control β with an doped barrier MQW: (1)electron trapping in wells and (2)hole transport due to doped barrier. However, contrary to an undoped barrier experimental data will show that hole transport dominates at low current densities while electron trapping dominates at higher current densities as is expected. Figure 66

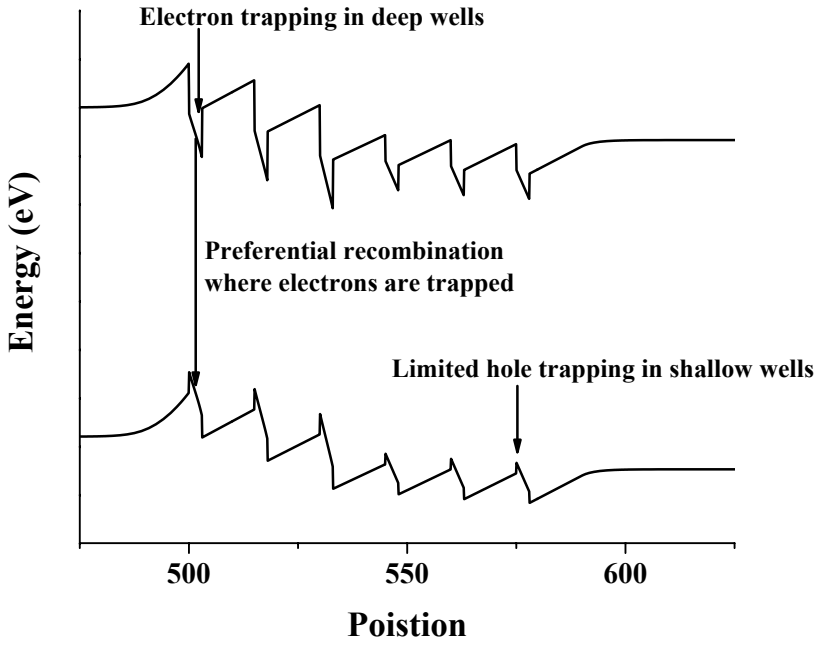

Figure 64: Band Diagram of undoped MQW

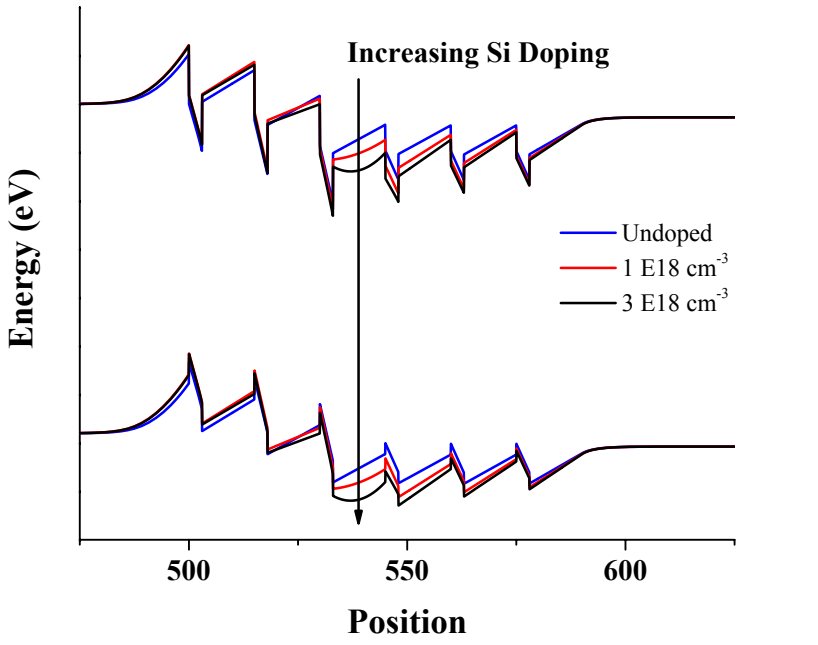

Figure 65: Band Diagram of a doped barrier MQW

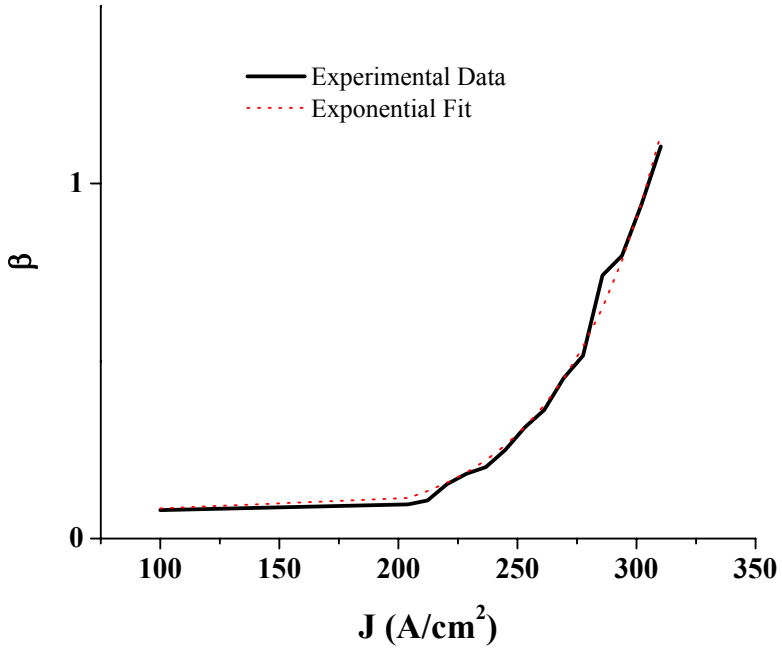

Figure 66: Modeling of $\beta(J)$ using an exponential function

shows how $\beta(J)$ can be modeled using an exponential function of the form:

$$\beta(J) = Ae^{J/B} + C \tag{49}$$

where for this case $A = 0.00067, B = 42.53 and C = 0.02$. Further results show that barrier doping concentration affects A inversely. In this model the electron concentration in the long wavelength region, n_l and the hole concentration in the short wavelength region, p_s, will remain unchanged. Only the electron concentration in the short wavelength region, n_s and the hole concentration in the long wavelength region, p_l will change. Thus,

$$\beta = C\frac{p_l}{n_s} \tag{50}$$

where C is a constant dependent on n_l, p_s and b_r.

CHAPTER IV

III-NITRIDE TUNNEL JUNCTIONS

4.1 Introduction

III-nitride tunnel junctions were grown by MOCVD. Various novel doping schemes to create highly doped p-type GaN were employed with Mg as the acceptor ion. Highly doped p-type material (p++) is necessary for creating efficient tunnel junctions that act as buried current spreading layers and provide high quality contacts to p-type GaN. Molar flow ratios and growth temperature were varied to achieve maximum doping concentration. SIMS and Hall effect were used to measure Mg incorporation and carrier concentration, respectively. The maximum carrier concentration achieved employed a hybrid growth scheme that achieved high carrier concentration and high quality material by alternating layers of high and low growth temperature material. The hybrid growth scheme developed here is a novel growth process that enhances p-type GaN. Successful GaN tunnel junctions were grown using the hybrid p-type doping scheme developed in this work. I-V measurements were taken on these devices to evaluate the effectiveness of the devices.

High hole concentrations in GaN are difficult to achieve due to the high thermal ionization energy (∼180 meV) of Magnesium (Mg) in GaN. At room temperature less than 1% of Mg acceptors are typically electronically active[23]. Therefore, in order to achieve acceptable hole concentrations, high Mg incorporation far above normal doping densities is required. This high doping concentration, however, decreases the crystalline quality of the film, which consequently increases its resistivity and makes it difficult to obtain good electrical contacts to the material. Resistive films cause current crowding in LEDs[24]. A semitransparent contact is deposited onto the entire surface of the p-type region to compensate for current crowding; this is followed by a smaller but thicker bonding pad. The cost of using this semitransparent current spreading layer is a reduction in light extraction from the device by not entirely transmitting the incident light. Post-growth treatment of GaN:Mg

is another important issue. Typically, material is annealed in a non-H_2 environment to break the compensating Mg-H bond that occurs in metal organic chemical vapor deposition grown GaN:Mg[46]. Reports show that optimization of the annealing process can lead to more effective activation of Mg acceptors[22]. Some reports suggest that annealing in air (containing O_2) can further increase Mg activation in GaN[39].

Current crowding poses a problem for buried p-type contacts in an LED. It is not possible to deposit a metal current spreading layer similar to a top p-type contact and a simple bonding pad will not provide enough current spreading for an efficient device. Hence, a tunnel junction is one solution to contacting buried p-layers. In this work, p+ GaN layers have been developed for use in a tunnel junction that may be used in two and three terminal devices for solid state lighting applications.

4.2 Tunnel Junction Theory

4.2.1 Overview of a Tunnel Junction for GaN Based LEDs

Electron tunneling results from a quantum mechanical phenomenon from the wave nature of electrons[7]. When an electron wave is incident with energy less than the energy barrier height, there is a probability that this electron can penetrate this energy barrier, and the penetration depth depends on the barrier height. Figure 67 shows a rectangular barrier with potential height of V, and thickness of d. For an electron wave with energy E_v, the tunneling probability is given by[7]:

$$T\left(E_v\right)=\left[1+\frac{V^2 sinh^2\left(kd\right)}{4E_v\left(V-E_v\right)}\right]^{-1}, k=\sqrt{\frac{2m\left(V-E_v\right)}{\hbar^2}} \tag{51}$$

where m is the effective mass of an electron, $\hbar$ is the plank constant. The tunnel probability is high for very thin barriers. For arbitrary shape of potential barriers, a numerical solution can be obtained by approximating the potential barrier with multiple sub-potential layers, each sub-potential layer can be treated as a constant potential layer. Equation 51 is used to calculate the tunneling probability for each of these constant potential barriers.

In semiconductor materials, carriers can be generated by band to band tunneling when a strong electric field presents, for example, the electric field greater than $10\frac{MV}{cm}$[54]. For a reversed biased, heavily doped, thin pn junction, if the electron penetration depth is

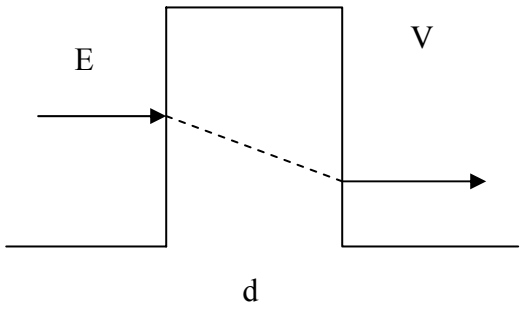

Figure 67: Potential Barrier for a Tunnel Junctio

larger than the depletion width of this pn junction electrons at valence bands at p side can penetrate into conduction bands at n side to become free carriers. This is the so called tunneling junction. The uses of a tunnel junction (TJ) in III-Nitride LEDs have been demonstrated recently[25]. The reverse biased TJ is to improve the lateral current spreading. With a TJ, n-GaN can be used to replace p-GaN as a top cap layer. Commonly, a so called semi-transparent p-Pad is usually applied on the top of p-GaN to overcome the low conductivity of p-GaN In conventional LEDs. The n-GaN has much higher conductivity, about 100 times, compared to p-GaN , and the reverse biased TJ supplies holes to p-GaN adjacent to the active region through lateral current. As a result, the application of n-GaN top contact layer can improve the current spreading of the LED, and increase light extraction by avoiding using semitransparent contact. Another benefit of using a TJ is the simplification of the LED fabrication process because n-GaN can be used as to implement both the top p-contact and lower n-contact as shown in Figure 36. The TJ usually is fabricated using heavily doped p++/n++ either InGan/GaN or GaN/GaN bi-layer. One example use an InGan/GaN bi-layer with layer thicknesses of 15 nm/30nm[15]. The p-type doping Mg level is about 10^{20} cm^{-3}, and n-type doping Si level is about $6x10^{19}$ cm^{-3} for this tunneling junction. This TJ is incorporated into a resonant cavity LED with violet light emission. The resonant cavity of this LED uses two pairs of DBRs: the top one is a SiO_2/HfO_2 above the TJ, and the bottom one is an AlGaN/GaN DBR grown on a GaN buffer layer. A TJ in the second example is fabricated using a GaN/GaN layer with layer thicknesses of 10nm/10 nm. The p+ GaN layer is doped with $3x10^{19}$ cm^{-3} of Mg; the

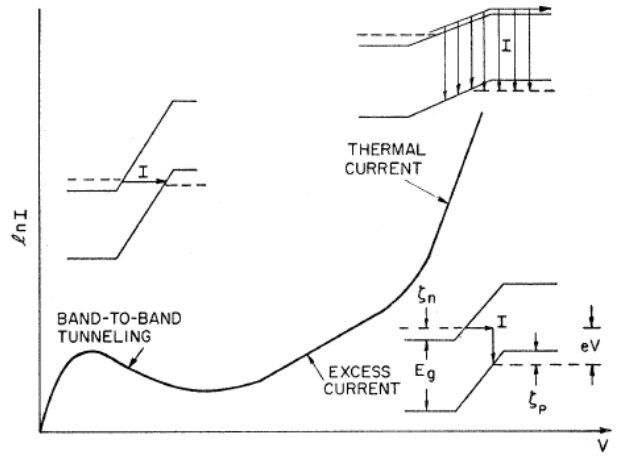

Figure 68: Current-voltage characteristic of a degenerate p-n junction.

averaged Si doping level in the n+ GaN layer is about 10^{20}cm^{-3}. A n-GaN is grown on the top of this TJ to replace the conventional p-GaN as a top contact layer. One disadvantage of the TJ is its large forward voltage, about 1 volt higher than that of a conventional LED because the TJ add a series resistance to the LED. However, the overall optical power of a LED is claimed to double compared to the conventional LED with a top semitransparent p-Pad[25]. A necessary characteristic to tunneling is the negative differential resistance (NDR) region in the forward bias operation of a tunnel diode, because it shows the existence of band-to-band tunneling (Figure 68)[42]. In the NDR region a decrease in the density of states leads to a decrease in tunneling probability and a subsequent decrease in current density[27]. Kane derived an equation for the current density of a tunnel diode as shown in Equation 52[27].

$$j_t = \frac{em^*}{18\hbar^3} e^{\frac{-\pi\sqrt{m^*}E_G^{\frac{3}{2}}}{2\sqrt{2}\hbar F}} \left(\frac{\overline{E}_\perp}{2}\right) \times \int \left[f_1\left(E_1\right) - f_2\left(E_2\right)\right] \left[1 - e^{\frac{-2E_s}{\overline{E}_\perp}}\right] dE \tag{52}$$

where E_s is the smaller of E_1, E_2. Kanes work will be used as a basis for understanding and quantifying the observed tunneling mechanisms in the GaN device. Full analysis of the current-voltage characteristics will lead to a better understanding of the device, although tunnel junctions for this work will be operated in the reverse bias region. A better understanding of GaN based tunnel junctions will help to optimize them for incorporation as more efficient contacting layers in LEDs. Currently, the presence of a tunnel junction increases

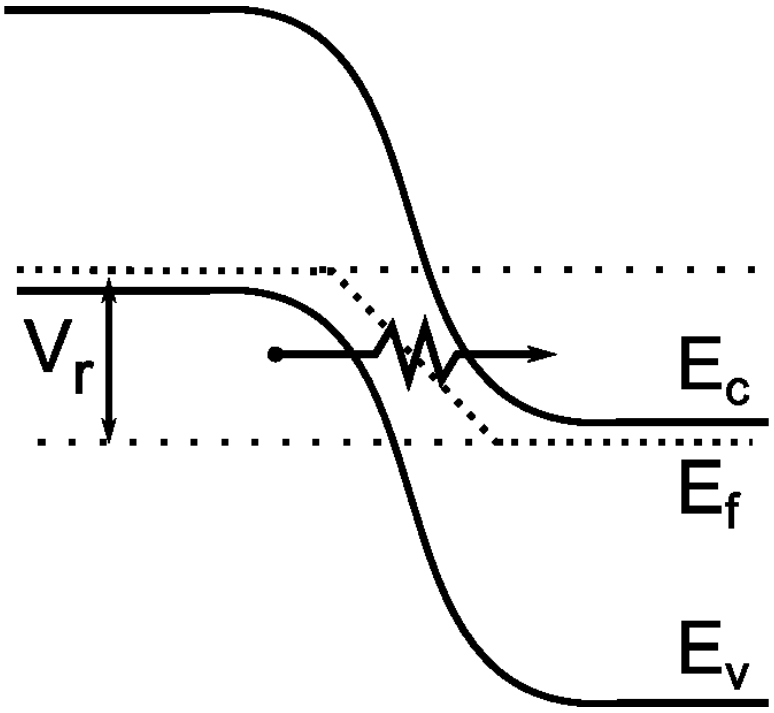

Figure 69: Tunnel Junction in reverse bias showing tunneling current

the series resistance of the device by 33% [26] over a typical LED with semitransparent current spreading layer. A goal of this research will be to reduce the series resistance of GaN tunnel junctions.

4.3 Hybrid p-type Doping

Hybrid doping was the first doping scheme employed in the tunnel junction development. Three sets of runs were performed to optimize hole concentration and material quality. The first set of growths was at high temperature (∼1030°C) in which the molar flow ratio of Cp_2Mg/TMGa was changed from 0.00556 to 0.0667 in order to incorporate more Mg into the films and maintain a high quality epitaxial layer. The second set of runs repeated the change in molar flow ratio of Cp_2Mg/TMGa from the high temperature runs, but with a lower deposition temperature (∼980°C). The third set of growths, hybrid p-type doping, consisted of alternating layers of high and low temperature p-type GaN repeated 10 times. The high temperature layers were doped with a molar flow ratio of 0.0334 Cp_2Mg/TMGa, while the low temperature layers were highly doped with a molar flow ratio of 0.0459 Cp_2Mg/TMGa. It is important to note that in the first and second set of growths the

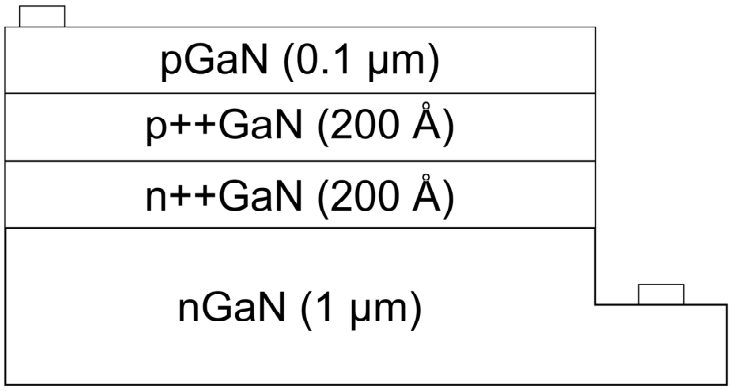

Figure 70: Schematic of the layer structure used in tunnel junction growths

molar flow ratio was set by changing the Cp_2Mg flow and maintaining a consistent TMGa flow. However, in hybrid p-type doping, the molar flow ratio was set by changing either the TMGa flow or the Cp_2Mg flow. It is believed that decreasing the amount of available gallium allows for higher rates of Mg incorporation. For all growths, NH_3 flow was held constant.

Several tunnel junctions were grown where the p++ layer was varied according to the three sets of growth runs described in this work (a general schematic of the devices is shown in Figure 70). A GaN buffer layer was grown on top of a bare sapphire substrate at low temperature (500°C to 600°C) followed by high temperature (∼1050°C) undoped GaN and then an n-type GaN with SiH_4 as an n-type dopant at a molar flow ratio of 3.51 to TMGa. The TMGa was switched with TEGa for the n+ layer (highly doped n-type GaN), which was grown at low temperature (∼980°C), and SiH_4 was used as an n-type dopant at molar flow ratio of 48.3 to TEGa. To ensure a better interface between the n+ and p+ layers a thin layer of undoped GaN was introduced as a barrier to magnesium diffusion. The device was capped with high quality p-type GaN.

The activation process was also changed, in addition to varying the temperatures and molar flow ratios of Cp_2Mg/TMGa. A standard rapid thermal annealing (RTA) process was used at 800°C with N_2 ambient. Also, lower temperature (500°C) atmospheric anneals were performed after some reports indicated that oxygen could enhance the activation process[39]. The atmosphere anneals were done at times ranging from 5 minutes to 3 hours.

Table 2: Summary of P-GaN doping data

Sample Name	**A(HT)**	**B(LT)**	**C(LT)**	**D(Hybrid)**
Mg/Ga Flow Ratio	0.014	0.050	0.100	0.025 (HT)/ 0.045(LT)
RMS Roughness (Å)	3.3	9.7	25.5	7.2
Hall Effect (cm^{-3})	1×10^{17}	3×10^{17}	2×10^{18}	2×10^{18}

Secondary Ion Mass Spectroscopy (SIMS) was used to measure Mg incorporation in the layers. Hall measurements were used to determine hole concentration and atomic force microscopy was used to measure surface quality. Scratch diodes and lithographically fabricated diodes were used to test for tunneling in the tunnel junction devices.

4.3.1 Results of Hybrid Doping

The results for Hall effect and AFM measurements are shown in Table 2 The variation of Cp_2Mg/TMGa ratio at high temperatures had little effect on hole concentration as measured by Hall effect or Mg incorporation as measured by SIMS. At higher deposition temperatures with Mg incorporation of $5 \times 10^{19} cm^{-3}$, hole concentrations of $\sim 1 \times 10^{17} cm^{-3}$ were achieved for RTA and atmospheric annealed samples, and surface morphologies remained good, up to a Cp_2Mg/TMGa ratio of 0.0459. However, at lower deposition temperatures with Mg incorporation of $1 \times 10^{20} cm^{-3}$, hole concentrations $> 1 \times 10^{18} cm^{-3}$ were achieved with atmosphere annealing and increased Cp_2Mg/TMGa flow ratio, but these samples exhibited poor surface morphology. Finally, the hybrid p-type doping, described above, achieved good surface morphology and hole concentrations $> 1 \times 10^{18} cm^{-3}$ using the standard RTA activation process, while no atmospheric annealing was performed on these samples as mentioned in the preceding section. In the hybrid doping, the balance between the Mg incorporation and the surface quality depended on the TMGa molar flow and the layer thickness of the respective temperature growths. Different Cp_2Mg molar flows were evaluated for the high and low temperature growth layers while keeping the TMGa molar concentration constant, but regardless of temperature they lead to poor surface quality and thus poor contacts. Lowering the Cp_2Mg molar flow greatly improved the surface quality, but it also reduced the carrier concentration and a working tunnel junction could not be achieved. A substantial improvement in the carrier concentration, from $1 \times 10^{17} cm^{-3}$ to $1 \times 10^{18} cm^{-3}$, without

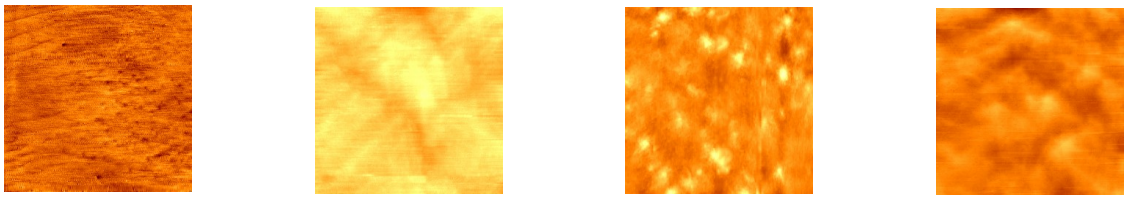

(a) (b) (c) (d)

Figure 71: AFM images of p-type doping

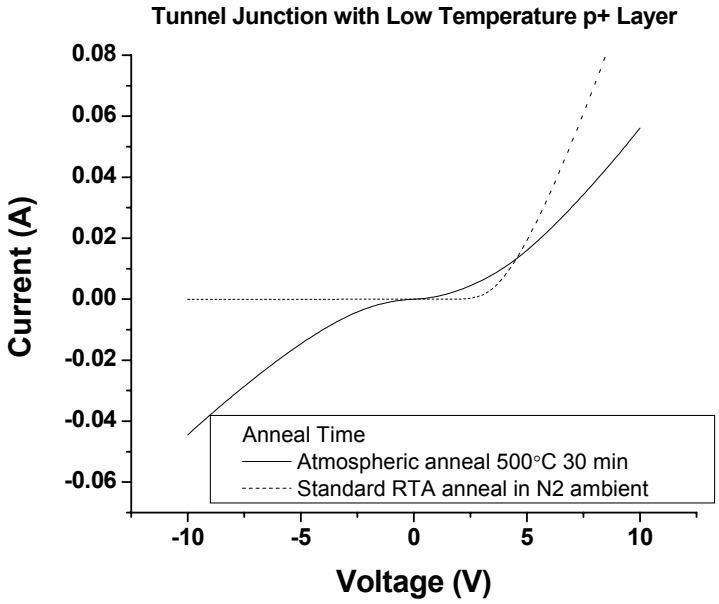

Figure 72: Effectof atmosphere anneal vs N_2 RTA

diminishing surface quality was seen when the Cp_2Mg molar concentration was kept constant for both the low temperature and high temperature layers, while the TMGa molar concentration was reduced for the low temperature layers.

Tunnel junctions employing p+ layers from each of the three growth runs exhibited different properties. Junctions with a high temperature p+ layer exhibited no tunneling, only typical diode behavior; this was true for both annealing processes. On the other hand, low temperature p+ layers showed tunneling when the sample was atmosphere annealed, but not after the standard RTA, Figure 72.

RTA under a N_2 ambient showed no effect on surface morphology as viewed under an optical microscope. Conversely, the atmosphere annealing caused a deterioration of the surface and was not used with the hybrid doped devices. Diodes (tunneling and normal)

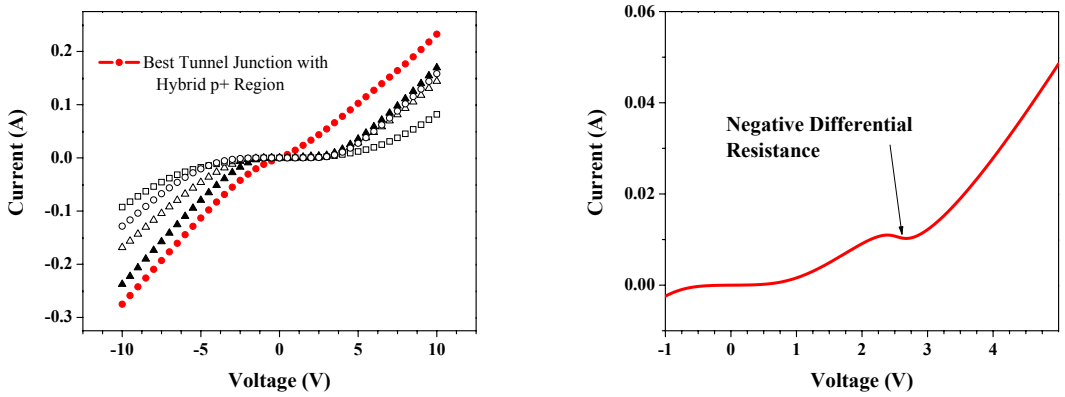

(a) (b)

Figure 73: I-V plot of (a) several TJs using hybrid p doping and (b) NDR

processed with the atmosphere anneal showed higher resistance. This can be seen as a smearing of the I-V curve in Figure 72.

4.3.2 Discussion of Hybrid Doping

The first method for p+ doping did not allow for enough Mg incorporation into the GaN. Ga incorporation is more efficient at higher temperatures, blocking the incorporation of Mg. However, the quality of GaN is preserved, as observed by surface inspection. At lower growth temperatures it is possible to incorporate more Mg and activate more acceptors, but the quality of the crystal surface tends to deteriorate. If the lower temperature p+ layers are used as a buried contact, the overgrown layers suffer from poor crystallinity, and a complex device becomes impossible.

Hybrid doping of the p+ region combines the good crystallinity of higher temperature GaN:Mg with the higher doping potential of low temperature materials. Higher Mg incorporation rates are achievable, by decreasing the TMGa flow relative to the Cp_2Mg flow, due to the lack of available Ga that would normally prevent Mg incorporation. In addition layers with high Cp_2Mg/TMGa molar ratios were kept thin to minimize disturbance to the crystal. Tunneling was achieved as shown by the I-V curves and the N-type negative resistance exhibited in Figure 73. Such a device is a good candidate for a buried contacting and current spreading layer in other devices, eliminating the need for the p-type material to

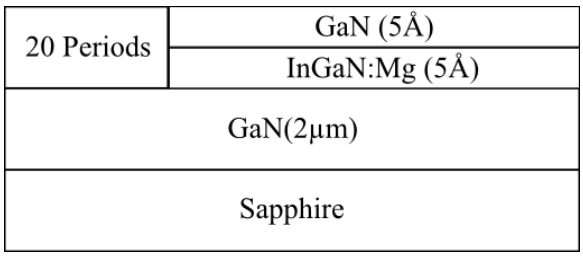

Figure 74: Schematic of nSPS test structure

be the top layer. Tunnel junctions have also been demonstrated as fully transparent current spreading layers on the top of devices [25].

Atmospheric annealing in normal atmospheric conditions was also evaluated as a way of increasing the activation of Mg in GaN. While some improved carrier concentrations were observed with Hall measurements, a tradeoff came in material quality deterioration. Although there may be some optimal condition for activation without unacceptable material degradation, such a method is unsuitable for a buried p+ layer, because it is essentially capped from the oxygen that is believed to cause higher activation efficacy.

4.4 Short Period Superlattice Doping

GaN/InGaN short period superlattice (SPS) structures doped with Si or Mg were investigated as possible doping schemes for a III-nitride tunnel junction. SPS structures have been suggested as and reported to have the potential for achieving higher carrier concentrations than bulk layers[30, 58, 40, 28]. The superlattices in this work had periods of 5 Å GaN and 5 Å InGaN. The test structures were each comprised of 20 periods. Hall and PL spectroscopy measurements were performed on the SPS test structures to evaluate their quality. Junctions were then grown using the Mg doped SPS and Si SPS structures and evaluated as tunnel junction devices

4.4.1 Si Doped SPS Structures

SPS test structures were grown with varying levels of silicon doping. The test structure consisted of 20 periods of alternating Si:InGaN and GaN layers of 5 Åthickness grown on top of 1.5 μm of undoped GaN on a sapphire substrate, as shown in Figure 74. Both the InGaN and GaN layers were grown at ∼800°C, which is the normal growth temperature

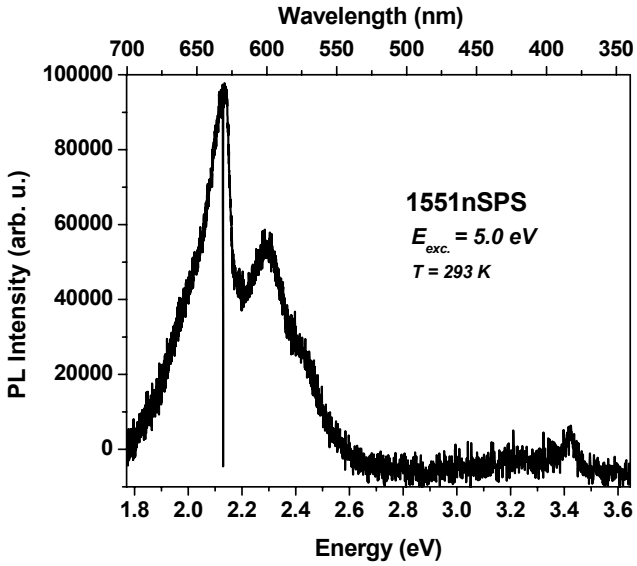

Figure 75: PL Spectrum for nSPS test structure

for InGaN. However, high quality GaN is normally grown at ∼1000°C. In this structure the quality of the material is preserved as characterized by AFM, XRD, and PL. AFM measurements provide a RMS surface roughness of 10 Å, while Figure 75 is PL data for the SPS structure showing a GaN peak at 3.4 eV. Hall effect measurements showed electron carrier concentrations in excess of $1 \times 10^{20} cm^{-3}$.

4.4.2 Mg Doped SPS Structures

Magnesium doping was introduced instead of silicon to investigate the properties of a pSPS structure. The growth was performed at 800°C for both the GaN and InGaN. The doping concentration was maximized using feedback from PL spectroscopy and Hall effect measurements. PL spectra of three samples are shown in Figures 76, 77 and 78. The flow of Mg into the chamber during growth is the only difference in these structures. The growth was performed at 800°C for both the GaN and InGaN. Sample A is shown as a baseline doping concentration. Sample B has twice the Mg flow and Sample C has half the Mg flow. Each of the PL spectra shows strong Fabry-Perot oscillations indicating high quality interfaces in the superlattice. Each spectra also shows a peak near 2.8 eV arising from the superlattice

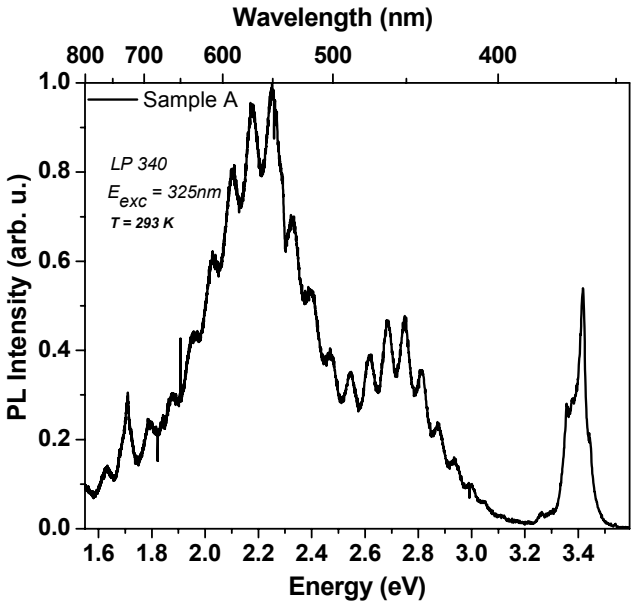

Figure 76: PL spectra of baseline pSPS doping

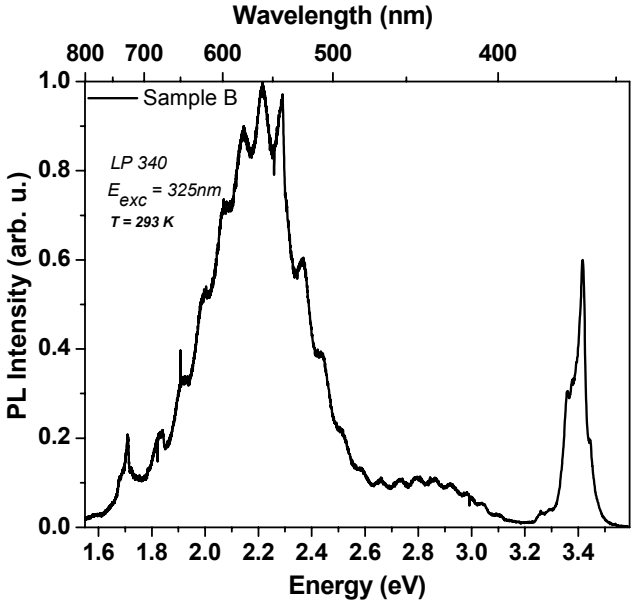

Figure 77: PL spectra of twice baseline pSPS doping

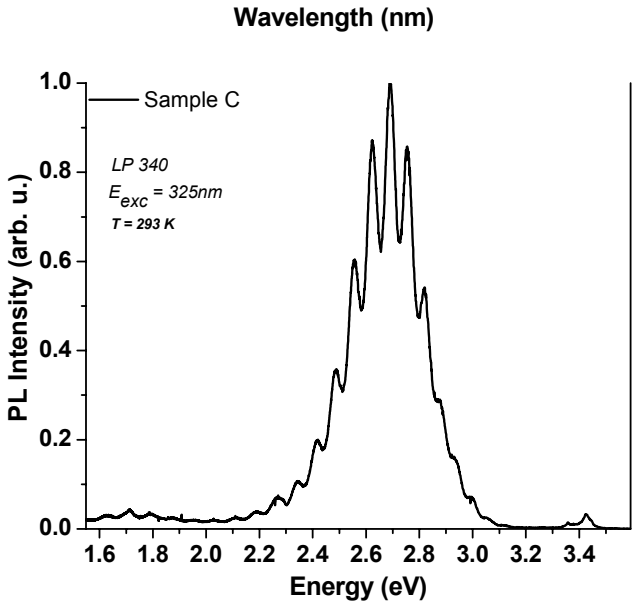

Figure 78: PL spectra of half baseline pSPS doping

Table 3: Carrier concentrations for pSPS samples

	Sample A	**Sample B**	**Sample C**
Hole Concentration	1.99×10^{18}	8.86×10^{17}	3.65×10^{18}
Mg Flow	Baseline	Twice	Half

InGaN composition. Samples A and B have another peak in their spectra that is due to defects in the material from over doping of Mg. The relative intensity of the defect band to the SPS peak indicates the level of defects in the material. For instance, in sample B which has twice as much Mg flow as sample A, the defect band nearly washes out the SPS peak. However, in sample C there is no defect band, indicating that there is no overdoping from Mg. This explanation is corroborated by the results of Hall effect measurements shown in Table 3. The hole concentration for sample C is higher than that of samples A and B which indicates that the samples are suffering from compensation effects from over doping of Mg.

4.4.3 SPS junctions

The SPS test structure described in the previous sections were then used to form a pn junction. Two variations of the structure are shown in Figure 79. The n SPS layer was the same as in the Section 4.4.1 and the pSPS layer was the same Sample C in Section 4.4.2.

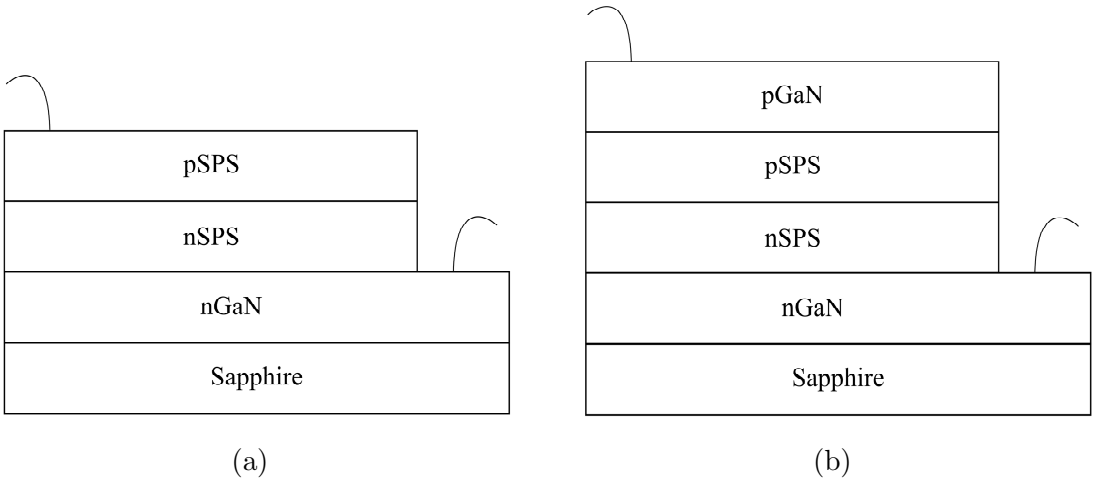

Figure 79: Schematics of two variations of SPS junctions

Current voltage measurements were performed on the devices to assess them as tunnel junctions, however, very little reverse current could be achieved. It is unclear whether further optimization of these structures would lead to a tunnel junction.

4.5 Mn Doping

Mn doping was introduced into a tunnel junction structure similar to the one mentioned previously that used the hybrid p-type doping scheme to assess its effect on tunneling behavior. Mn dopants tend to have energy levels in the middle of the bandgap for GaN, which may lead to defect enhanced tunneling. Normally, as the tunnel junction is driven in to reverse bias, tunneling may occur when the valence band of the p-side is at higher potential than the conduction band of the n-side as shown in Figure 69. The tunneling probability is a function of the width of the tunnel barrier, however, if a state exists in that barrier it may act as a transition point for carriers, and improve the tunneling probability as shown in Figure 80. Several devices were grown and fabricated. The layer structures shown in Figure 81 are modified from the tunnel junctions employing the hybrid doping scheme mentioned before. Mn has been introduced into the intrinsic region at the junction between the n++ layer and p++ layer. Table 4 shows the expected Mn concentrations in each of the samples. All other paramters were held constant except the flow of Mn entering the reactor. The current voltage results are shown below in Figure 82. It can be seen that

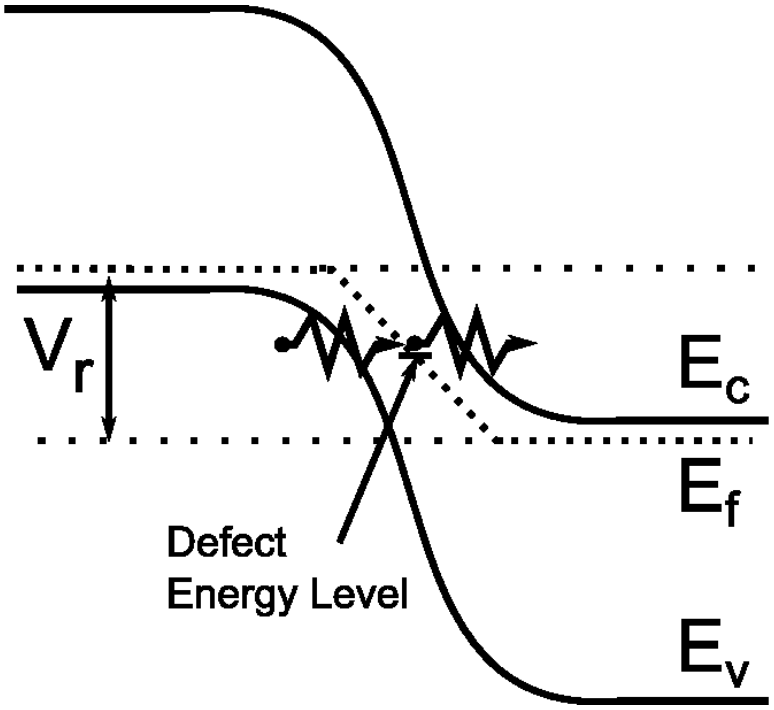

Figure 80: Tunnel junction in reverse bias illustrating defect assisted tunneling

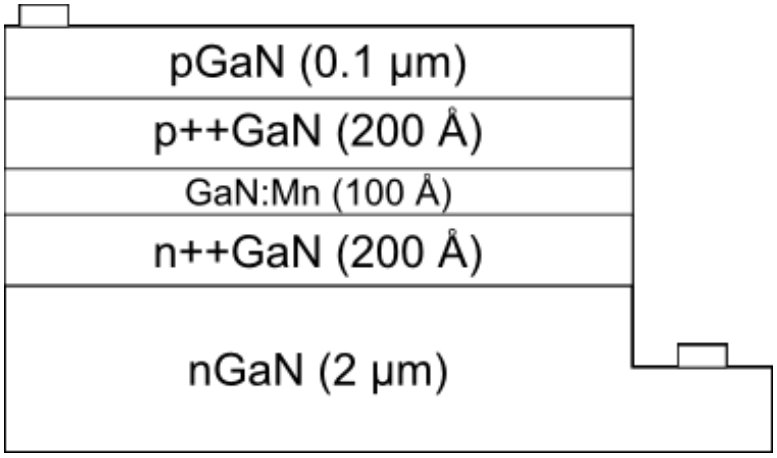

Figure 81: Tunnel junction structure schematic showing GaN:Mn placement

Table 4: Mn doping for tunnel junctions

Sample	Mn Concentration
Low Mn Doping	.5%
Medium Mn Doping	1%
High Mn Doping	2%

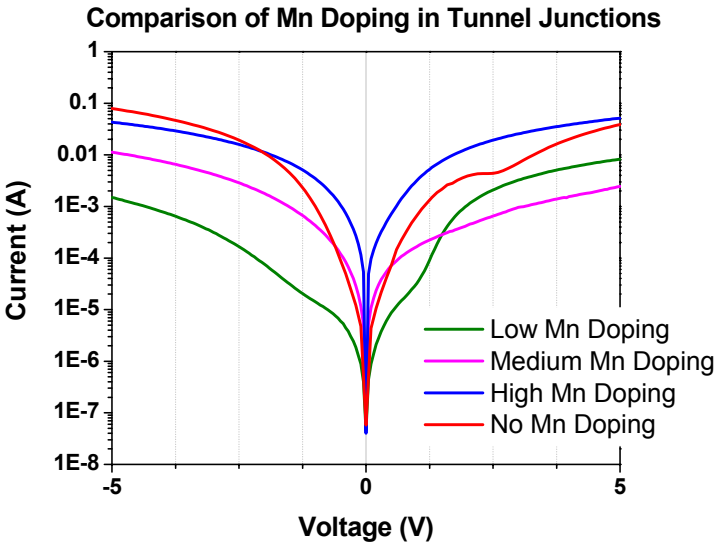

Figure 82: I-V plots of Mn Tunnel junctions

each of the samples containing Mn in the junction has reduced reverse current as compared to the junction without Mn. One explanation for this is that the presence of Mn impurities in the junction increases carrier scattering causing more carriers to give off their energy in the form of photons. A more plausible explanation maybe that the Mn impurities diffused into the p++ layer partially compensating the hole concentration resulting in a fermi level further away from the valence band. A decrease in the p-type doping would increase the tunneling barrier seen by carriers as and decrease the amount of tunneling current as seen by Equation 52.

4.6 Conclusion

Several methods for forming a III-nitride tunnel junction were explored, however, a suitable device for a buried current spreading layer was not achieved. Hybrid doping showed the best results as a tunnel junction however the voltage need to achieve reverse currents suitable for LED operation were too high. SPS doping showed strong potential for obtaining high concentrations of holes in p-type material, however, structures incorporating these layers did not create suitable tunnel junctions. Lastly, Mn doping of an intrinsic region in the junction to create defect assisted tunneling also proved to be not suitable for creating a tunnel junction. A simpler solution for creating a dual wavelength LED is described in

Chapter 6. There are advantages and disadvantages to the two terminal device described in Chapter 6, however, then major advantage is that such a device is attainable.

CHAPTER V

PHOSPHOR TEST BED

5.1 First Generation Phosphor Test Bed

The basis for a BSDLED was demonstrated by pumping a combination of phosphors with multiple wavelengths of excitation, and then varying the relative intensities of those pumps. Such a device is a novel concept and will play an innovative role in solid state general illumination.

A wide variety of phosphors that are excited by a range of pump wavelengths exists. In fact, a single phosphor may respond differently to different pump wavelengths. Thus, a combination of multiple phosphors with differing and exclusive excitation spectra can be simultaneously pumped by multiple wavelengths to produce white light. The relative intensities of the pump peaks can then be varied to change the output of the total device and therefore allow dynamic tuning of the correlated color temperature (CCT). Such a device combines the controllability seen in RGB-LEDs and the broadband characteristics of PC-LEDs. It is believed that such innovations will prove instrumental in the success of solid state general illumination sources that require high quality dynamic white light.

The analyses of several phosphors for use in a dynamic phosphor converted illumination source are reported here. Such a device can be constructed using readily available phosphors and pumped with standard GaN LED emission wavelengths. Pump wavelengths of 400 nm and 460 nm were chosen based on a number of criteria including availability of phosphors and desired output spectrum. The phosphors analyzed here include: UV to white (A), $SrGa_2S_4$ (B), SrCa:Eu (C). Each phosphor was excited by the 400 nm and 460 nm light independently and simultaneously and the output power spectra observed. Phosphor A was strongly excited by 400 and not 460, while the converse was true for Phosphor C as shown in Table 5.

Phosphors A, B and C were then combined based on the results in Table 5 to achieve

Table 5: Phosphor responses to different pump wavelengths

Excitation	Phosphors		
	$SrGa_2S_4$ (Green)	SrCa:Eu (Red)	UV to White
460 nm	Strong	Strong	Weak
400 nm	Strong	Weak	Strong

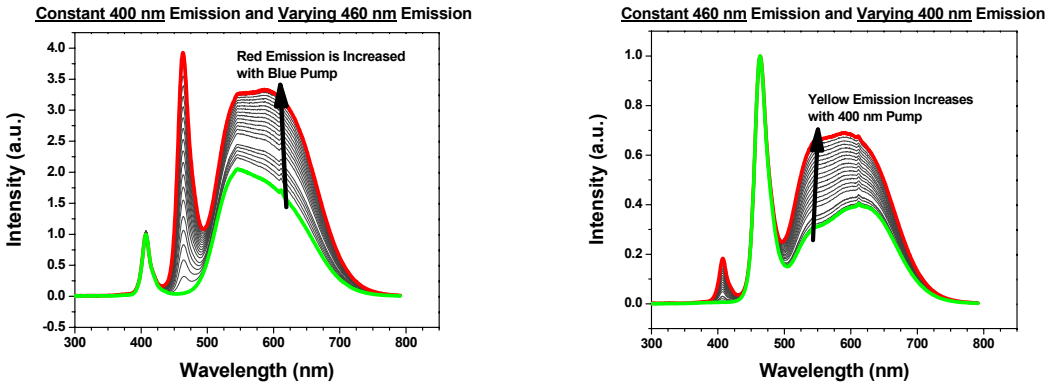

(a) (a)

Figure 83: Phosphorescence for changing (a) 460 nm and (b) 400 nm pump

a source with CCT similar to an incandescent bulb. Next, the dual wavelength source was used to excite the phosphors as the relative intensities of the two wavelengths were varied from singular 460 nm or 400 nm pumping to equal pumping from both wavelengths. Figure 83a and b shows the change in phosphorescence as the intensity of one wavelength is held constant and the other varied for both cases. The shape of the emission curve is shown to change by varying the relative intensity of the two pump wavelengths as denoted by the arrows on Figure 83. Figure 83a shows an increase in the red phosphorescence (655 nm peak) as the 460 nm pump relative intensity is increased. Figure 83b shows that an increase in 400 nm relative intensity is accompanied by an increase in the yellow/green (560 nm peak) phosphorescence. Figure 84 displays the equal intensity spectrum superimposed with the two singular pump spectra and normalized to the phosphor peak of each, clearly depicting the shape change of the phosphorescence spectrum.

Figure 85 shows the varied spectra plotted on a 1931 Commission Internationale De

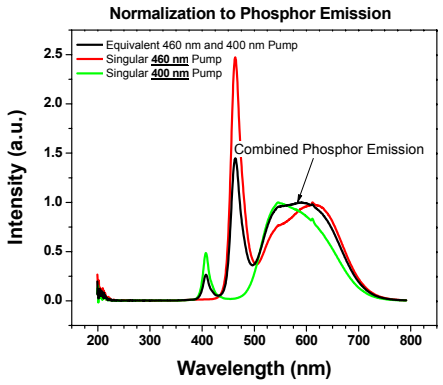

Figure 84: Overlayed phosphorescence spectra for varied pumps

L'eclairage (CIE) diagram showing the variation of chromaticity achievable with this combination of phosphors. Pumping relatively harder with the 400 nm light excites more of the yellow/green phosphor emission moving the chromaticity coordinates closer to the yellow edge of the spectrum. Increasing the relative intensity of the 460 nm pump excites more of the red phosphorescence as well as adding blue light from the pump to the spectrum, thus, shifting the chromaticity coordinates toward the violet edge (bottom left) of the CIE diagram. A large range of points can be accessed with this combination of phosphors and pump choices. In addition, correlated color temperatures (CCT) ranging from 3588 K to 4793 K are achievable. Another important note is the high color rendering index (CRI) of 85 and 82 as listed in Figure 85. These CRIs rival many fluorescent lamps and are attributed to the broad emission from the combined phosphor emission.

5.2 First Generation Phosphor Summary

These results show great potential for BSDLEDs. Such a source is possible by using a three terminal device as described previously and phosphor combinations similar to those analyzed here. Innovations such as this will help solid state illumination sources gain a competitive advantage over conventional illumination sources. This will be necessary for solid state lighting to realize success in the general illumination market.

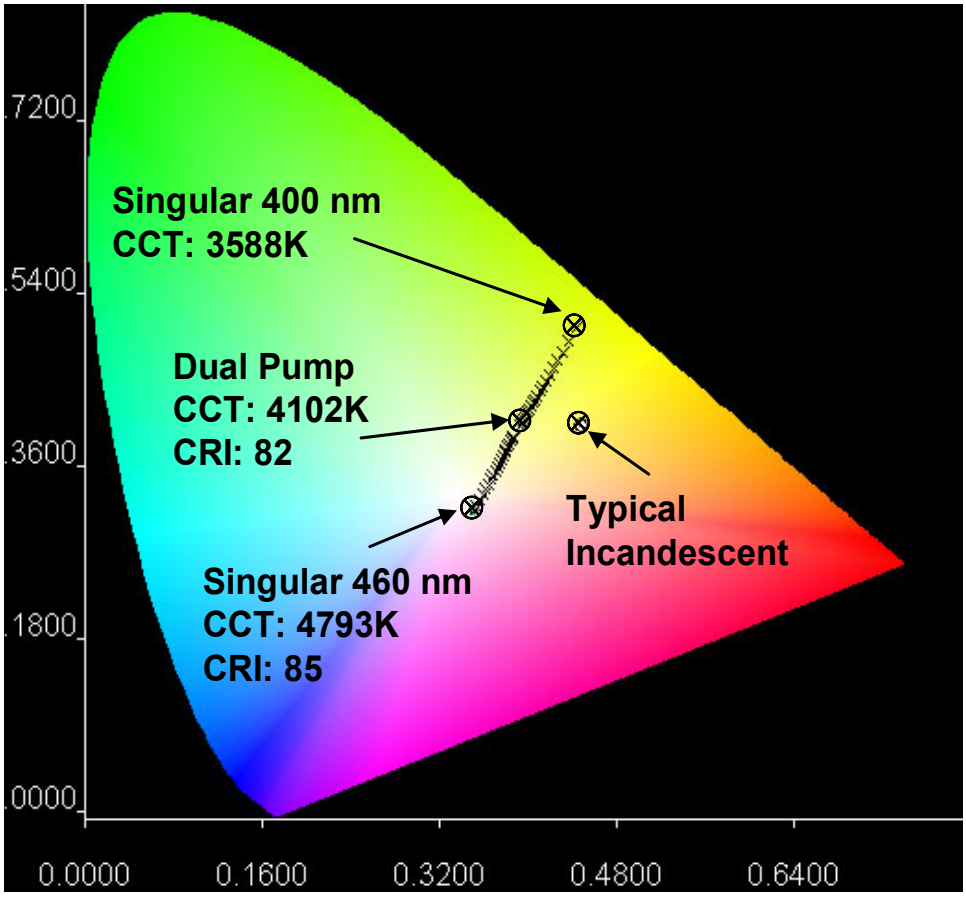

Figure 85: Plot of CIE coordinates for varied phosphorescence spectra

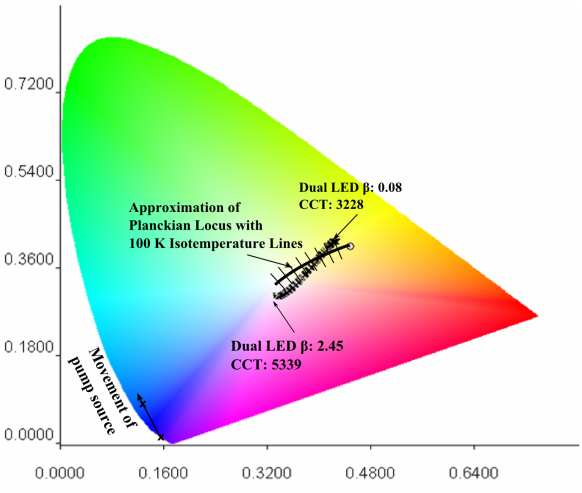

Figure 86: CIE daigram with range of second generation phosphor mix

5.3 Second Generation Phosphor Test Bed

A wider range of phosphors were combined to create a mixture that would have CIE co-ordinates closer to the Planckian Locus. In addition to the phosphors used in the first generation test bed, YAG:Ce and an orange emitting phosphor were used to enhance the spectral power distribution of the source. Another stipulation to the second generation phosphor test bed was that it work with the second generation dual LEDs described in Chapter 6. These devices do not have a the dynamic range that is achievable with two discrete devices, which can have β ranging from 0 to ∞. YAG responds very well to pumping with 460-470 nm light, but not to ~400 nm light. On the other hand, the orange phosphor used responded equally well to pumping from 400-480 nm light. The range of chromaticity achievable with the second generation phosphor combination is shown in Figure 86. This was achieved using the dual LED described in Chapter 6. When β of the source is 0.08, the spectrum has a CCT of 3228K, and is very similar to an incandescent light bulb. As β is increased by increasing current density, the spectrum shifts due to added long wavelength content from the LED as well as additional long wavelength components from the red and

orange phosphors. The high CCT end also shows a slight upward curve that is caused by saturation of the long wavelength phosphors and more LED light passing through. Shift in the CIE coordinates for the standalone pump source is shown on the bottom left corner of Figure 86. The fact that the direction of shift for the final device and standalone pump differs illustrates that the phosphor emission significantly contributes to the final SPD.

5.4 Conclusion of Phosphor Testing

The results shown here describe successful use of phosphor combinations with a dual LED to create a dynamic spectrum light source. The first generation phosphor test bed was pumped with a source in which β ranged from 0 to ∞. However, the second generation phosphor test bed had a constraint that it must work with a β range of 0.08 to 2.5. A suitable set of phosphors was used to create a source of which the CCT can be varied from 3228 K to 5339 K by increasing the drive current used in the LED.

CHAPTER VI

DUAL LEDS

6.1 First Generation Two Terminal LED Structures

LED structures with multiple quantum well regions designed to emit at different wavelengths have been grown. It has been observed that the emission mechanism for each of these MQW regions is the same as that seen in a single MQW region LED.

Dual MQW region LEDs, Figure 87, for efficient pumping of multiple phosphors have been grown by MOCVD, for use in broadband, white solid state light sources. Blue (460 nm) and Violet/UV (∼400-420 nm) emitting MQW regions were incorporated into a single device and show recombination mechanisms similar to single MQW region devices. The introduction of a spacing region successfully separated the electroluminescent emissions, and two distinct emission peaks were observed. A large factor in the efficient radiative recombination in these devices is the localization of carriers by indium compositional fluctuations in the InGaN quantum wells. Photoluminescence measurements were carried out to determine the physical mechanism behind light emission in these devices. Optical recombination in low-dimensional InGaN quantum structures strongly depends on the localization of carriers in quantum dot-like structures[11, 63, 61, 49]. Inhomogeneities in the indium concentration on the nm-scale provide potential fluctuations in the band gap, and the carriers are trapped in islands that may provide 3D-quantisation up to elevated temperatures[61]. An increased overlap of hole and electron wave functions is induced by the localization of carriers in the nanoscale islands. The average localization energies were determined by an Arrhenius plot of the luminescence intensity following the approach suggested by Adelmann et al[2]. The two activation processes are necessary to describe the data in both low and high temperature regimes.

All the LEDs in this work consisted of InGaN/GaN quantum wells in the active region. The emission wavelength was controlled by changing the growth temperature of the wells,

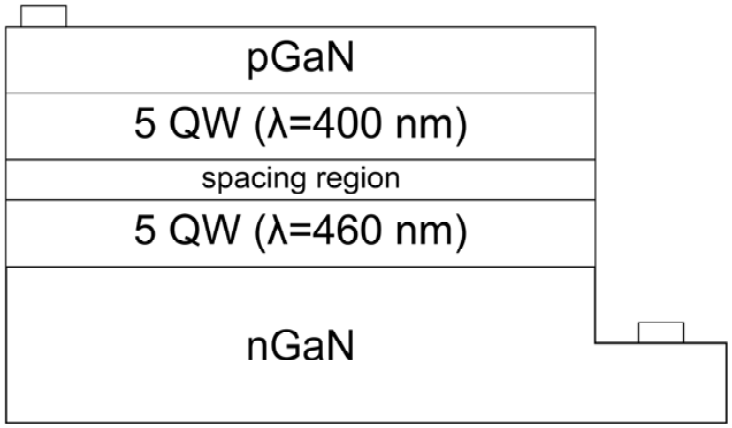

Figure 87: Layer schematic of 1^{st} generation Dual LED

which affected the growth rate and the indium incorporation. The barrier was grown in two stages; the first stage was grown without hydrogen and the second stage was grown with hydrogen and at a higher temperature and rate than the first stage. Multiple growths were completed to optimize the growth rate of the well and the two stage barrier.

A series of systematic growth runs were completed at various temperatures to better understand the effects of temperature on the indium incorporation in the quantum wells. Active regions were developed specifically for 460 and 400-420 nm emission. X-ray diffraction and structure simulation were used to study changes in the indium concentration with respect to the growth temperature and the thickness of the wells against the emitted and PL wavelength.

Next, a series of devices containing a 460 and a 400-420 nm set of multi-quantum well regions, a dual MQW region structure, separated by an undoped spacing region was grown as shown schematically in Figure 87. The dual MQW region emitter incorporated the optimized MQW growth conditions for the respective emission wavelengths. The device structure development focused on the 3 layers shown below:

1. First set of MQW (460 nm)
2. Spacing layer between the two MQWs
3. Second set of MQW (400-420 nm)

The 460 nm MQW was placed at the bottom so that it does not reabsorb the emission from the 400-420 nm MQW. A spacing layer was introduced between the two MQWs to mitigate interaction. The two respective MQWs were split into three growth stages: the quantum well and a two stage barrier. As discussed above, temperature was used to vary the indium incorporation into the well to control the desired emission wavelengths. During device optimization it was determined that varying well and barrier thickness and different growth temperatures were the best approach for the two sets of MQWs.

Thin and thick undoped GaN, n-type GaN and low aluminum concentration GaN layers were studied for the spacing layer at both low (below 800°C) and high (above 900°C) temperature growths. In addition, different precursors for gallium (TMGa and TEGa) were evaluated to optimize the interface layer.

Text Box: Figure 1.9: Temperature Dependent PL data for blue emitter. Inset shows peak position and intensity as a function of the temperature facilitating the determination of activation energies of 4 meV and 44 meV.

A bright quantum well emission dominated the PL of all samples. Temperature dependent PL data for a blue emitter is shown in Figure 88. Inset shows peak position and intensity as a function of the temperature facilitating the determination of activation energies of 4 meV and 44 meV. Similar results were obtained for the UV emitter (not shown here). A significant S-shape behavior of peak energy, which indicates the presence of QD-like potential fluctuations, is revealed by temperature dependent PL measurements for low excitation energies (Figure 88). Evaluation of MQW emission determines the activation energies to be $E_{act}(1) = 4$ meV and $E_{act}(2) = 44$ meV following the approach suggested by Adelmann et al.[2], Equation 53.

$$I = C\left[1 + Ae^{\frac{-E_1}{kT}} + Be^{-E_2}kT\right] - 1 \tag{53}$$

where, k is the Boltzmann factor, and A and B are scaling factors. The scaling factor of the latter process is more than 200 times larger than the first. Interface roughness and/or one monolayer fluctuations of the QW thickness typically provide localization centers with localization energies below 5 meV. Therefore, the smaller energy can be attributed

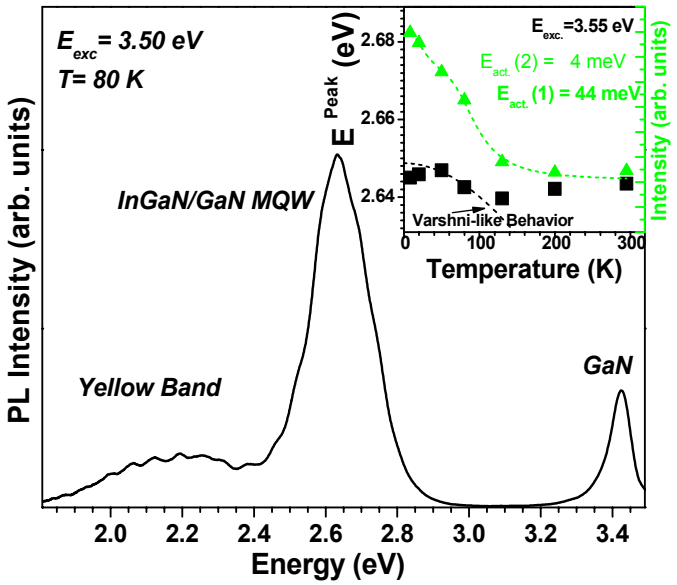

Figure 88: Temperature Dependent PL for blue emitter

to imperfections of the interfaces in the MQW. A more thermally stable localization is indicated by the second E_{act} = 44 meV. It is assigned to the localization of carriers in nanoscale islands caused by fluctuations in the indium concentration. Site selective PL spectroscopy was also performed on the dual MQW device, shown in Figure 89a. For each peak a mobility edge can be determined: 2.94 for the blue emission and 3.08 for the UV emission. This indicates the existence of isolated localization sites on the low-energy side of the mobility edges, confirming the radiative recombination in the device is generated in zero dimensional centers. Hence, the dual MQW devices show the same emission mechanism as detected for each single MQW devices.

Bright electroluminescence was also observed from the devices. The EL data for dual MQW region device is shown in Figure 90. Two distinct peaks are observed in the dual MQW region device, showing separate luminescence from each of the MQWs. Similar results are observed for devices with 400 nm and 460 nm peaks.

The enabling light emission mechanism in GaN-based LEDs with a single MQW region, namely carrier localization[45], has been successfully employed in a device with dual MQW

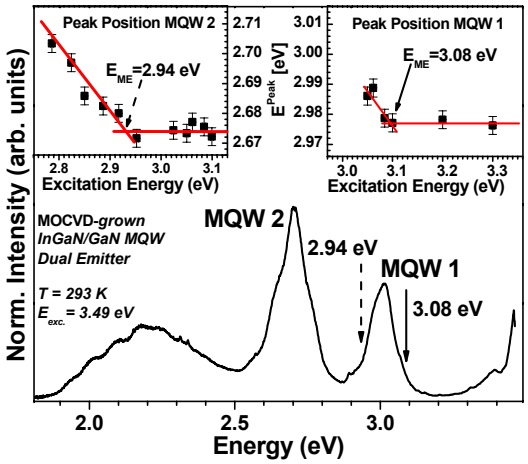

Figure 89: Site Selective PL for MQW device

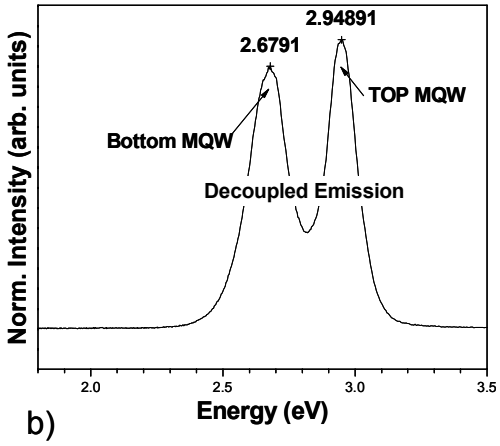

Figure 90: Electroluminescence from a dual LED

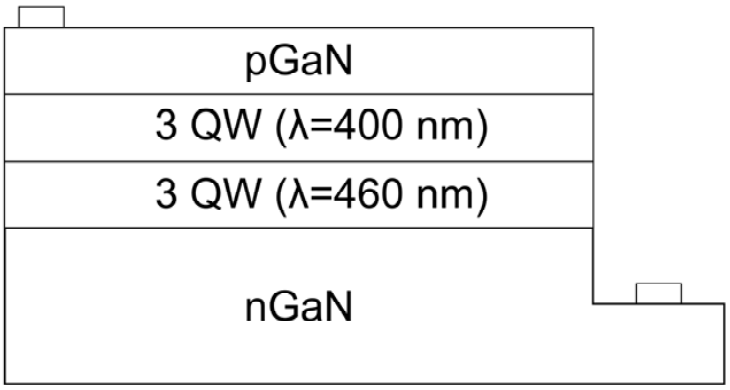

Figure 91: Layer schematic for 2^{nd} generation Dual LEDs

regions tailored to emit in the blue and near UV regions of the spectrum. This was important to preserve the same high brightness characteristics from standard GaN LEDs to the new device. Temperature and excitation energy dependent PL measurements confirmed the existence of carrier localization first in the single MQW region devices and then in the dual MQW region devices.

Bright emission derived from the carrier localization is also seen in EL (Figure 90). These devices show that dual wavelength emission is possible from the same device.

6.2 Second Generation Two Terminal Dual Wavelength LEDs

The first generation of two terminal dual wavelength had an emission spectrum with two distinct peaks which could be used to efficiently couple into multiple phosphors of different excitation spectra. However, dynamic control of the relative intensities of the two peaks was limited in these devices. A second generation of devices were designed to increase the ability to control the relative intensity of the two peaks and simplify the structure. A series of experiments were performed to determine the behavior of these devices. A basic schematic of the device layer structure is shown in Figure 91. The samples were grown in the highly modified commercial MOCVD reactor used for the rest of the work. The active region consisted of six quantum wells with three designed to emit at 400 nm and three designed to emit at 460 nm. The first three grown were designed to emit at 400 nm and will be referred to as QWs 1-3, while the last three grown were designed to emit at 460 nm and

are referred to as QWs 4-6. Below the active region is an n-type GaN region with carrier concentration of $\sim 10^{18} cm^{-3}$ electrons. Above the active region a p-type GaN region with hole concentration $\sim 10^{17} cm^{-3}$. The n and p-type regions used in these device are typical of common LED structures. In this study the most important metric was the relative intensity of the two emission peaks. β is defined as the ratio of the long wavelength intensity to the short wavelength intensity. In the case of these samples the long wavelength quantum wells are positioned nearer the n-type GaN layer and the short wavelength quantum wells are positioned near the p-type gallium nitride. In effect, β is a measure of the amount of electron hole pairs recombining in the long wavelength quantum wells as compared to the short wavelength quantum wells, which is dependent on the current injection into both of those regions. β will be used throughout this section to denote this ration in the text and figures.

6.2.1 Dual LED Results

First a sample with no doping in any of the barriers was grown, fabricated and tested. The electroluminescent spectra at varied drive current is shown in Figure 92. Figure 92 shows that at low currents the long wavelength emission is greater than the short wavelength emission. As drive current is increased the relative intensity of the short wavelength emission is increased to a point where the effect saturates as shown in Figure 93. The maximum β for this device is 1.47 and the minimum is 0.89. Next the barrier between QWs 3 and 4 was doped with Si to study the affect it has on the minimum and maximum β. Three samples with different doping levels in the barrier between QWs 3 and 4 were grown, fabricated and tested. The first sample, had a carrier concentration of $\sim 6 \times 10^{18} cm^{-3}$ electrons. EL spectra in Figure 94 show that at low currents the short wavelength dominates with a β $\sim$0.1. It is not until very high current densities (220 $\frac{A}{cm^2}$) that β begins to change. The maximum β reached before the device is destroyed by high current is $\sim$1.1, as shown in Figure 95 where β is plotted against current density. Another sample was grown with twice the Si doping in the barrier ($1.2 \times 10^{19} cm^{-3}$), however, no change in β was observed for current densities that the device could sustain. A third sample with half the Si doping

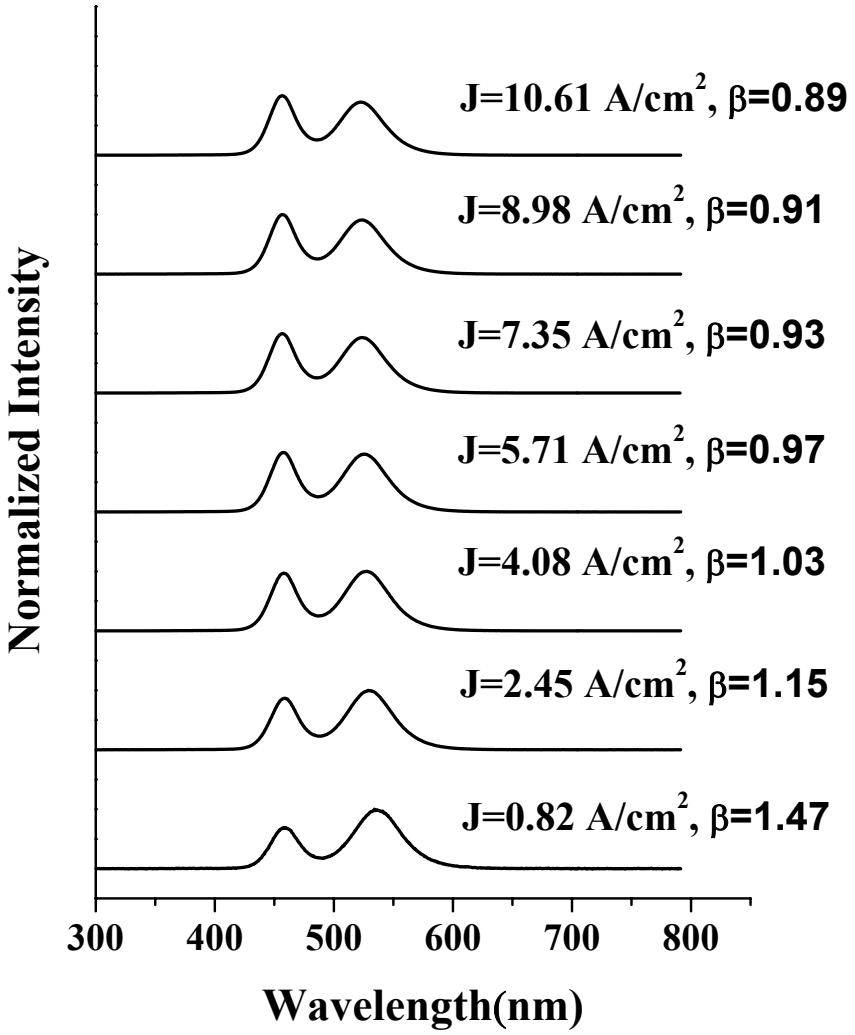

Figure 92: Normalized EL spectra of Dual LED with undoped barriers

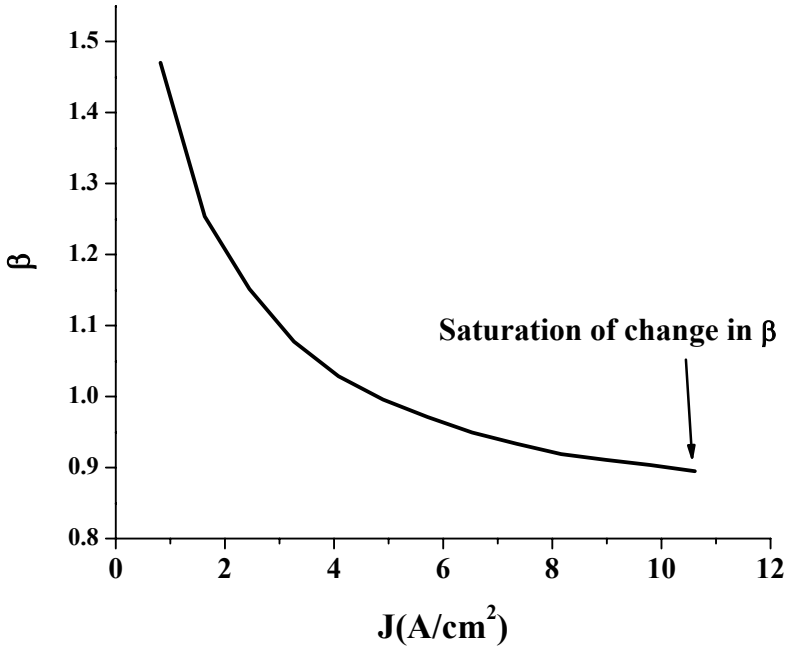

Figure 93: β vs. J for Dual LED with undoped barriers

Table 6: Results of Second Generation Dual LED growths and testing

Doping (cm^{-3})	**Min** β	**Max** β	β=1
None	0.89	1.47	$4\frac{A}{cm^2}$
3×10^{18}	0.08	2.5	$220\frac{A}{cm^2}$
6×10^{18}	0.08	1.1	$305\frac{A}{cm^2}$
1.2×10^{19}	NA	NA	NA

$(3 \times 10^{18} cm^{-3})$ was also grown. The effect of drive current on β was much greater and started to show at current densities $\sim 100\frac{A}{cm^2}$, as seen in Figure 96. The maximum β attainable for this device was ~2.5, for which the EL spectrum is shown in Figure 97. The results for these device is tabulated in Table 6.

6.2.2 Discussion of Dual LED

Doping of the barrier between QWs 3 and 4 with Si achieves significant control over the β by varying drive current. A model to explain this behavior considers two barriers to current injection in the different QW regions. A band diagram for the QW region of a device with doping in the barrier between QWs 3 and 4 is shown in Figure 98.

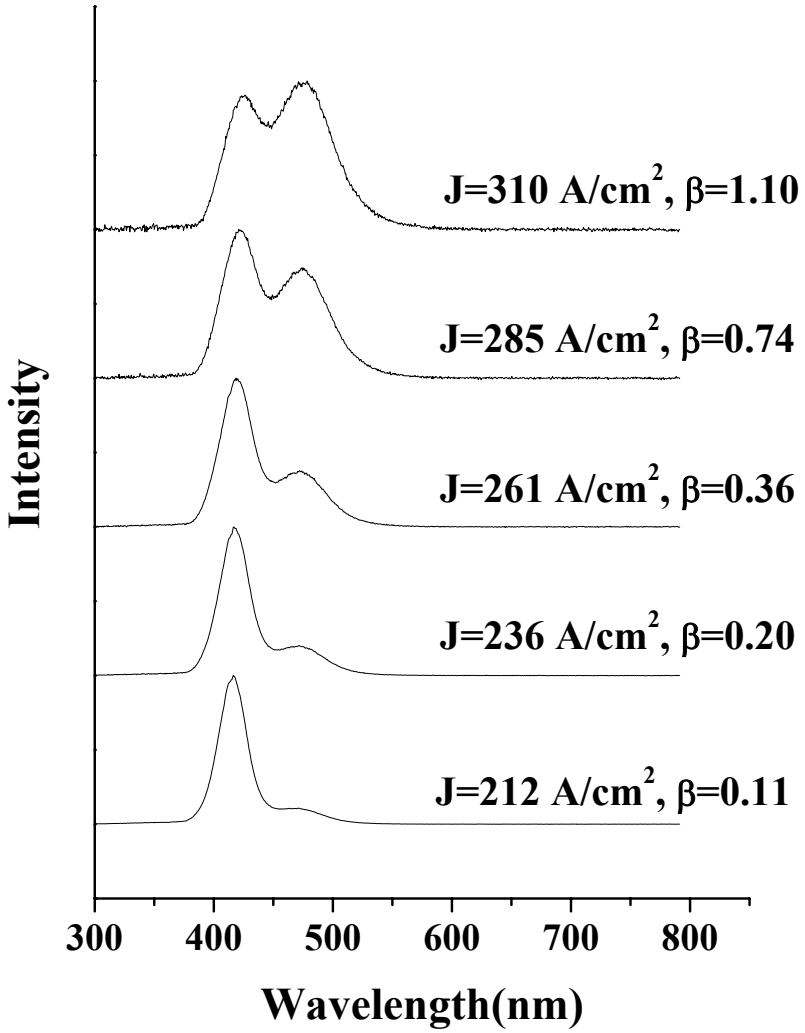

Figure 94: Normalized EL Spectra for $6 \times 10^{18} cm^{-3}$ doped barrier

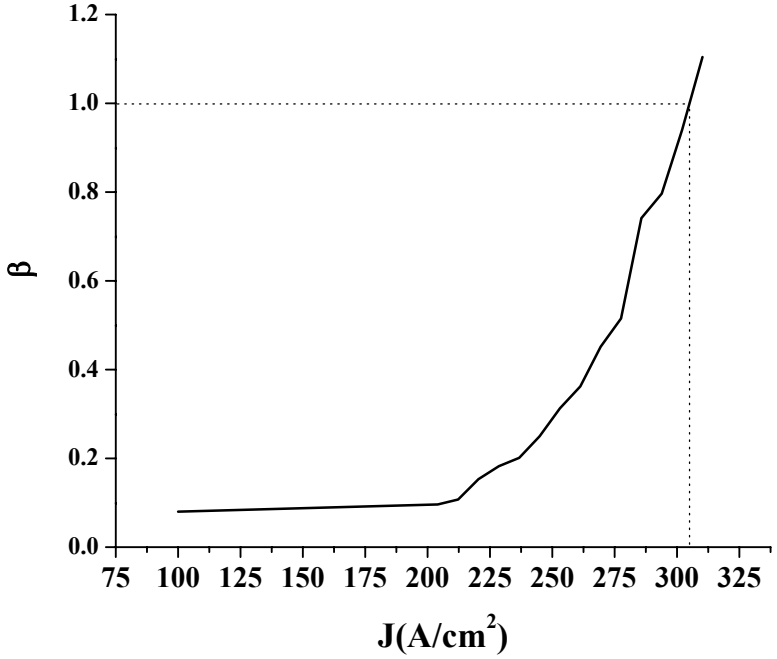

Figure 95: β vs J for $6 \times 10^{18} cm^{-3}$ doped barrier

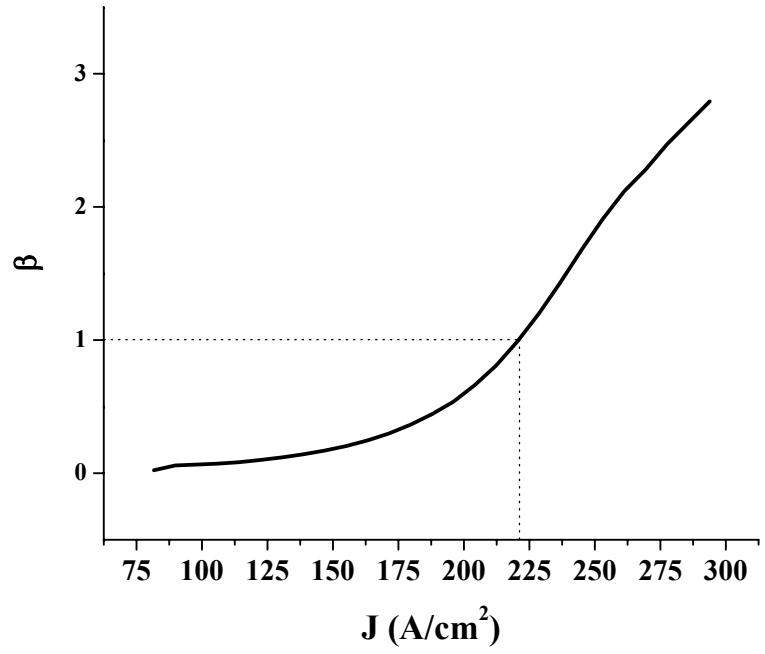

Figure 96: β vs J for $3 \times 10^{18} cm^{-3}$ doped barrier

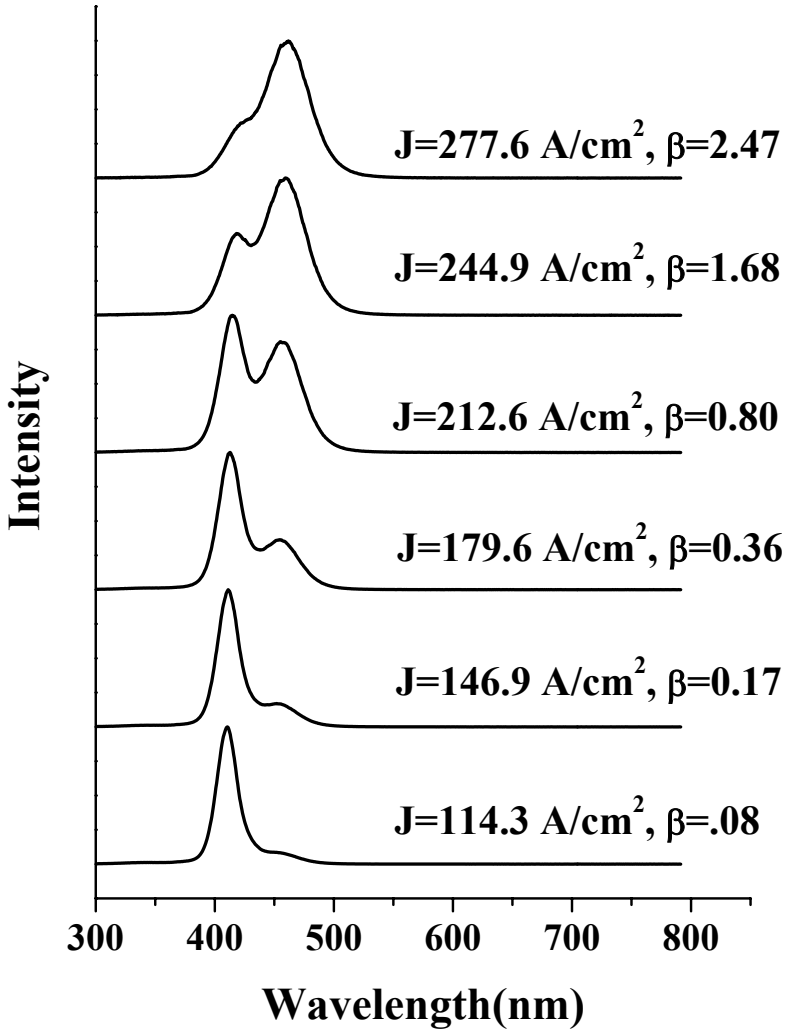

Figure 97: Normalized EL Spectra for $3 \times 10^{18} cm^{-3}$ doped barrier

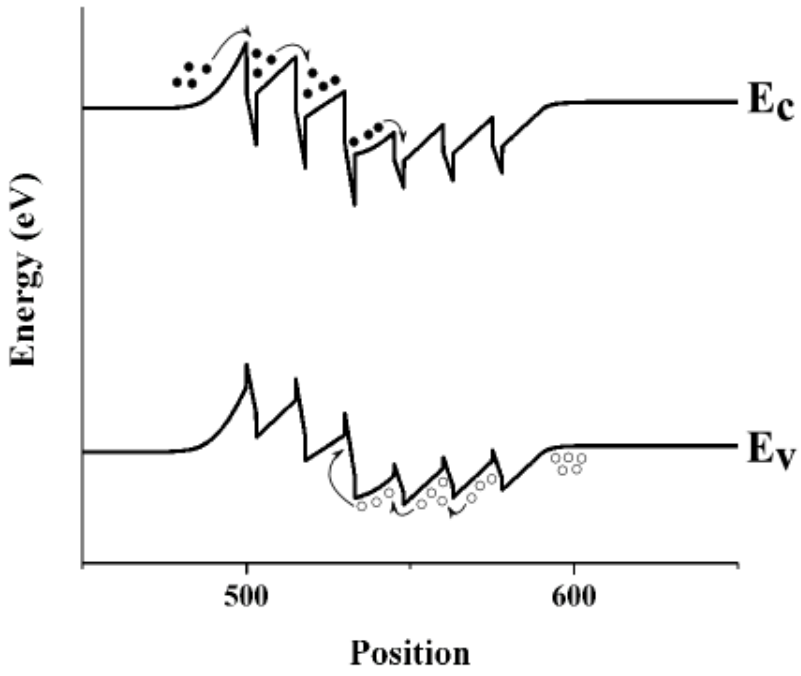

Figure 98: Band Diagram of QW region for a Dual LED with doped a doped barrier

In Figure 98 the n-type region lies to the left of the QWs and the p-type region is to the right. The relatively high In concentration in the Qws 1-3 leads to electron trapping and blocking, making it more difficult for electrons to travel to QWs 4-6. This effect is best observed in a dual LED with no doping where the QWs 4-6 are preferentially excited at low currents. In the case of no doping holes are more free to move to QWs 1-3 than electrons are to move to QWs 4-6 at low currents. As current is increased the electrons fill higher energy states and are able to travel to QWs 4-6. At this point the mobility of the carrier influences β. QWs 4-6 are more preferentially pumped because holes have lower mobilities and do not travel as far as the electrons, thus recombination is more likely in QWs 4-6. On the other hand, the doping of the barrier between QWs 3 and 4 creates a barrier to hole transport to the QWs 1-3. In the case of the doped barrier the hole blocking washes out the effect of electron blocking at low currents. The holes are trapped in QWs 4-6 until current is high enough to promote some holes over the doped barrier and into QWs 1-3. At this point the electron trapping effect influences β recombination occurs in QWs 1-3. A

mathematical model describing β as a function of drive current is in Section 3.3.3.2

CHAPTER VII

BROADBAND CIRCADIAN LIGHT SOURCE

7.1 Introduction

Bringing daylight indoors has been the major goal of the lighting industry for more than a century. While there have been some advances in this area, most noticeably the use of fiber optics, there have been no major revolutions. As the lighting industry has matured, lighting designers have been able to consider effects beyond visual to the psychological, such as the effects of architectural downing to highlight features of a building facade. However, as the lighting industry matures further, designers can take another step and examine the physiological aspects of lighting of people within the environment.

Solid State Lighting (SSL), that using light emitting diodes (LEDs) as the illumination source, is becoming a practical future for lighting as LEDs continue to improve in efficiency, luminous output, cost. LEDs can be smaller, more efficient, more robust, longer lived, cooler, and more easily controlled than conventional lamps. Yet, for solid state lighting to provide a competitive advantage over conventional lighting it must provide new innovations rather than being a more cost effective replacement. The controllability provided by solid state lighting sources lends itself to the development of new sources for general illumination.

Recent biological research has investigated the relationship between human internal clocks, the circadian rhythm, and light. Studies show that certain circadian rhythms can be entrained with light. Thus, disorders such as jet lag, shift work sleep disturbance, age-related insomnia, advanced- and delayed-sleep phase syndromes, and SAD (seasonal affective disorder) can be addressed. However, many uncertainties still exist in this field. While melatonin levels in the blood are generally accepted as the true indicator of a response, the photoreceptor for the circadian system is still in debate. More work is required in this field which proper tools can greatly facilitate.

In light of this, a circadian light source that modulates its Correlated Color Temperature

(CCT) and total intensity to mimic daylight of the earth during the normal day has been designed. The ingenuity of this device is the manner in which it modulates CCT. This is achieved by varying the intensity of blue light in the visible power spectrum via LEDs. For example, when blue light is combined with white light, the CIE coordinates of the source shift closer to the blue edge, similar to daylight's daily movement along the Planckian Locus. The curve can be approximated to a linear regression due to chromatic adjustment of the eye. Moreover, blue light at 460-470nm has been shown to elicit the greatest circadian response[6]. Due to the spectral changes, this implies that lighting can have physiological effects for humans beyond the normal visual and psychological effects. The light source developed in this work can mimic the sun and most efficiently and comfortably tap into the human circadian system, by using this color variation.

7.2 Circadian Rhythms

Human biological systems are complex and not well understood with human eye being one of the most complex of these. Although, it is widely accepted that vision is primarily mediated through cells known as rods and cones contained in the eye. As research continues biologists have realized that there are functions of the eye other than vision[3]. There are cells in the eye that are believed to have the ability to reset certain biological systems when the correct amount of light is present.

A circadian rhythm is one with a cycle of about 24 hours. "Circa" means about and "dia" means day, giving: "about a day" or 24 hours. This internal clock is reset daily with light, which is received by photoreceptors in the body, Figure 99b. A basic flow diagram is illustrated in Figure 99a. It illustrates the path of our circadian system the results in our propensity to sleep or wake. Circadian rhythms are common throughout different life forms from bacteria to humans. Core body temperature, sleep schedules, and other physiological behaviors, are regulated by this clock. This internal clock is reset daily with light, which is received by photoreceptors in the body. The action spectrum in Figure 100 denoted as melatonin response gives evidence to the importance of spectral content of the source, because it represents the response of the human circadian system to varying colors of light.

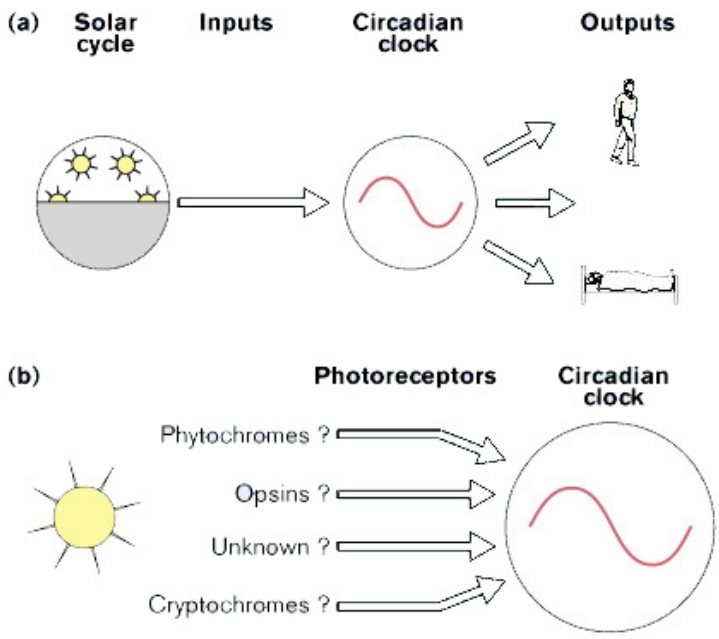

Figure 99: Entrainment (a) and Mechanisms (b) of the Circadian Clock

An important note is the peak around 464nm. The human circadian clock has an average free running time of 24.22 hours. Free-running is defined as the average cycle time in a no light environment. In humans the phase of circadian cycle can be monitored by salivary or blood melatonin levels, or core body temperature[13]. These rise and fall of these functions occurs at different times of the day and depends on light as shown in Figure 101. Melatonin is the principle hormone secreted by the pineal gland and is a derivative of tryptophan. High melatonin levels have been shown to cause sleepiness[16] in humans, therefore partly regulating the sleep/wake cycle. Secretion and synthesis are inhibited by light, and so induced by darkness. However, the exact biological path for these cues is still unknown though continuing research is examining the different steps. Light has been shown to be one environmental cue at the beginning and melatonin is recognized as the endpoint of a biological chain[16]. Currently, a major research thrust in this field has been to identify the single or set of circadian photoreceptors. Knowing and understanding the cells that react to light for the circadian system would allow biologists to better understand the way light interacts with human systems. It is evident from Figure 100 that the primary visual receptors are not responsible for light entrainment of the circadian system. The shaded curve

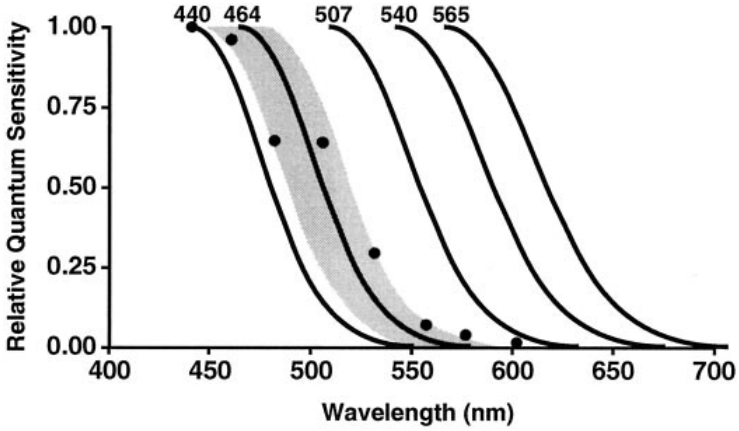

Figure 100: Action Spectrum of Vision and Melatonin Suppression in Humans

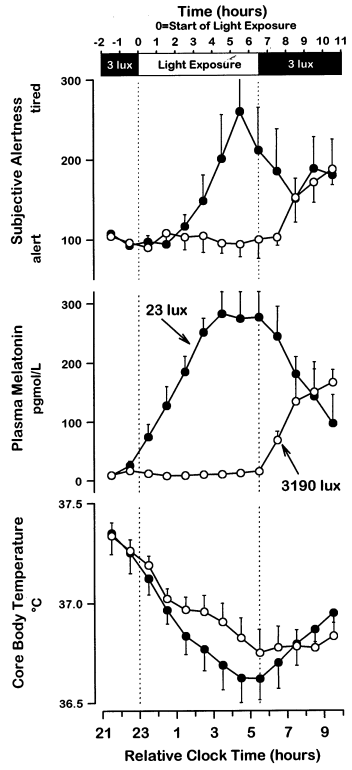

Figure 101: Phase Shift of a Circadian Rhythm

represents that action spectrum where the other curves are corresponding to the responses of rods and cones[6]. Other research has at least concluded that cones are not responsible for entrainment, but acknowledges that these type of tests "do not eliminate more complex models based on unusual combinations of known photoreceptors"[55]. Moreover, one study showed that mice without rods or cones still had a circadian reaction to light[20].

As research has progressed, several candidates for the primary photoreceptor have been proposed. Recently, melanopsin, an opsin located in the human eye has been given much attention as the most likely candidate. With a peak response at 480 nm, it is the closest match to the circadian system. The slight offset from the 464 of the melatonin inhibition suggests that it might not be the only player in its role as a circadian receptor. Also, the entire pathway of light entrainment is still unclear to researchers, and it is possible that the cell serves some other purpose[6]. Accordingly much of this field seems to be not well understood.

The current state-of-the-art in Circadian Light Therapy devices consists of bright white light boxes. These are used to irradiate a certain amount of light onto a subject for a specified period of time. Until recently it was widely believed that brightness and exposure were the only important parameters in the light therapy. The evidence presented here shows that wavelength of light plays some role in circadian entrainment. The color does matter because of the way cells work, having peak responses at certain wavelengths. Solid state lighting has the ability to efficiently interact with the human circadian system on this premise.

7.3 Circadian Light Source

Solid state lighting must employ new features offered by LEDs in coordination with the current understanding of light and how it interacts with the human body. Current lamp technologies are limited in their abilities to do this because they are designed for one function and typically only the intensity can be controlled. However, the circadian source must be more complex to offer these capabilities. A basic schematic is shown in Figure 102. The control source is used to modulate the light source and the power module provides the

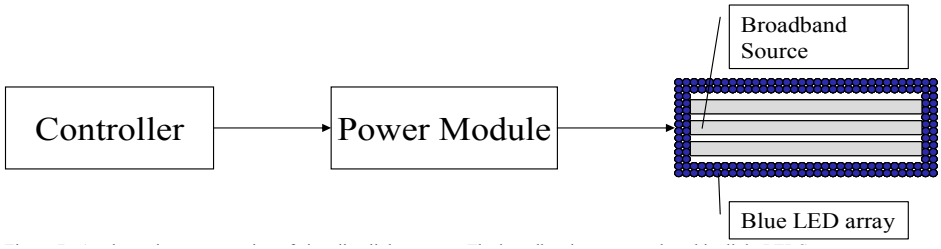

Figure 102: Schematic of a Circadian Light Source

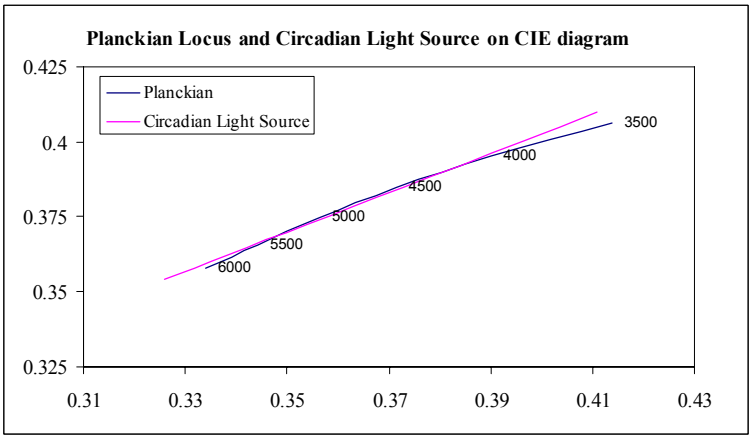

Figure 103: Plot varied CCT for circadian light source

necessary current to drive the LEDs in the light module. Modulation is achieved through the use of a simple microcontroller or more advanced computer, and a pulse width modulation scheme designed to increase or decrease the intensity of an individual or bank of LEDs on a periodic cycle close to that of a day. This is possible because of near instant turn-on time of LEDs. The circadian source developed in this work can be used to produce variations with time periods of 5 seconds to 48 hours but will be normally be used with time periods of 20-28 hours depending the application.

The spectrum and thus CCT of the device can be controlled by varying the intensity of blue and green high brightness LEDs incorporated in the device. The correct color mix and modulation, leads to a linear approximation of the Planckian locus as shown in Figure 103. This is data taken using a spectrometer from an array of LEDs where the intensities of the blue and green LEDs were varied. The Circadian Light Source works by modulating its CCT in a cycle that mimics the normal day. A more sophisticated device is being developed that can accurately follow the Planckian by modulating Red, Green, and Blue (or other

color) LEDs in coordination with a broadband source in the proper sequence. Ultimately the source will be able to produce a very wide range of colors from the edge of the color gamut to anything on the Planckian; although for general illumination will typically be limited to the Planckian.

The lamp choice must also consider CRI. Using multi-chip LEDs may or may not lead to a suitable CRI of 85 or above, which is the definition of a deluxe lamp for lighting applications. It is possible to achieve high CRI by using three (3) LEDs with the correct emission wavelength[66] and a suitable control system. Another feature that is under consideration is a feedback system to monitor, in real time, the CIE coordinates of the spectral output. This would consist of a sensor to ensure that changing properties in the LEDs do not degrade the quality of the light. Additional cost for the source is the main concern with a feedback system.

Another consideration for a proper circadian source is brightness. For light to elicit a circadian response there is a minimum irradiance required. These levels have been determined for white light[9]. However, there has been no work found that studies emission with wavelength $\sim$460nm in this way. There has also been no work found that examines the effects of a changing source similar to the natural daylight. The circadian light source can be used for many different studies in this area to determine an optimal source for human circadian responses.

The source described here has many possible applications. As mentioned, it would give researchers a new tool in understanding the human circadian system. The dynamics of this source introduce a new element for conducting studies in this area. One of the possible next steps in this project is to coordinate with a biological research group to develop new tools and better understand these processes by performing human factor studies using experience from engineering and biological sciences. Instead of using saturated blue light to cause a physiological change, the circadian source can be used as an illumination source providing increased comfort over a saturated blue source. The circadian source will prove to be versatile as a general illumination source, allowing for changes in CCT according to the designers needs. The dynamics allow it to change its characteristics depending on time of

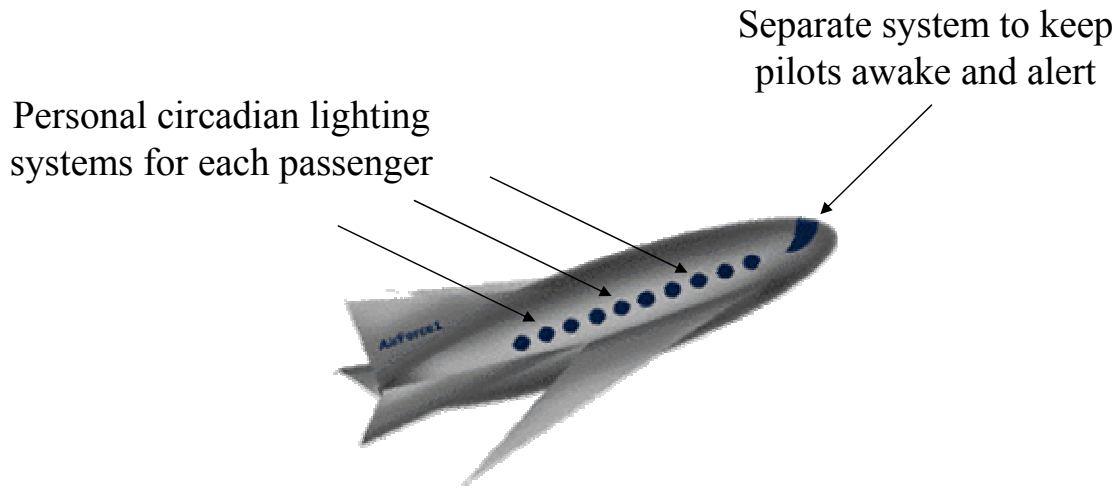

Figure 104: Example application for a circadian source

day, activity, number of people in the room, or other environmental concerns. Some of the physiological effects might be decreased in this case but visual and psychological effects will still play a major part.

One concept places these devices in airplanes much like reading lights, as which it may double Figure 104. It could be used to mitigate effects of jet lag. Each traveler would have a personal circadian light system for their specific schedule. Depending on the length or purpose of their stay the source could help them adapt accordingly. Another set of sources in the cockpit could help to keep the pilots more alert especially during transcontinental flights. This is an example of the innovative incorporation solid state lighting in an environment that provides new functionality.

7.4 Conclusion

Solid state lighting offers new features for lighting engineers and designers; one of which is controllability. For the success of solid state lighting, new sources based on that technology must take advantage of these features with new ideas about lighting. This source developed here uses controllability to add functionality to a general illumination device.

A circadian rhythm is one that has a period of about a day. Researchers have shown that these rhythms can be reset in humans by light irradiated on the eyes. Further research

has shown that an action spectrum for this type of response exists indicating that certain wavelengths of light have more effect than others. The action spectrum for a circadian response has a peak around 464nm corresponding to this spectral region. Also, an increase in color temperature of a light source corresponds to an increase in the spectral power density in the blue light.

A circadian light source has been developed as a general illumination source that can mimic the changes in color temperature of daylight through the day. This type of source may more effectively affect physiological changes in a subject than typical bright white source currently in use, while still retaining comfort provided by white light as opposed to blue light. For this device to be effective, however, the light must be bright enough. While dosage levels have been determined for white light, no work has been found that determines them for colored light. Further research is required, in which a device like the circadian light source could be used to understand the role of differing wavelengths in the entrainment of human circadian rhythms. The circadian source has many possible applications. It can serve as a general illumination source and a circadian entrainment source, because it is a white light source that can increase its color temperature to more efficiently interact with the human circadian system.

CHAPTER VIII

DEVELOPMENT OF A LIGHT BOX FOR ENTRAINING CIRCADIAN RHYTHMS IN RATS

Retinal melatonin receptors respond to a narrow band of wavelengths by inhibiting the pineal gland's secretion of the hormone melatonin; for humans, this band is in the blue region of the spectrum. The eye is normally exposed to blue light during the day. As a result, melatonin is associated with ambient darkness, and it regulates sleep-wake cycles in animals. The circadian rhythm is disrupted in the absence of a 24-hour day-night cycle. For humans in such environments (e.g., astronauts, or those suffering from seasonal affective disorder), periodic exposure to intense blue light can successfully regulate wakefulness. High-intensity light-emitting diodes have predictable spectral profiles, with narrow peaks at wavelengths dictated by the desired application. Their sub-microsecond switching times allow pulse-width intensity modulation. These properties make them well-suited for stimulating melatonin receptors with reproducible intensities and wavelengths of light. This section covers the development of a small artificial environment based on solid-state lighting has been developed. The enclosure is to be used at the Morehouse School of Medicine to study the suppression of melatonin production and consequent circadian phase-shifting in rats.

8.1 First Generation Light Box

A box as shown Figure 105 was built to hold a single rat at a time and expose it to a pulse of blue or green light for a desired period of time. LEDs were mounted on a board as shown in Figure 106, which was attached to the top box and aimed at the bottom box. The intensity of the LED emission could be controlled by increasing or decreasing the drive current to the LEDs through the tuning of a potentiometer as shown in Figure 107 which is a circuit schematic for the light box. A switch was used to direct current to a bank of green or blue LEDs. Figures 108a and b are photographs of the light box with green LEDs and blue LED

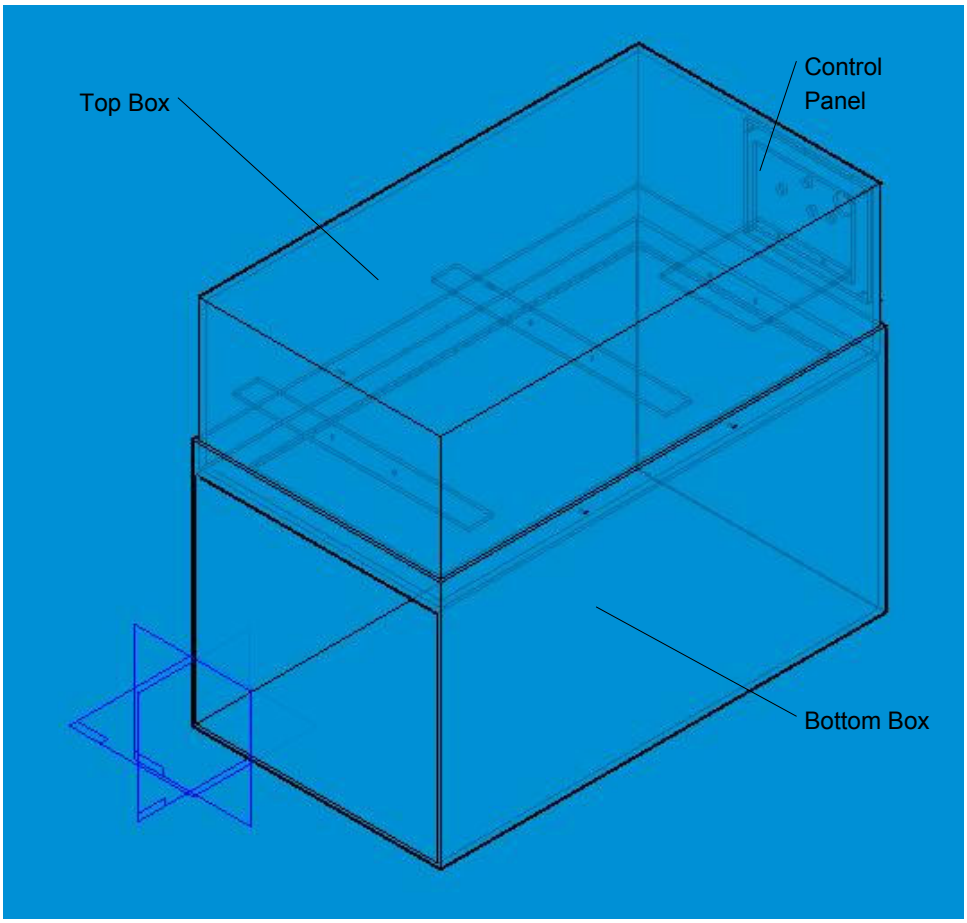

Figure 105: First Generation Light Box

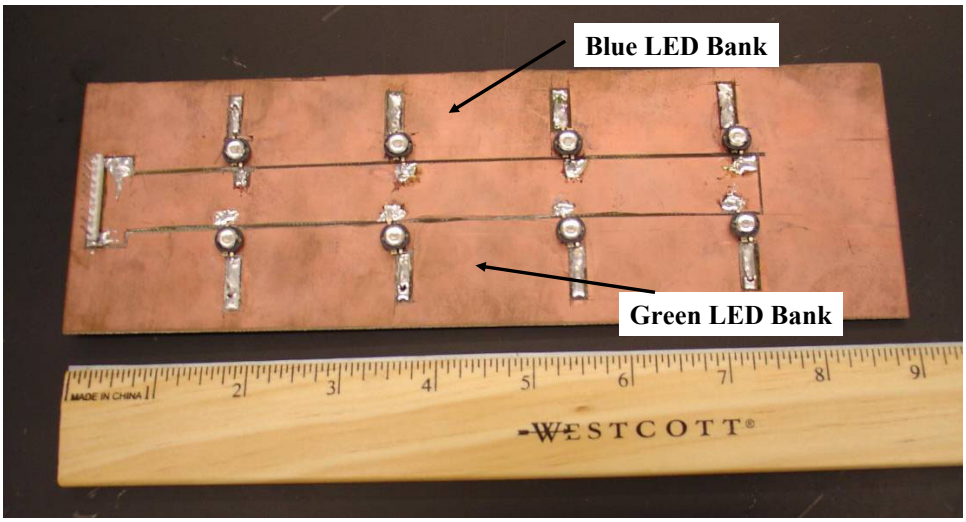

Figure 106: LED Board for first generation light box

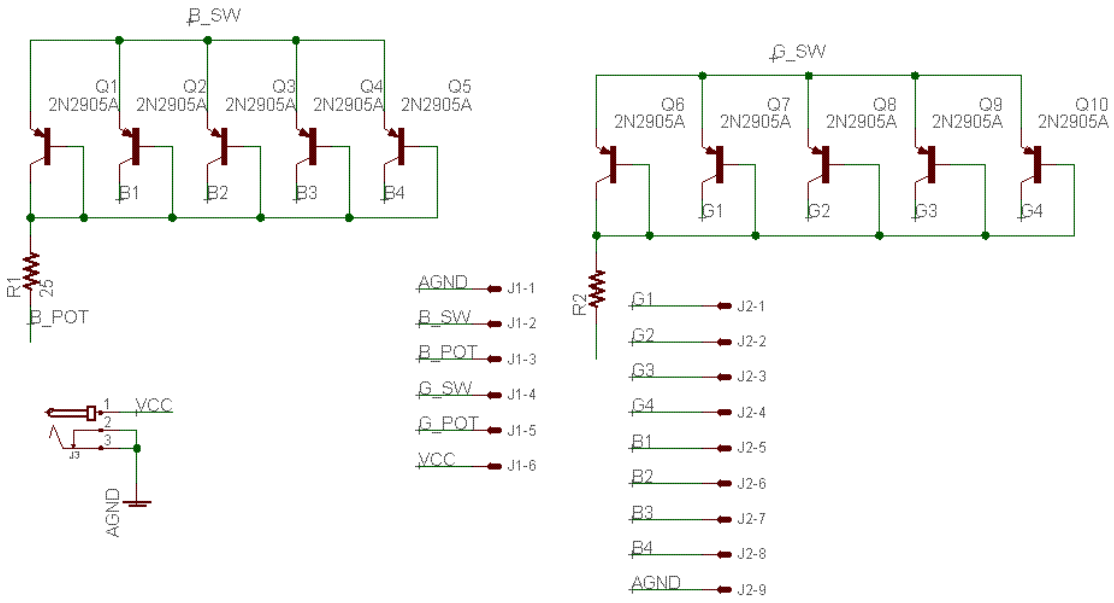

Figure 107: Circuit schematic for first generation light box

turned on respectively. The carrier in which the rats were kept is also seen inside the light box. During normal operation the rat and carrier would be inserted into the light box and the hinged door closed. The blue or green LEDs would then be turned on for a specific amount of time and the amount of circadian phase shift was measured for the rat. Results obtained using this box are shown in Figures 109a and b. These results were obtained using a 15 minute pulse of light with blue intensity of $0.1\frac{\mu W}{cm^2}$ and green intensity of $0.14\frac{\mu W}{cm^2}$. Green light is 30 % more intense than white and blue light, but does not phase-shift the locomotor activity rhythm(a) and does not suppress melatonin(b). This experiment shows the usefulness of blue light in phase-shifting circadian rhythms in rats.

8.2 Second Generation Light Box

Many SSL systems use pulse width modulation to control the intensity of an LED instead of current control in order to minimize current-dependent effects (e.g., intensity nonlinearity and chromatic shifting). The effects of such a scheme on circadian rhythm phase-shifting however is unknown. A second generation light box was to developed to investigate these attributes. This system consists of an embedded microcontroller that controls and monitors

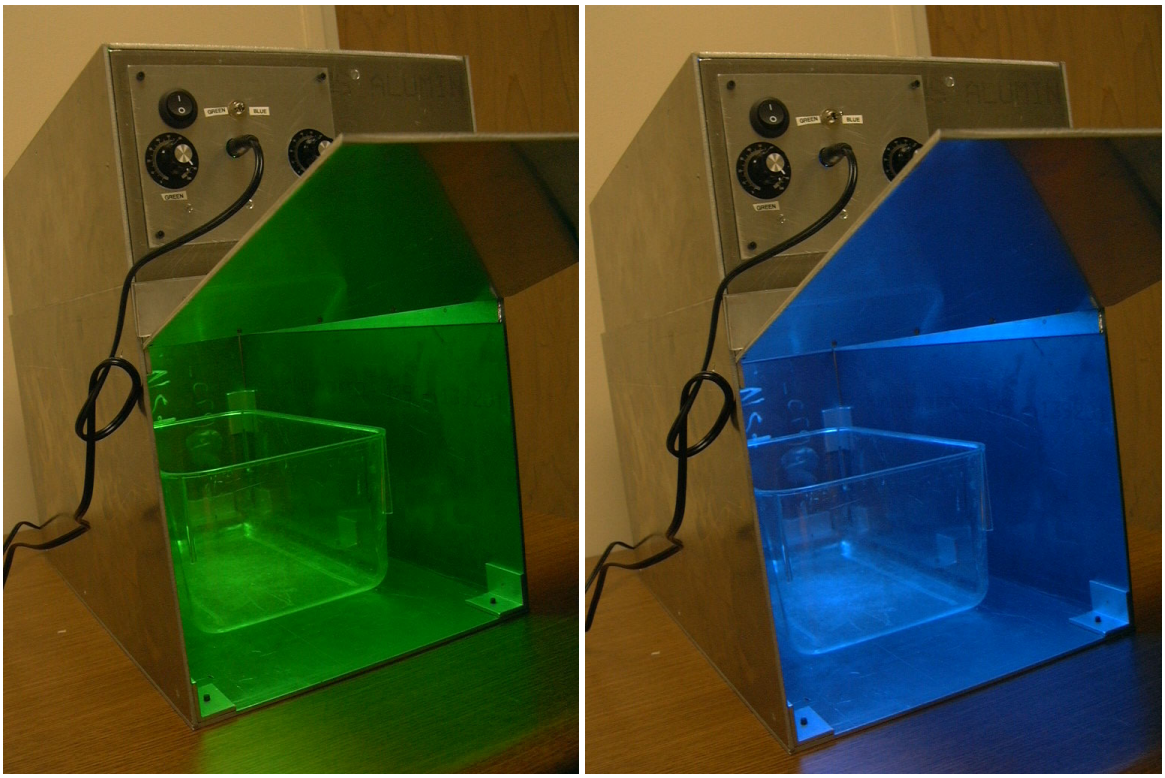

(a) (b)

Figure 108: Photographs of first generation light box

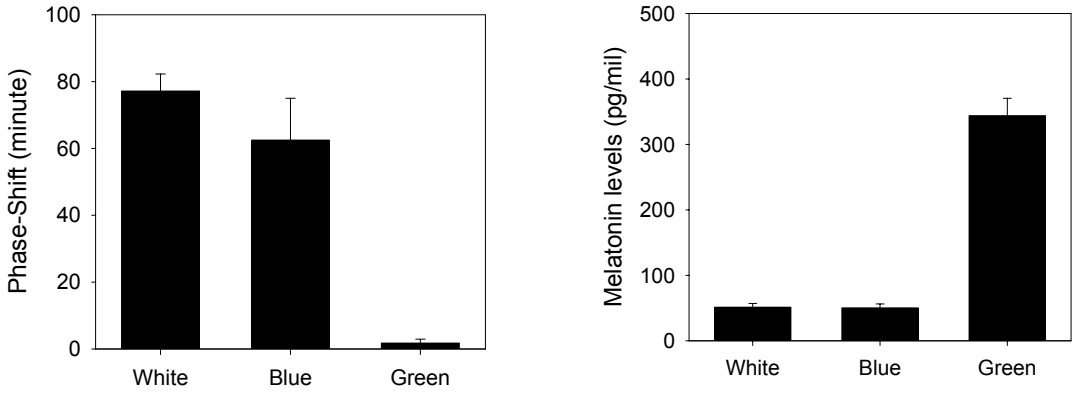

(a) (b)

Figure 109: Results obtained using the first generation light box

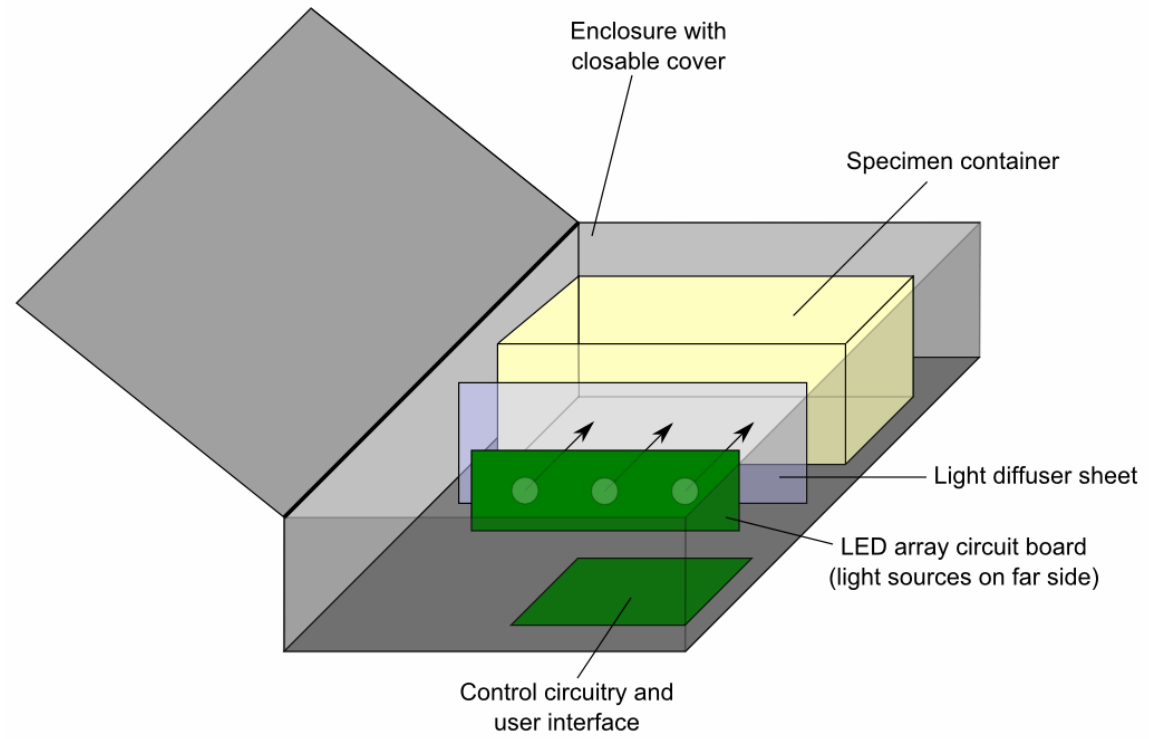

Figure 110: Schematic of the second generation light box

multiple LED arrays. Figure 110 shows an experimental prototype of this system. The box's user interface allows direct linear control over the LED supply current, the system also permits pulse-width modulation of the LED arrays. The system monitors the array heat sink temperatures and optionally applies a calibrated correction to the light output of the system, thereby compensating for the array's temperature-dependent behavior. The controller also stores user-defined diurnal lighting profiles, allowing the internal ambient environment to be varied automatically over time. All of these features are improvements to a similar previous enclosure. Figure 111is a high-level schematic view of the system. A secondary goal of this project is to evaluate the safety of high-energy light exposure. There is inconclusive evidence that exposure to sunlight - and especially to blue light - is a risk factor for age-related macular degeneration (AMD). Long-term exposure to short, high-intensity bursts of blue light may accelerate the onset of macular degeneration, relative to ordinary sunlight exposure. This system would benefit from the use of tunable LED arrays, such as phosphor-coated LEDs. For example, a tunable white LED source could

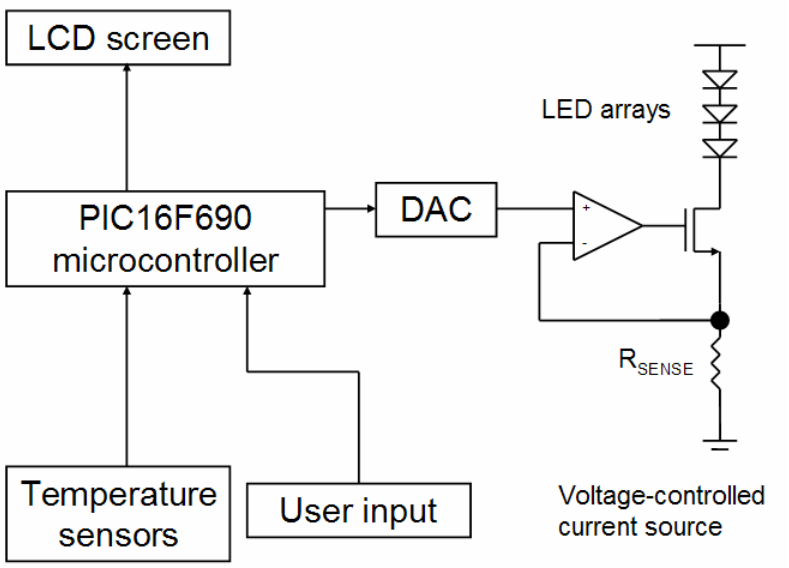

Figure 111: High level schematic of second generation light box

simulate a variety of ambient light scenarios, such as natural daylight, incandescent light, or fluorescent lighting. By simulating more realistic environments, the enclosure would be able to more accurately predict long-term biological effects. It would also be possible to evaluate the safety of phosphor-coated LEDs pumped by near-ultraviolet light.

CHAPTER IX

CONCLUSION

A novel solid state illumination source has been developed. A two terminal dual LED has been created with the ability to control the relative intensities of the two emission peaks by varying drive current. The key factor in the design of the two terminal LED is the barrier doping, by allowing greater control over β. A model for the operation of this device has been presented in which drive current effects the rates at which holes and electrons travel through the junction and cause a variation in β. The dependence of β on drive current can be modeled as an exponential function, where barrier doping density affects a scaling factor in the function. In addition, novel use of phosphor mixtures allows the creation of a broadband spectral power distribution that can be varied using a dual LED as an excitation source. Combinations of phosphors that have varied excitation spectra provide the ability to selectively excite different phosphors with the different LED emission peaks. First and second generations of the two terminal dual LED and the phosphor combination are discussed. The final source has the ability to mimic the light of a blackbody radiator over a range of 3200 K - 5300 K. The development of a three terminal dual LED as a pump source was prohibited by the need for a III-nitride tunnel junction, that proved unattainable in the scope of this work. However, several novel doping schemes were investigated toward this end. Finally, a circadian light source has also been developed that can affect physiological changes in humans, and a light box for entrainment of circadian rhythms in rats has been built. The two terminal dual LED created in this work is a novel simple solution to the issues of creating a tunnel junction. Fabrication of a two terminal dual LED is the same as that of a standard LED, requiring less complexity and introducing less error. Further optimization of the two terminal dual LED structure and doping profile could enable a greater range of β. This work demonstrates the operation of a novel LED structure with novel operational characteristics, as well as the novel use of phosphors in a spectrally dynamic light source.

The pursuit of novel devices and further investigation of current devices are required for the future of solid state lighting to be a success. The novel solid state general illumination source described here presents an example of added functionality to existing solid state lighting devices and opens the future of solid state lighting to new activities.

Ancillary material should be put in appendices, which appear just before the bibliography.

REFERENCES

[1] Adachi, S., *Physical properties of III-V semiconductor compounds : InP, InAs, GaAs, GaP, InGaAs, and InGaAsP*. New York: Wiley, 1992.

[2] Adelmann, C., Simon, J., Feuillet, G., Pelekanos, N. T., Daudin, B., and Fishman, G., "Self-assembled ingan quantum dots grown by molecular-beam epitaxy," *Applied Physics Letters*, vol. 76, no. 12, p. 1570, 2000.

[3] Barinaga, M., "CIRCADIAN CLOCK: How the Brain's Clock Gets Daily Enlightenment," *Science*, vol. 295, no. 5557, pp. 955–957, 2002.

[4] Benisty, R., Stanley, R., and Mayer, M., "Method of source terms for dipole emission modification in modes of arbitrary planar structures," *J. Opt. Soc. Am. A, Opt. Image Sci. Vis. (USA)*, vol. 15, no. 5, pp. 1192 – 201, 1998/05/.

[5] Berson, D. M., Dunn, F. A., and Takao, M., "Phototransduction by Retinal Ganglion Cells That Set the Circadian Clock," *Science*, vol. 295, no. 5557, pp. 1070–1073, 2002.

[6] Brainard, G. C., Hanifin, J. P., Greeson, J. M., Byrne, B., Glickman, G., Gerner, E., and Rollag, M. D., "Action Spectrum for Melatonin Regulation in Humans: Evidence for a Novel Circadian Photoreceptor," *J. Neurosci.*, vol. 21, no. 16, pp. 6405–6412, 2001.

[7] Brennan, K. F., *The physics of semiconductors : with applications to optoelectronic devices*. Cambridge ; New York: Cambridge University Press, 1999.

[8] Brunner, D., Angerer, H., Bustarret, E., Freudenberg, F., Hopler, R., Dimitrov, R., Ambacher, O., and Stutzmann, M., "Optical constants of epitaxial algan films and their temperature dependence," *J. Appl. Phys. (USA)*, vol. 82, no. 10, pp. 5090 – 6, 1997/11/15.

[9] Cajochen, C., Zeitzer, J. M., Czeisler, C. A., and Dijk, D.-J., "Dose-response relationship for light intensity and ocular and electroencephalographic correlates of human alertness," *Behavioural Brain Research*, vol. 115, no. 1, pp. 75–83, 2000.

[10] Campbell, S. A., *The science and engineering of microelectronic fabrication*. New York: Oxford University Press, 1996.

[11] Chichibu, S., Azuhata, T., Sota, T., and Nakamura, S., "Excitonic emissions from hexagonal gan epitaxial layers," *Journal of Applied Physics*, vol. 79, no. 5, pp. 2784–2786, 1996.

[12] Chynoweth, A., Logan, R. A., and Feldmann, W. L., "Excess tunnel current in silicon esaki junctions," *Physical Review*, vol. 121, no. 3, pp. 684–&, 1961. 1440C Times Cited:199 Cited References Count:23.

[13] Czeisler, C. A., Duffy, J. F., Shanahan, T. L., Brown, E. N., Mitchell, J. F., Rimmer, D. W., Ronda, J. M., Silva, E. J., Allan, J. S., Emens, J. S., Dijk, D.-J., and Kronauer, R. E., "Stability, Precision, and Near-24-Hour Period of the Human Circadian Pacemaker," *Science*, vol. 284, no. 5423, pp. 2177–2181, 1999.

[14] Dashiell, M. W., Troeger, R. T., Rommel, S. L., Adam, T. N., Berger, P. R., Guedj, C., Kolodzey, J., and Seabaugh, A. C., "Current-voltage characteristics of high current density silicon esaki diodes grown by molecular beam epitaxy and the influence of thermal annealing," *Ieee Transactions on Electron Devices*, vol. 47, no. 9, pp. 1707–1714, 2000. 345KL Times Cited:18 Cited References Count:28.

[15] Diagne, M., He, Y., Zhou, H., Makarona, E., Nurmikko, A. V., Han, J., Waldrip, K. E., Figiel, J. J., Takeuchi, T., and Krames, M., "Vertical cavity violet light emitting diode incorporating an aluminum gallium nitride distributed bragg mirror and a tunnel junction," *Applied Physics Letters*, vol. 79, no. 22, pp. 3720–3722, 2001. 493CL Times Cited:24 Cited References Count:13.

[16] Dijk, D.-J. and Cajochen, C., "Melatonin and the circadian regulation of sleep initiation, consolidation, structure, and the sleep eeg," *J. Biol. Rhythms (USA)*, vol. 12, no. 6, pp. 627 – 35, 1997/12/.

[17] Duschl, R., Schmidt, O. G., Reitemann, G., Kasper, E., and Eberl, K., "High room temperature peak-to-valley current ratio in si based esaki diodes," *Electronics Letters*, vol. 35, no. 13, pp. 1111–1112, 1999. 218JR Times Cited:18 Cited References Count:6.

[18] Ferguson, I., US Patent 6366018.

[19] Ferguson, I., US patent 6404125.

[20] Freedman, M. S., Lucas, R. J., Soni, B., von Schantz, M., Muñoz, M., David-Gray, Z., and Foster, R., "Regulation of Mammalian Circadian Behavior by Non-rod, Non-cone, Ocular Photoreceptors," *Science*, vol. 284, no. 5413, pp. 502–504, 1999.

[21] Gil, B., *Group III nitride semiconductor compounds : physics and applications.* Series on semiconductor science and technology ; 6, Oxford, New York: Clarendon Press; Oxford University Press, 1998.

[22] Gong, Y., Gu, Y., Kuskovsky, I., Neumark, G., Li, J., Lin, J., Jiang, H., and Ferguson, J., "Non-equilibrium acceptor concentration in gan:mg grown by metalorganic chemical vapor deposition," *GaN and Related Alloys - 2003 Symposium (Mater. Res. Soc. Symposium Proceedings Vol.798)*, pp. 491 – 6, 2004//.

[23] Götz, W., Johnson, N. M., and Bour, D. P., "Deep level defects in mg-doped, p-type gan grown by metalorganic chemical vapor deposition," *Applied Physics Letters*, vol. 68, no. 24, pp. 3470–3472, 1996.

[24] Guo, X. and Schubert, E. F., "Current crowding in gan/ingan light emitting diodes on insulating substrates," *Journal of Applied Physics*, vol. 90, no. 8, pp. 4191–4195, 2001.

[25] Jeon, S. R., Song, Y. H., Jang, H. J., Yang, G. M., Hwang, S. W., and Son, S. J., "Lateral current spreading in gan-based light-emitting diodes utilizing tunnel contact junctions," *Applied Physics Letters*, vol. 78, no. 21, pp. 3265–3267, 2001.

[26] Jeon, S.-R., Oh, C. S., Yang, J.-W., Yang, G. M., and Yoo, B.-S., "Gan tunnel junction as a current aperture in a blue surface-emitting light-emitting diode," *Applied Physics Letters*, vol. 80, no. 11, p. 1933, 2002.

[27] Kane, E. O., "Theory of tunneling," *Journal of Applied Physics*, vol. 32, no. 1, p. 83, 1961.

[28] Kauser, M. Z., Osinsky, A., Dabiran, A. M., and Chow, P. P., "Enhanced vertical transport in p-type algan/gan superlattices," *Applied Physics Letters*, vol. 85, no. 22, p. 5275, 2004.

[29] Kendall, M. and Sholand, M., "Energy savings potential of solid state lighting in general lighting applications," 2001. Energy, U.S. Department of.

[30] Kumakura, K., Makimoto, T., and Kobayashi, N., "Efficient hole generation above 10¡sup¿19¡/sup¿ cm¡sup¿-3¡/sup¿ in mg-doped in gan/gan superlattices at room temperature," *Japanese Journal of Applied Physics, Part 2: Letters*, vol. 39, no. 3 A-B, pp. 195–196, 2000. 00275185647 Compilation and indexing terms, Copyright 2005 Elsevier Engineering Information, Inc. 0021-4922 Indium gallium nitride Acceptor Gallium nitride.

[31] Kumar Wickramasinghe, H., "Scanning probe microscopy: current status and future trends," *J. Vac. Sci. Technol. A, Vac. Surf. Films (USA)*, vol. 8, no. 1, pp. 363 – 8, 1990/01/.

[32] Kurata, K., Ono, Y., Ito, K., Mori, M., and Sano, H., "An experimental study on improvement of performance for hemispherically shaped high-power ireds with ga¡sub¿1-x¡/sub¿al¡sub¿x¡/sub¿as grown junctions," *IEEE Trans. Electron Devices (USA)*, vol. ED-28, no. 4, pp. 374 – 9, 1981/04/.

[33] Langer, R., Barski, A., Simon, J., Pelekanos, N., Konovalov, O., Andre, R., and Dang, L. S., "High-reflectivity gan/gaaln bragg mirrors at blue/green wavelengths grown by molecular beam epitaxy," *Appl. Phys. Lett. (USA)*, vol. 74, no. 24, pp. 3610 – 12, 1999/06/14.

[34] Laws, G., Larkins, E., Harrison, I., Molloy, C., and Somerford, D., "Improved refractive index formulas for the $al_xga_{1-x}n$ and $in_yga_{1-y}n$ alloys," *J. Appl. Phys. (USA)*, vol. 89, no. 2, pp. 1108 – 15, 2001/01/15.

[35] Lee, C. M., Chuo, C. C., Chen, I. L., Chang, J. C., and Chyi, J. I., "High-brightness inverted ingan-gan multiple-quantum-well light-emitting diodes without a transparent conductive layer," *Ieee Electron Device Letters*, vol. 24, no. 3, pp. 156–158, 2003.

[36] Lee, R. T. and Stringfellow, G. B., "Pyrolysis of 1,1 dimethylhydrazine for omvpe growth," *Journal of Electronic Materials*, vol. 28, no. 8, p. 963, 1999.

[37] Leung, M., Djurisic, A., and Li, E., "Refractive index of ingan/gan quantum well," *J. Appl. Phys. (USA)*, vol. 84, no. 11, pp. 6312 – 17, 1998/12/01.

[38] Lewy, A., Wehr, T., Goodwin, F., Newsome, D., and Markey, S., "Light suppresses melatonin secretion in humans," *Science*, vol. 210, no. 4475, pp. 1267–1269, 1980.

[39] Lin, Y.-J., "Activation mechanism of annealed mg-doped gan in air," *Applied Physics Letters*, vol. 84, no. 15, pp. 2760–2762, 2004.

[40] Liu, C. H., Su, Y. K., Wu, L. W., Chang, S. J., and Chuang, R. W., "Tunnelling efficiency of n(+)-ingan/gan short period superlattice tunnelling contact layer for nitride-based light emitting diodes," *Semiconductor Science And Technology*, vol. 18, no. 6, pp. 545–548, 2003.

[41] Logan, R. A. and Chynoweth, A. G., "Effect of degenerate semiconductor band structure on current-voltage characteristics of silicon tunnel diodes," *Physical Review*, vol. 131, no. 1, pp. 89–&, 1963. 1498C Times Cited:39 Cited References Count:12.

[42] Meyerhofer, D., Brown, G. A., and Sommers, H. S., "Degenerate germanium .1. tunnel, excess, and thermal current in tunnel diodes," *Physical Review*, vol. 1, no. 4, pp. 1329–&, 1962. 1471C Times Cited:56 Cited References Count:49.

[43] Miyoshi, S., Onabe, K., Ohkouchi, N., Yaguchi, H., Ito, R., Fukatsu, S., and Shiraki, Y., "Movpe growth of cubic gan on gaas using dimethylhydrazine," *Journal of Crystal Growth*, vol. 124, no. 1-4, p. 439, 1992.

[44] Nakada, N., Nakaji, M., Ishikawa, H., Egawa, T., Umeno, M., and Jimbo, T., "Improved characteristics of ingan multiple-quantum-well light-emitting diode by gan/algan distributed bragg reflector grown on sapphire," *Appl. Phys. Lett. (USA)*, vol. 76, no. 14, pp. 1804 – 6, 2000/04/03.

[45] Nakamura, S., "The roles of structural imperfections in ingan-based blue light-emitting diodes and laser diodes," *Science*, vol. 281, no. 5379, pp. 956–961, 1998.

[46] Nakamura, S., Mukai, T., Senoh, M., and Iwasa, N., "Thermal annealing effects on p-type mg-doped gan films," *Jpn. J. Appl. Phys. 2, Lett. (Japan)*, vol. 31, no. 2B, pp. 139 – 42, 1992/02/15.

[47] Ng, H., Moustakas, T., and Chu, S., "High reflectivity and broad bandwidth aln/gan distributed bragg reflectors grown by molecular-beam epitaxy," *Appl. Phys. Lett. (USA)*, vol. 76, no. 20, pp. 2818 – 20, 2000/05/15.

[48] Nicol, D. B. and Ferguson, I. T., "Development of a circadian light source," *Proceedings of the SPIE - The International Society for Optical Engineering*, vol. 4776, p. 255, 2002. Copyright 2003, IEE 7680685 0277-786X circadian light source solid state lighting controllability lighting environment multiple LEDs emission wavelengths illumination source spectral power distribution psychological aspects color variation biological changes color temperature spectral difference broadband source light therapy polychromatic Planckian Locus CIE diagram 460 nm.

[49] O'Donnell, K. P., Martin, R. W., and Middleton, P. G., "Origin of luminescence from ingan diodes," *Physical Review Letters*, vol. 82, no. 1, pp. 237–240, 1999.

[50] Ohring, M., *The materials science of thin films : deposition and structure*. San Diego, CA: Academic Press, 2nd ed., 2002.

[51] Ozden, I., Makarona, E., Nurmikko, A. V., Takeuchi, T., and Krames, M., "A dual-wavelength indium gallium nitride quantum well light emitting diode," *Applied Physics Letters*, vol. 79, no. 16, p. 2532, 2001.

[52] Park, E.-H., Joong-Seo-Park, and Yoo, T.-K., "As-grown p-type gan growth by dimethylhydrazine nitrogen precursor," *Journal of Crystal Growth*, vol. 272, no. 1-4, pp. 426 – 31, 2004/12/10.

[53] Peng, T. and Piprek, J., "Refractive index of algainn alloys," *Electron. Lett. (UK)*, vol. 32, no. 24, pp. 2285 – 6, 1996/11/21.

[54] Piprek, J. and of Photo-optical Instrumentation Engineers., S., *Semiconductor optoelectronic devices for lightwave communication : 8-10 September 2003, Orlando, Florida, USA*. Bellingham, Wash.: SPIE, 2003.

[55] Rea, M. S. and Bullough, J. D., "Application efficacy," *Journal of the Illuminating Engineering Society*, vol. 30, no. 2, pp. 73 – 95, 2001.

[56] Rommel, S. L., Dillon, T. E., Dashiell, M. W., Feng, H., Kolodzey, J., Berger, P. R., Thompson, P. E., Hobart, K. D., Lake, R., Seabaugh, A. C., Klimeck, G., and Blanks, D. K., "Room temperature operation of epitaxially grown si/si0.5ge0.5/si resonant interband tunneling diodes," *Applied Physics Letters*, vol. 73, no. 15, pp. 2191–2193, 1998. 128UX Times Cited:42 Cited References Count:20.

[57] Royo, P., Stanley, R., and Ilegems, A., "Analytical calculation of the extraction efficiency of microcavity light-emitting diodes for display and fiber coupling applications," *IEEE J. Sel. Top. Quantum Electron. (USA)*, vol. 8, no. 2, pp. 207 – 18, 2002/03.

[58] Sheu, J. K., Chi, G. C., and Jou, M. J., "Low-operation voltage of ingan/gan light-emitting diodes by using a mg-doped al¡sub¿0.15¡/sub¿ga¡sub¿0.85¡/sub¿n/gan superlattice," *Electron Device Letters, IEEE*, vol. 22, no. 4, p. 160, 2001. 0741-3106.

[59] Someya, T. and Arakawa, Y., "Highly reflective gan/$al_{0.34}ga_{0.66}$n quarter-wave reflectors grown by metal organic chemical vapor deposition," *Appl. Phys. Lett. (USA)*, vol. 73, no. 25, pp. 3653 – 5, 1998/12/21.

[60] Stringfellow, G. B., *Organometallic vapor-phase epitaxy : theory and practice*. San Diego: Academic Press, 2nd ed., 1999.

[61] Sugawara, M., "Model for lasing oscillation due to bi-excitons and localized bi-excitons in wide-gap semiconductor quantum wells," *Japanese Journal of Applied Physics, Part 1 (Regular Papers & Short Notes)*, vol. 35, no. 1A, p. 124, 1996.

[62] Takeuchi, T., Hasnain, G., Corzine, S., Hueschen, M., Schneider, R. P., J., Kocot, C., Blomqvist, M., Ying-Lan, C., Lefforge, D., Krames, M. R., Cook, L. W., and Stockman, S. A., "Gan-based light emitting diodes with tunnel junctions," *Japanese Journal of Applied Physics, Part 2 (Letters)*, vol. 40, no. 8B, p. 861, 2001. Copyright 2001, IEE 7044097 0021-4922 GaN-based light emitting diodes tunnel junctions hole injection GaN:Si InGaN:Mg GaN-InGaN quantum well heterostructure forward voltage voltage drop reverse-biased tunnel junction light output semi-transparent electrode highly resistive p-AlGaN cladding layer 15 nm 30 nm 4.1 V 3.5 V GaN:Si-InGaN:Mg.

[63] Takeuchi, T., Sota, S., Katsuragawa, M., Komori, M., Takeuchi, H., Amano, H., and Akasaki, I., "Quantum-confined stark effect due to piezoelectric fields in gainn strained quantum wells," *Japanese Journal of Applied Physics Part 2-Letters*, vol. 36, no. 4A, pp. L382–L385, 1997.

[64] Windisch, R., Dutta, B., Kuijk, M., Knobloch, A., Meinlschmidt, S., Schoberth, S., Kiesel, P., Borghs, G., Dohler, G., and Heremans, P., "40% efficient thin-film surface-textured light-emitting diodes by optimization of natural lithography," *IEEE Trans. Electron Devices (USA)*, vol. 47, no. 7, pp. 1492 – 8, 2000/07/.

[65] Yeh, P., *Optical waves in layered media*. New York: Wiley, 1988.

[66] Zukauskas, A., Shur, M., and Gaska, R., *Introduction to solid-state lighting*. New York: J. Wiley, 2002.

INDEX

VITA

David Brackin Nicol was born on March 3, 1979 in Tallahassee, Florida. He moved with his family to Auburn, Alabama in 1984 where he lived through senior year of High School. In 1997, he began his freshman year at Georgia Institute of Technology. David graduated with High Honors in Electrical Engineering during the May 2002. Also during the spring of 2002 he began undergraduate research with Dr. Ian Ferguson on solid state lighting and circadian rhythms. This partnership was a good match and led to graduate studies under Dr. Ferguson in solid state lighting.